Search for Anomalous Couplings in the Decay of Polarized Z Bosons to Tau Lepton Pairs*

Eric C. Torrence

Stanford Linear Accelerator Center
Stanford University
Stanford, CA 94309

---

*Ph.D. thesis, Massachusetts Institute of Technology, Cambridge, MA 02139.

Search for Anomalous Couplings in the Decay of Polarized Z Bosons to Tau Lepton Pairs

by

Eric C. Torrence

B.S., Physics
University of Washington, 1990

Submitted to the Department of Physics
in partial fulfillment of the requirements for the Degree of

DOCTOR OF PHILOSOPHY

at the

MASSACHUSETTS INSTITUTE OF TECHNOLOGY

June 1997

Author . . . .
Department of Physics
May 22, 1997

Certified by . . . .
Richard K. Yamamoto
Professor of Physics
Thesis Supervisor

Accepted by . . . .
George F. Koster
Chairman, Graduate Committee
Department of Physics

Search for Anomalous Couplings in the Decay of Polarized Z Bosons to Tau Lepton Pairs

by

Eric C. Torrence

Submitted to the Department of Physics
on May 22, 1997 in partial fulfillment of the
requirements for the Degree of
DOCTOR OF PHILOSOPHY

Abstract

Using a sample of 4,500 polarized Z decays to τ lepton pairs accumulated with the SLD detector at the SLAC Linear Collider (SLC) in 1993-95, a search has been made for anomalous couplings in the neutral current reaction $e^+e^- \to \tau^+\tau^-$. A measurement of the CP violating Weak Electric Dipole Moment (WEDM) and the CP conserving Weak Magnetic Dipole Moment (WMDM) of the τ lepton has been performed by considering the transverse spin polarization of τ leptons produced at the Z pole. Using a maximum likelihood technique, the observed τ decay spectra in the e, μ, π, and ρ decay channels are used to infer the net transverse polarization of the underlying tau leptons, and a fit for the anomalous dipole moments is performed. No evidence for these dipole moments is observed, and limits are placed on both the real and imaginary parts of the WEDM and WMDM.

Thesis Supervisor: Richard K. Yamamoto
Title: Professor of Physics

Acknowledgments

First and foremost, I would like to thank my wife Tamara. Without her constant patience and support, I am quite certain that this thesis would have never been completed. I love you.

I owe a tremendous debt to the friends I have made working on the Compton polarimeter. Bruce Schumm and Mike Fero showed me the ropes very early on, and they had me working within hours of arriving at SLAC. Morris Swartz has always been a most pleasant source of animated conversation, while Mike Woods always had yet another annoying task to bring to my attention. Working with these four gentlemen has been the most challenging and rewarding experience of my albeit brief career. I am sure I will be telling stories about them for many years to come. Stories will also be told about Peter Rowson and Ray Frey, who like to think of themselves as being above this whole polarimeter business, but are really cut from the same cloth.

The SLD collaboration may be unique in modern particle physics in that so much has been done by so few with so little. I would particularly like to thank the graduate students before me, who inevitably bore the brunt of this axiom, and managed to bring the machine out of the dark ages and into the veritable renaissance which I enjoyed during my stay. Special thanks are extended to Amit Lath for being such a good office mate, Tom Junk for his endless patience and support, Mike Hildreth for

his continuing help and guidance, Homer Neal for his constant efforts on everyone's behalf, and Dave Williams for just being Dave.

In the now dwindling tau group I must thank Jim Quigley and Nik Allen for allowing me to swipe huge chunks of their thesis without even a mild protest, Mourad Daoudi for his persistent leadership, and Erez Etzion for his outlook on life.

Jim deserves special mention for being such a pleasant companion during these seven arduous years of graduate schooling, while Oliver Bardon gets special credit for showing both of us how to stay sane while navigating the MIT maze. I would also like to thank Phil Burrows for the many donuts, the few pleasant hikes, and his friendship, while Ramon Berger will always have a special place in my heart for his carpooling wit and unique perspective. Ray Cowan also deserves a kind nod for the many useful discussions about rocks over the years.

It goes without saying, although I will say it anyway, that I am indebted to all of the SLD collaborators past and present who have toiled and struggled so that real physics could actually be produced. I am particularly grateful to Marty Breidenbach, Charlie Prescott, and Charles Baltay for their efforts on behalf of the collaboration, as well as the tremendous support which they have extended to me personally.

I would like to thank Eddie Farhi and Paul Joss, my intrepid readers, for both allowing me to graduate and for being so understanding of my particular geographic difficulties. I would also like to thank my advisor, Richard Yamamoto, for allowing me to make my own mistakes and for providing unwavering support every step of the way. I appreciate everything that you have done for me.

Finally, my parents deserve special thanks for not just the obvious biological reasons, but for fostering an environment of love and rational thought which inspired me to start questioning the world around me at a very early age.

Contents

List of Figures

List of Tables

Chapter 1

Introduction

The modern theory of Electroweak interactions was first proposed by Glashow, Weinberg, and Salaam in the 1960s[1] and in recent years has been verified with ever increasing accuracy by the large data samples currently being collected at the high energy e^+e^- accelerators running at CERN and SLAC. While this may be a theoretical triumph for the GWS theory, theorists of today adamantly believe that there must be something beyond this so called Standard Model (SM) which is more comprehensive and complete. A number of models have been proposed in recent years under the general rubric of Supersymmetry which reproduce the basic attributes of the GWS theory from a more fundamental starting point. Since the current body of experimental data agrees quite well with the Standard Model, however, there is no experimental guidance available to distinguish which, if any of the various flavors of Supersymmetry is correct. This has left the particle physics community quite interested in finding any sort of experimental signature of something new that the Standard Model cannot accommodate.

In the spirit of leaving no stone unturned, this thesis describes a measurement of the anomalous, non-SM, tensor couplings in the decay of Z bosons to tau leptons. This analysis was performed on a sample of Z boson events produced by polarized

e^+e^- collisions at the SLAC Linear Collider (SLC) and observed by the SLAC Large Detector (SLD) during the 1993 and 1994-95 running periods. This analysis is somewhat complementary to similar measurements which have been performed by the LEP collaborations at CERN, and in the absence of any signal for these anomalous couplings, upper limits have been placed on their relative strengths.

1.1   Background

Long before the GWS theory was proposed, and even before the formulation of relativistic quantum field theory, physicists were measuring the electric and magnetic dipole moments of the electron and muon.[2] Originally a macroscopic concept describing a spatial distribution of electric charge or current, in the context of relativistic field theory the dipole moment of a point-like lepton represents a measurement of higher order quantum corrections to the point-like first order Born interactions.

Experiments measuring the electric dipole moment of the electron and muon have been underway for many decades, and the current world average values of

$$\tilde{d}_e^\gamma = (-0.3 \pm 0.8) \times 10^{-26} \ e \ \text{cm}$$
$$\tilde{d}_\mu^\gamma = (3.7 \pm 3.4) \times 10^{-19} \ e \ \text{cm}$$

are consistent with zero to astonishing precision.[3] Under the operation of time reversal (T), an electric dipole moment will change sign, violating the principle of T invariance. As all interactions are postulated to be invariant under the combined reversal of charge, parity, and time (CPT) by quantum field theory, the presence of an electric dipole moment must also be accompanied by a violation of CP invariance. The true nature of CP violation in nature is currently not well understood, and although the Standard Model can phenomenologically account for the CP violation experimentally observed in the quark sector, it does not provide any fundamental
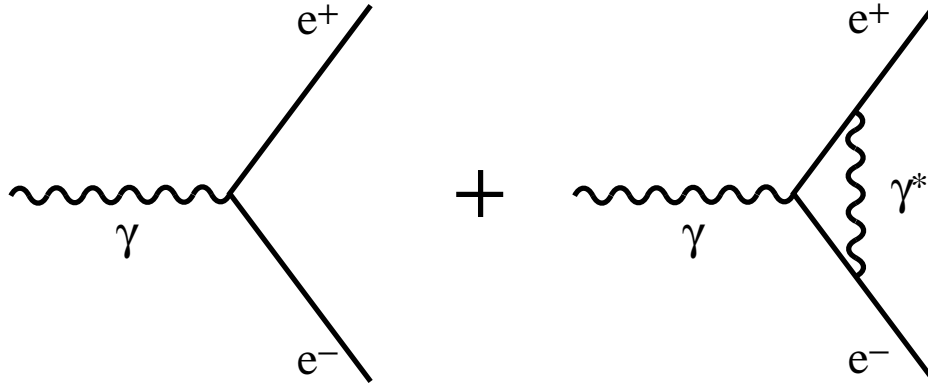
Figure 1-1: Higher order Feynman diagrams contributing to the anomalous magnetic moment of the electron are shown.

guidance to explain why it has not been observed elsewhere. As such, measurements limiting the electric dipole moments in the leptonic sector provide a useful constraint when attempting to construct theories beyond the Standard Model.

In contrast to the electric dipole moment, the CP conserving magnetic dipole moment is known to pick up corrections from higher order electroweak processes. The leading terms contributing to the anomalous magnetic moment of the electron are shown in Figure 1-1. Precision measurements of this anomalous part of the magnetic dipole moment have long been used as a test of theoretical models, and their accurate prediction was one of the great triumphs of Quantum Electrodynamics (QED) in the 1960s. The current world average values of

$$\mu_e = (1.001\ 159\ 652\ 193 \pm 0.000\ 000\ 000\ 010)\ \frac{e\hbar}{2m_e}$$

$$\mu_\mu = (1.001\ 165\ 923 \pm 0.000\ 000\ 008)\ \frac{e\hbar}{2m_\mu}$$

agree well with the predictions of the Standard Model, and a program is currently

underway at Brookhaven to reduce the error on the magnetic moment of the muon by another factor of 20.[4] At this precision, purely weak corrections will become important, and this measurement will provide a nice low energy test of the Standard Model.

Given that the electric and magnetic dipole moments of the electron and muon have already been measured to high precision, what is the motivation behind measuring these quantities for the tau lepton? First, the dipole moments involved in the process $Z \rightarrow \tau^+\tau^-$ are *weak* dipole moments rather than the *electromagnetic* dipole moments involved at the $\gamma \rightarrow \tau^+\tau^-$ vertex. Considerations of gauge invariance require that these couplings are related, but in principle they are not the same thing. Second, because all of the elements involved in the $Z \rightarrow \tau^+\tau^-$ vertex are heavy, any new physics which couples to the mass of a particle would be enhanced at this vertex compared to any of the lighter leptons coupling to a photon. While the details of this argument depend on the specifics of the new physics involved, almost any plausible new physics which comes from a higher mass scale is not excluded at the current limits on the weak tau dipole moments by the more precise electron or muon data. Third, although the Standard Model couplings are universal among the three lepton families, there is no compelling fundamental reason why this must be so, and individual measurements of each family are clearly desired. Finally, in contrast to the anomalous magnetic moment of the lighter leptons, the Standard Model contribution to the anomalous magnetic moment of the tau lepton has been calculated to be[5]

$$d_\tau^Z = -(1.2 + 0.3i) \times 10^{-20} \ e \ \mathrm{cm}, \tag{1.1}$$

which is many orders of magnitude below the experimental sensitivity of this analysis. One of the leading diagrams contributing to this WMDM is shown in Figure 1-2. A Standard Model contribution to the CP violating WEDM would require a two
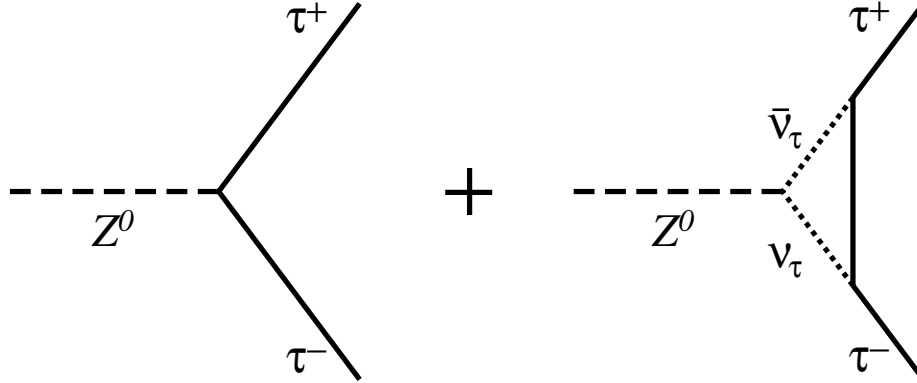
Figure 1-2: The largest Standard Model contribution to the CP conserving WMDM is shown. The effect of this term is many orders of magnitude below the experimental sensitivity of this analysis. The leading SM contribution to the CP violating WEDM is estimated to be considerably smaller.

loop diagram at the decay vertex, and the magnitude of this CP violating amplitude has been estimated to be at least seven orders of magnitude below the tree level process.[6] As the Standard Model prediction for these anomalous couplings is vanishingly small, any measured non-zero value is a direct sign of new physics.

Aside from the increased sensitivity to new physics, there are other benefits to performing this measurement at the Z pole with tau lepton pairs. Tau leptons are readily identified with high efficiency and low background at the Z pole by the highly collimated and low multiplicity nature of their observable decay products. As will be shown in Section 1.2, the dipole couplings of any lepton involve tensor operators producing spin dependent observables. Since the tau lepton decays shortly after it is produced, the spin of the original tau can be measured, at least in a statistical sense, by the momentum spectra of the observed tau decay products. This technique will be used in this analysis to measure the transverse polarization of the produced tau leptons which is directly related to the anomalous weak dipole moments of interest.

1.2   Dipole Moment Formalism

In the process

$$e^+e^- \to V \to \tau^+\tau^- \tag{1.2}$$

the most general Lorentz structure for the coupling of the tau leptons to the neutral vector field V_μ is described using operators up to dimension six by the Lagrangian

$$\mathcal{L} = -g\,\bar{\tau}\left[\gamma^\mu(F_1^L P_- + F_1^R P_+) - \frac{i\sigma^{\mu\nu}q_\nu}{m_\tau}(F_2^L P_- + F_2^R P_+) \right.$$
$$\left. + q^\mu(F_3^L P_- + F_3^R P_+)\right]\tau\,V_\mu, \quad (1.3)$$

where q^μ is the momentum of the gauge boson V.[7] The couplings are explicitly written in terms of left and right handed form factors $F^{L/R}$ by use of the projection operator $P_\mp = \frac{1}{2}(1 \mp \gamma^5)$ which selects only the left or right handed tau lepton. In general these couplings can be complex, energy dependent, and will have different strengths depending upon which vector boson V is being considered.

The F_3 form factor represents a contact term which will vanish for the photon due to considerations of gauge invariance, and will also vanish for a Z boson which is on shell or coupled to massless fermions. For scattering at the Z pole, these F_3 terms can be safely ignored, and explicitly substituting for the projection operators $P_\pm$, Equation 1.3 can be re-written as

$$\mathcal{L} = -\frac{g}{2}\bar{\tau}\left[\gamma^\mu(A - B\gamma^5) - \frac{i\sigma^{\mu\nu}q_\nu}{m_\tau}(C - D\gamma^5)\right]\tau V_\mu \tag{1.4}$$

where

$$A = (F_1^L + F_1^R) \qquad B = (F_1^L - F_1^R)$$
$$C = (F_2^L + F_2^R) \qquad D = (F_2^L - F_2^R). \tag{1.5}$$

At tree level in the Standard Model, these couplings are predicted to be

$$F_1^L(Z) = (c_v + c_a)/2 = -\frac{1}{2} + \sin^2\theta_w$$
$$F_1^R(Z) = (c_v - c_a)/2 = \sin^2\theta_w \tag{1.6}$$
$$F_2^L(Z) = F_2^R(Z) = 0$$

$$F_1^L(\gamma) = F_1^R(\gamma) = -g_e/g_z \tag{1.7}$$
$$F_2^L(\gamma) = F_2^R(\gamma) = 0$$

where $\sin^2\theta_w$ is the weak mixing angle, and g from Equation 1.3 has been set to the neutral weak coupling parameter g_z. Substituting in these values, the Standard Model Lagrangian can then be written as

$$\mathcal{L}_{SM} = -\frac{g_z}{2}\bar{\tau}\left[\gamma^\mu(c_v - c_a\gamma^5)\right]\tau\ Z_\mu + g_e\bar{\tau}\gamma^\mu\tau\ A_\mu. \tag{1.8}$$

For scattering at the Z pole, the terms involving the photon propagator are highly suppressed with respect to the Z propagator by a factor of $\mathcal{O}(\Gamma_Z/m_Z)$ in the relative amplitudes, such that the cross section from Z boson production is ~ 800 times the cross section from pure γ exchange. The cross section from the γ-Z interference term strictly vanishes at the Z pole, although initial state radiation smears the collision energy enough to produce a $\sim 2\%$ contribution to the total rate. This small photon amplitude and other higher order SM corrections to the tree level calculation can be accommodated with the improved Born approximation where the coupling parameters c_v and c_a are defined to be collision-energy dependent *effective* couplings defined in terms of the *effective* weak mixing angle $\sin^2\theta_w^{eff}$, which incorporates all higher order terms which do not modify the basic $V - A$ Lorentz structure.[1] Those

---

[1] The exact details of which higher order terms are included into the effective couplings can vary between different theoretical schemes. Usually, the photon amplitudes are *not* included. A

Standard Model corrections which do modify the $V - A$ Lorentz structure contribute directly to the weak dipole moments of interest, although these terms have already been shown to be extremely small.

In this analysis, the possibility of new vector bosons beyond the Standard Model directly producing tau pairs through the process

$$e^+ e^- \rightarrow V_{new} \rightarrow \tau^+ \tau^- \tag{1.9}$$

will not be explicitly considered. New physics of this type would not modify the underlying Lorentz structure of the vertex, but rather would appear as a modification to the Standard Model c_v and c_a couplings in a similar fashion as the presence of the photon propagator. Evidence for this sort of new physics would be seen in the precision electroweak measurements of the Z partial width to tau leptons $\Gamma_Z(\tau)$ or the electroweak asymmetry parameter A_τ. Rather, this analysis is sensitive to any new physics which enters as a higher order correction to the $Z \rightarrow \tau^+ \tau^-$ vertex leading to non-zero F_2 couplings. The Lagrangian responsible for these anomalous couplings can be written as

$$\mathcal{L}_{anom} = \frac{i}{2} \bar{\tau} \left[\sigma^{\mu\nu} q_\nu (d_\tau - i \tilde{d}_\tau \gamma^5) \right] \tau \; Z_\mu, \tag{1.10}$$

where the parameters

$$d_\tau \equiv \frac{g_z}{m_\tau} (F_2^L + F_2^R) \tag{1.11}$$

$$\tilde{d}_\tau \equiv -i \frac{g_z}{m_\tau} (F_2^L - F_2^R) \tag{1.12}$$

are identified as the Weak Magnetic Dipole Moment (WMDM) and Weak Electric Dipole Moment (WEDM) in analogy with the equivalent parameters defined at the

---

decent review can be found in PDG 96[3].

photon vertex.[2] The definition of the WEDM $\tilde{d}_\tau$ as written in Equation 1.10 is chosen to agree with the convention which is (almost) consistently followed in the experimental literature. There is no consistent definition of the WMDM, and this definition was chosen out of notational simplicity. Some authors choose to write the WMDM in terms of the dimensionless anomalous contribution to the Weak Magnetic Moment a_τ^Z where $d_\tau = (a_\tau^Z e)/(2m_\tau)$. Unfortunately, things are even less standardized in the theoretical literature, and when comparisons are made between the work of different authors, or even between different papers from the same author, one must refer to the equivalent of Equation 1.10 to understand just which scale factors and sign conventions are being employed to define the anomalous coupling parameters.

Despite the notational difficultly, the anomalous dipole couplings defined in Equation 1.10 are model-independent phenomenological form factors which describe the most general next-highest order coupling at the $Z \to \tau^+ \tau^-$ vertex, which is predicted to be effectively zero by the Standard Model. As written, the dipole moments $d_\tau, \tilde{d}_\tau$ are dimensional quantities with units of $e \cdot \mathrm{cm}$. The effect of turning on these anomalous couplings through some new physical process beyond the Standard Model will be covered in Section 1.3 and Appendix A. In Section 1.4 it will be shown that a non-zero WEDM ($\tilde{d}_\tau$) will produce a CP violating interaction, while the WMDM (d_τ) is an intrinsically CP conserving parameter.

---

[2] Strictly, these should be written as d_τ^Z and $\tilde{d}_\tau^Z$, although the weak (Z) dipole moments are always implied when not explicitly specified.

1.3 Cross Sections

The differential cross section for the production and subsequent decay of tau leptons at the Z pole can be conveniently be written as

$$\frac{d\sigma_{L/R}}{d\Omega \, d\mathbf{q}_a^+ d\mathbf{q}_b^-} \propto \chi_{L/R}^{\alpha'\alpha\beta'\beta}(\Omega) \, \mathcal{D}^{\alpha'\alpha}(\mathbf{q}_a^+) \, \mathcal{D}^{\beta'\beta}(\mathbf{q}_b^-) \tag{1.13}$$

where $\chi_{L/R}(\Omega)$ is the production spin density matrix for a left or right handed incident electron, and $\mathcal{D}(\mathbf{q}_a^+)$ is the tau decay spin density matrix to a particular final state a with momentum $\mathbf{q}_a^+$. The production spin density matrix is simply a compact notation for the squared production amplitudes given by

$$\chi_{L/R}^{\alpha'\alpha\beta'\beta} = \mathcal{M}^\star(e^+ e_{L/R}^- \to \tau_{\alpha'}^+ \tau_{\beta'}^-) \, \mathcal{M}(e^+ e_{L/R}^- \to \tau_\alpha^+ \tau_\beta^-), \tag{1.14}$$

while the elements of the tau decay matrix are similarly given by

$$\mathcal{D}^{\alpha'\alpha}(\mathbf{q}_a^+) = \mathcal{M}^\star(\tau_{\alpha'}^+ \to a(\mathbf{q}_a^+) + X) \, \mathcal{M}(\tau_\alpha^+ \to a(\mathbf{q}_a^+) + X) \tag{1.15}$$

where the indices $(\alpha', \alpha) / (\beta', \beta)$ represent the explicit spin states of the intermediate τ^+ / τ^- amplitudes.

The calculation of this differential cross section for both the Standard Model and the anomalous couplings defined in Equation 1.8 and Equation 1.10 is described fully in Appendix A. The coordinate system used to describe the tau spin direction is defined such that the $+\hat{\mathbf{z}}$ axis points in the direction of the produced τ^- lepton, while the $+\hat{\mathbf{x}}$ axis lies in the production plane, pointing in the direction of increasing θ. The τ^+ hemisphere uses the identical coordinate system as the τ^- hemisphere as shown in Figure 1-3, while the spin basis is chosen so that the orthogonal tau spin states are labeled $(+/-)$ depending on whether the longitudinal spin of the tau is aligned or opposed to the $+\hat{\mathbf{z}}$ axis.
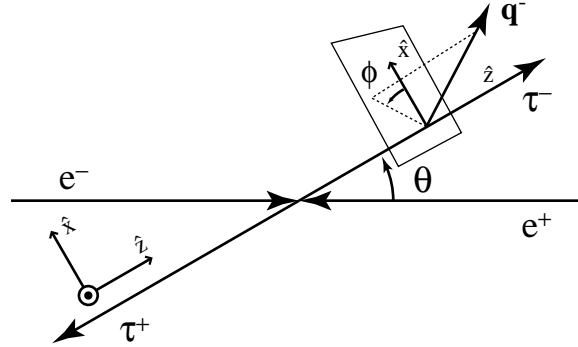
Figure 1-3: The tau decay matrix coordinate system is shown. The same coordinate system is used to describe both tau hemispheres, and the azimuthal decay angle ϕ describes the angle of the tau decay product out of the tau production plane.

Under the relativistic approximation of a massless tau lepton, there are two SM production amplitudes and two anomalous coupling amplitudes as shown in Table 1.1 where the shorthand notation for the production amplitudes

$$\mathcal{A}_{L/R}(\alpha, \beta) = \mathcal{M}(e^+ e^-_{L/R} \to \tau^+_\alpha \tau^-_\beta) \tag{1.16}$$

has been used. For notational clarity, the anomalous couplings have been written in terms of the dimensionless coupling constants $k_v \equiv \frac{\sqrt{s}}{g_z} d_\tau$, $k_a \equiv i\frac{\sqrt{s}}{g_z} \tilde{d}_\tau$, where $\sqrt{s} = m_Z$ is the collision energy.

As shown in Figure 1-4, the two non-zero Standard Model amplitudes $\mathcal{A}(++)$ and $\mathcal{A}(--)$ produce tau pairs with their spins aligned in the same direction, either along or opposed to the τ^- momentum vector. In the relativistic limit, these amplitudes are not modified by the addition of the anomalous coupling terms, but rather the other two amplitudes $\mathcal{A}(+-)$ and $\mathcal{A}(-+)$ are turned on producing tau pairs with their spins anti-aligned, as shown in Figure 1-5. These two anomalous amplitudes are CP conjugates of each other, that is to say that under the CP reversal

Table 1.1: Relativistic Tau Production Amplitudes

	Left Handed $-g_z^2 E^2 (c_v + c_a) \times$	Right Handed $-g_z^2 E^2 (c_v - c_a) \times$
$\mathcal{A}(++)$	$-(c_v - c_a)(1 - \cos\theta)$	$-(c_v - c_a)(1 + \cos\theta)$
$\mathcal{A}(--)$	$-(c_v + c_a)(1 + \cos\theta)$	$-(c_v + c_a)(1 - \cos\theta)$
$\mathcal{A}(+-)$	$+(k_v - k_a)\sin\theta$	$-(k_v - k_a)\sin\theta$
$\mathcal{A}(-+)$	$+(k_v + k_a)\sin\theta$	$-(k_v + k_a)\sin\theta$

The relativistic tau production amplitudes for both Standard Model and anomalous couplings are shown separately for left and right handed incident electrons.

operation, $\mathcal{A}(+-) \underset{CP}{\Longrightarrow} \mathcal{A}(-+)$.[3] From Table 1.1, these two amplitudes will be unequal only if the Weak Electric Dipole Moment (k_a) is non-zero, giving rise to a CP violating interaction. If only the Weak Magnetic Dipole Moment (k_v) is non-zero, the spin structure of the produced tau leptons will be modified, but the additional amplitudes will preserve CP invariance. The two Standard Model amplitudes are both CP conjugates of themselves, and hence there is no possibility of generating a CP violating amplitude using only these tree level SM couplings.

It will be assumed for the remainder of this analysis that the initial state electron beam is an ensemble of longitudinally polarized particles with no coherent transverse polarization. Under this assumption, the cross section for a given electron beam polarization $\mathcal{P}_e$ can be written in terms of the derived cross sections as

$$d\sigma(\mathcal{P}_e) = \frac{1}{2}(1 - \mathcal{P}_e)d\sigma_L + \frac{1}{2}(1 + \mathcal{P}_e)d\sigma_R \qquad (1.17)$$

where the polarization is defined by $\mathcal{P}_e \equiv (n_R - n_L)/(n_R + n_L)$ such that $\mathcal{P}_e < 0$ denotes a left polarized beam.

---

[3] This relation is only strictly true if the initial state is a CP conjugate of itself. This condition is satisfied with the production of vector bosons in $e^+ e^-$ collisions.
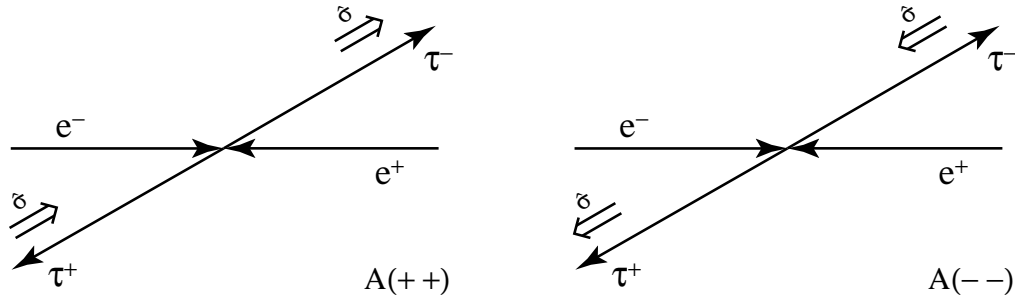
Figure 1-4: The Standard Model production amplitudes create tau pairs with their spins aligned. These two amplitudes can only produce longitudinally polarized taus.

1.4   Transverse Polarization

The production spin density matrix $\chi^{\alpha'\alpha\beta'\beta}$ is the production cross section for a τ^+ lepton into the spin state described by the superscripts (α', α), and a τ^- lepton into the spin state described by the superscripts (β', β). To explore the basic phenomenology of the anomalous dipole moments, it is useful to write this matrix explicitly in the Pauli spin space of the two tau leptons. The spin structure of χ can then be decomposed into the following form

$$\chi = \sigma_0 \left[\mathbf{1} \otimes \mathbf{1}\right] + B_i^+ \left[\hat{\sigma}_i^+ \otimes \mathbf{1}\right] + B_j^- \left[\mathbf{1} \otimes \hat{\sigma}_j^-\right] + C_{ij} \left[\hat{\sigma}_i^+ \otimes \hat{\sigma}_j^-\right], \qquad (1.18)$$

where the 2 by 2 unit matrix is denoted by $\mathbf{1}$, and $\hat{\sigma}_i$ denotes one of the three Pauli spin matrices.[4] The first term gives the total differential cross section for tau production independent of the tau spin orientation. The next two terms each have three components representing the net tau spin polarization of the τ^+ and τ^- respectively, while the final term describes the explicitly spin correlated part of the

---

[4] This notation is more fully developed in [8].
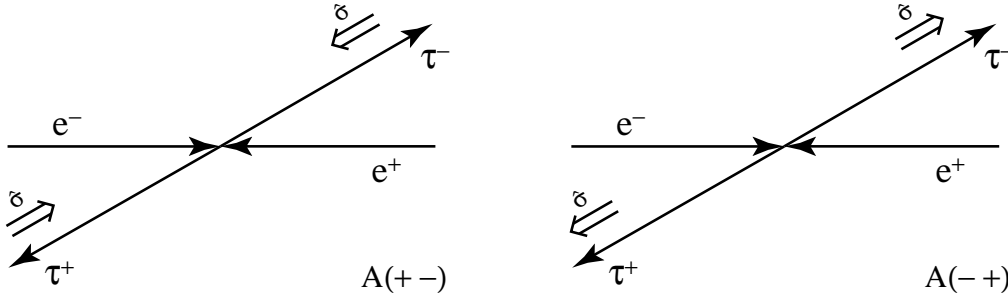
Figure 1-5: The anomalous coupling production amplitudes create tau pairs with their spins opposed. This allows the production of transversely polarized taus.

tau production cross section.

The differential cross section term σ_0 in Equation 1.18 is given by

$$
\begin{aligned}
\sigma_0 &= \chi^{++++} + \chi^{----} + \chi^{++--} + \chi^{--++} \\
&= |\mathcal{A}(++)|^2 + |\mathcal{A}(--)|^2 + |\mathcal{A}(+-)|^2 + |\mathcal{A}(-+)|^2
\end{aligned}
\tag{1.19}
$$

which has a component from both the Standard Model and the anomalous coupling amplitudes. Using the relativistic amplitudes in Table 1.1, the total cross section terms for left and right handed incident electrons are given as

$$
\sigma_0|_L^{SM} = 2g_z^4 E^4 (c_v + c_a)^2 (c_v^2 + c_a^2) \left[(1 + \cos^2\theta) + 2A_\tau \cos\theta \right]
\tag{1.20}
$$

$$
\sigma_0|_R^{SM} = 2g_z^4 E^4 (c_v - c_a)^2 (c_v^2 + c_a^2) \left[(1 + \cos^2\theta) - 2A_\tau \cos\theta \right]
\tag{1.21}
$$

$$
\sigma_0|_L^{anom} = 2g_z^4 E^4 (c_v + c_a)^2 (|k_v|^2 + |k_a|^2) \sin^2\theta
\tag{1.22}
$$

$$
\sigma_0|_R^{anom} = 2g_z^4 E^4 (c_v - c_a)^2 (|k_v|^2 + |k_a|^2) \sin^2\theta,
\tag{1.23}
$$

where the Standard Model and anomalous parts have been written separately, and $A_\tau = 2c_v c_a/(c_v^2 + c_a^2)$ is the SM electroweak asymmetry parameter. Applying Equa-

tion 1.17 to account for the electron beam polarization and re-arranging some terms gives the total differential cross section

$$\frac{d\sigma_0}{d\Omega} \propto (1 + \cos^2\theta) + 2A_\tau \frac{A_e - \mathcal{P}_e}{1 - \mathcal{P}_e A_e} \cos\theta + \left(\frac{|k_v|^2 + |k_a|^2}{c_v^2 + c_a^2}\right) \sin^2\theta. \qquad (1.24)$$

The presence of either anomalous dipole moment will increase the total cross section by a factor proportional to $|d|^2$. This has been noted by a number of authors to provide a constraint on the total magnitude of the anomalous couplings by considering the agreement of the tau partial width $\Gamma(Z \to \tau^+\tau^-)/\Gamma_0$ measured by the LEP collaborations to the Standard Model prediction.[9] While somewhat indirect, this provides a fairly decent limit of

$$\sqrt{|d_\tau|^2 + |\tilde{d}_\tau|^2} < 2.1 \times 10^{-17} \ e \ \text{cm} \qquad (95\% \ C.L.)$$

which sets the scale for the desired sensitivity of the more direct measurement described in this analysis.[10]

The longitudinal ($\hat{\mathbf{z}}$) polarization of the produced tau leptons is a well known feature of the Standard Model. In terms of the production spin density matrix, the longitudinal polarization for the τ^+ and τ^- lepton can be written as

$$\mathcal{P}_z^+ = B_z^+/\sigma_0 = \frac{(\chi^{++++} + \chi^{++--}) - (\chi^{--++} + \chi^{----})}{(\chi^{++++} + \chi^{++--}) + (\chi^{--++} + \chi^{----})} \qquad (1.25)$$

$$\mathcal{P}_z^- = B_z^-/\sigma_0 = \frac{(\chi^{++++} + \chi^{--++}) - (\chi^{++--} + \chi^{----})}{(\chi^{++++} + \chi^{--++}) + (\chi^{++--} + \chi^{----})}, \qquad (1.26)$$

where the denominator is simply the total cross section σ_0 computed above.[5] Again, the numerator can be written in terms of a Standard Model component and an

---

[5] To be completely accurate, the Standard Model component of $\mathcal{P}_z$ is entirely correlated between the two tau hemispheres, and in the notation of Equation 1.18 would show up in the C_{ij} term. What is meant here is the observed polarization if the opposite hemisphere is ignored.

anomalous component as

$$B_z^{\mp}|_L^{SM} = -2g_z^4 E^4 (c_v + c_a)^2 (c_v^2 + c_a^2) \left[A_\tau (1 + \cos^2\theta) + 2\cos\theta \right] \tag{1.27}$$

$$B_z^{\mp}|_R^{SM} = -2g_z^4 E^4 (c_v - c_a)^2 (c_v^2 + c_a^2) \left[A_\tau (1 + \cos^2\theta) - 2\cos\theta \right] \tag{1.28}$$

$$B_z^{\mp}|_L^{anom} = \pm 2g_z^4 E^4 (c_v + c_a)^2 (k_v^\star k_a + k_v k_a^\star) \sin^2\theta \tag{1.29}$$

$$B_z^{\mp}|_R^{anom} = \pm 2g_z^4 E^4 (c_v - c_a)^2 (k_v^\star k_a + k_v k_a^\star) \sin^2\theta, \tag{1.30}$$

resulting in a longitudinal tau polarization given by

$$\mathcal{P}_z^{\mp} = -\frac{A_\tau (1 + \cos^2\theta) + 2\frac{A_e - \mathcal{P}_e}{1 - \mathcal{P}_e A_e}\cos\theta \mp \left(\frac{k_v^\star k_a + k_v k_a^\star}{c_v^2 + c_a^2}\right)\sin^2\theta}{(1 + \cos^2\theta) + 2A_\tau \frac{A_e - \mathcal{P}_e}{1 - \mathcal{P}_e A_e}\cos\theta + \left(\frac{|k_v|^2 + |k_a|^2}{c_v^2 + c_a^2}\right)\sin^2\theta}. \tag{1.31}$$

There is very little information to be gained by searching for anomalous longitudinal tau polarization, since this involves terms of second order in the anomalous coupling parameters k_v and k_a.

The transverse $(\hat{\mathbf{x}}, \hat{\mathbf{y}})$ polarization of the produced tau leptons is much more sensitive to the anomalous coupling terms in the generalized Lagrangian. The Standard Model does predict a small $\hat{\mathbf{x}}$ transverse component resulting from the non-zero tau mass, but this is suppressed with respect to the longitudinal tau polarization by a factor of $\mathcal{O}\left[c_v/(\gamma c_a)\right]$ resulting in a transverse polarization of only a few tenths of a percent. The component of transverse polarization in the production plane can be written in terms of the real part of the spin density matrix as

$$\mathcal{P}_x^+ = B_x^+/\sigma_0 = 2\Re\left(\chi^{+-++} + \chi^{+---}\right)/\sigma_0 \tag{1.32}$$

$$\mathcal{P}_x^- = B_x^-/\sigma_0 = 2\Re\left(\chi^{+++-} + \chi^{--+-}\right)/\sigma_0, \tag{1.33}$$

while the component transverse to the production plane is given by the imaginary

part as

$$\mathcal{P}_y^+ = B_y^+/\sigma_0 = -2\Im\left(\chi^{+-++} + \chi^{+---}\right)/\sigma_0 \tag{1.34}$$

$$\mathcal{P}_y^- = B_y^-/\sigma_0 = -2\Im\left(\chi^{+++-} + \chi^{--+-}\right)/\sigma_0. \tag{1.35}$$

These numerator terms are zero in the Standard Model for the relativistic amplitudes shown in Table 1.1, and can be written in terms of the real and imaginary parts of the anomalous couplings as

$$B_x^\mp|_L = -4g_z^4 E^4 \sin\theta\left[\Re(k_v)(c_a\cos\theta + c_v) \pm \Re(k_a)(c_v\cos\theta + c_a)\right] \tag{1.36}$$

$$B_x^\mp|_R = -4g_z^4 E^4 \sin\theta\left[\Re(k_v)(c_a\cos\theta - c_v) \pm \Re(k_a)(c_v\cos\theta - c_a)\right] \tag{1.37}$$

$$B_y^\mp|_L = -4g_z^4 E^4 \sin\theta\left[\Im(k_v)(c_v\cos\theta + c_a) \pm \Im(k_a)(c_a\cos\theta + c_v)\right] \tag{1.38}$$

$$B_y^\mp|_R = -4g_z^4 E^4 \sin\theta\left[\Im(k_v)(c_v\cos\theta - c_a) \pm \Im(k_a)(c_a\cos\theta - c_v)\right]. \tag{1.39}$$

Dividing out the total cross section σ_0 gives the net transverse tau polarization in the production plane

$$\mathcal{P}_x^\mp = -\Re(k_v)\,\frac{2\sin\theta\,(c_a\cos\theta + c_v\frac{A_e-\mathcal{P}_e}{1-\mathcal{P}_e A_e})/(c_v^2+c_a^2)}{(1+cos^2\theta) + 2A_\tau\frac{A_e-\mathcal{P}_e}{1-\mathcal{P}_e A_e}\cos\theta + \left(\frac{|k_v|^2+|k_a|^2}{c_v^2+c_a^2}\right)\sin^2\theta}$$

$$\mp\,\Re(k_a)\,\frac{2\sin\theta\,(c_v\cos\theta + c_a\frac{A_e-\mathcal{P}_e}{1-\mathcal{P}_e A_e})/(c_v^2+c_a^2)}{(1+\cos^2\theta) + 2A_\tau\frac{A_e-\mathcal{P}_e}{1-\mathcal{P}_e A_e}\cos\theta + \left(\frac{|k_v|^2+|k_a|^2}{c_v^2+c_a^2}\right)\sin^2\theta}, \tag{1.40}$$

and transverse to the production plane

$$\mathcal{P}_y^\mp = -\Im(k_v)\,\frac{2\sin\theta\,(c_v\cos\theta + c_a\frac{A_e-\mathcal{P}_e}{1-\mathcal{P}_e A_e})/(c_v^2+c_a^2)}{(1+\cos^2\theta) + 2A_\tau\frac{A_e-\mathcal{P}_e}{1-\mathcal{P}_e A_e}\cos\theta + \left(\frac{|k_v|^2+|k_a|^2}{c_v^2+c_a^2}\right)\sin^2\theta}$$

$$\mp\,\Im(k_a)\,\frac{2\sin\theta\,(c_a\cos\theta + c_v\frac{A_e-\mathcal{P}_e}{1-\mathcal{P}_e A_e})/(c_v^2+c_a^2)}{(1+\cos^2\theta) + 2A_\tau\frac{A_e-\mathcal{P}_e}{1-\mathcal{P}_e A_e}\cos\theta + \left(\frac{|k_v|^2+|k_a|^2}{c_v^2+c_a^2}\right)\sin^2\theta}. \tag{1.41}$$

Substituting back in the original definition of the dipole moments, this can be written
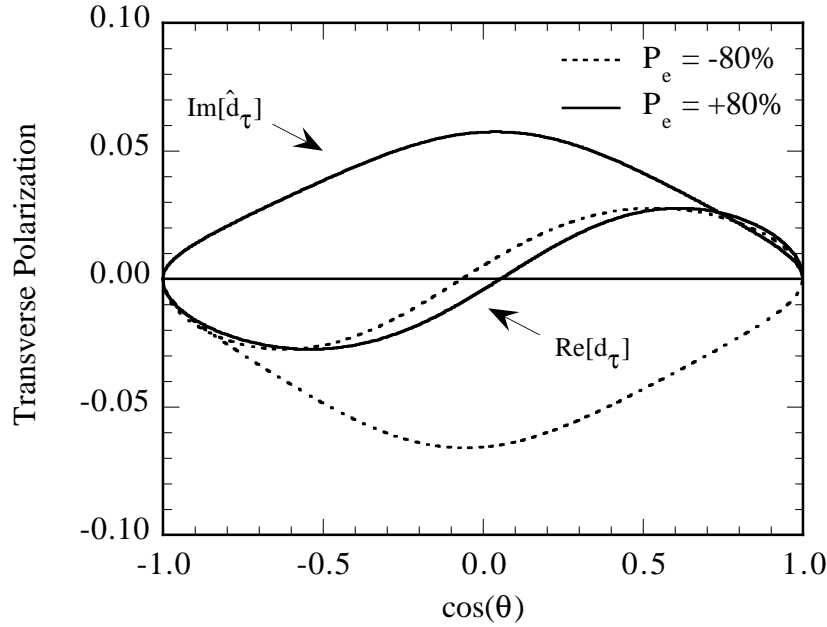
Figure 1-6: The transverse τ^- polarization in the production plane $(\mathcal{P}_x^-)$ is shown as a function of the production angle for a non-zero $\Re[d_\tau]$ and $\Im[\tilde{d}_\tau]$. In each case a dipole strength of 1×10^{-17} e cm is shown for both left and right polarized electron beams.

more compactly as

$$
\begin{array}{rcl}
\mathcal{P}_x^\mp & = & -\frac{\sqrt{s}}{g_z}\left[\Re(d_\tau)f_1(\theta) \mp \Im(\tilde{d}_\tau)f_2(\theta)\right] \\[2mm]
\mathcal{P}_y^\mp & = & -\frac{\sqrt{s}}{g_z}\left[\Im(d_\tau)f_2(\theta) \pm \Re(\tilde{d}_\tau)f_1(\theta)\right],
\end{array}
\tag{1.42}
$$

where in the limit of small anomalous couplings such that the anomalous contribution to the total cross section can be ignored, $f_1(\theta)$ and $f_2(\theta)$ depend only upon the Standard Model couplings (c_v, c_a), the electron beam polarization $(\mathcal{P}_e)$, and the production angle (θ).

As shown in Figure 1-6, the first angular function

$$
f_1(\theta) = \frac{2\sin\theta \ (c_a\cos\theta + c_v\frac{A_e - \mathcal{P}_e}{1 - \mathcal{P}_e A_e})/(c_v^2 + c_a^2)}{(1 + \cos^2\theta) + 2A_\tau\frac{A_e - \mathcal{P}_e}{1 - \mathcal{P}_e A_e}\cos\theta + (\sqrt{s}/g_z)^2\left(\frac{|d_\tau|^2 + |\tilde{d}_\tau|^2}{c_v^2 + c_a^2}\right)\sin^2\theta}
\tag{1.43}
$$

is a nearly odd function of $\cos\theta$ which describes the transverse polarization resulting
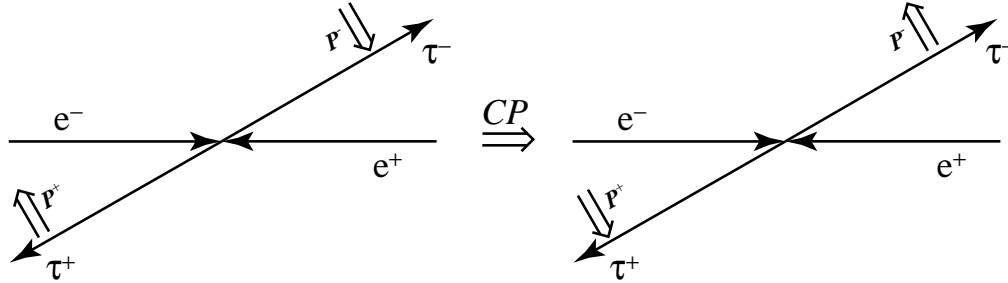
Figure 1-7: The transverse polarizations induced by the Weak Electric Dipole Moment
($\tilde{d}_\tau$) reverse under the CP operation resulting in a different polarization
configuration. This is a CP violating interaction.

from the real part of either dipole moment, while the second angular function

$$f_2(\theta) = \frac{2\sin\theta \ (c_v\cos\theta + c_a\frac{A_e - \mathcal{P}_e}{1 - \mathcal{P}_e A_e})/(c_v^2 + c_a^2)}{(1 + cos^2\theta) + 2A_\tau\frac{A_e - \mathcal{P}_e}{1 - \mathcal{P}_e A_e}\cos\theta + (\sqrt{s}/g_z)^2\left(\frac{|d_\tau|^2 + |\tilde{d}_\tau|^2}{c_v^2 + c_a^2}\right)\sin^2\theta} \qquad (1.44)$$

is a nearly even function of $\cos\theta$ which describes the transverse polarization resulting
from the imaginary part. In the limit of large electron polarization ($|\mathcal{P}_e| \to 1$), a
reversal of the electron beam polarization is equivalent to a parity reversal of these
functions:

$$f(\cos\theta, \mathcal{P}_e) \approx -f(-\cos\theta, -\mathcal{P}_e). \qquad (1.45)$$

This can be seen in Figure 1-6 to have a dramatic effect on the transverse polariza-
tion resulting from the imaginary parts of the anomalous couplings, while changing
very little the transverse polarization resulting from the real parts. The benefit to
this analysis of the polarized electron beam available at the SLC is this increased
sensitivity to the imaginary parts of the anomalous coupling terms.

From Equation 1.42 the CP nature of the two dipole moments originally dis-

cussed in Section 1.3 can be directly seen. The transverse polarization which results from both the real and imaginary parts of the WEDM ($\tilde{d}_\tau$) is opposite for the τ^+ and τ^- leptons. Remembering that the same coordinate system is used for both tau hemispheres, this results in polarization vectors which are opposed to each other for the two leptons. Under the CP operation, the polarizations of the two tau leptons are exchanged, and any difference between these two polarization vectors directly violates CP invariance. The WMDM ($\tilde{d}_\tau$), meanwhile, produces a transverse polarization which is the same for both the τ^+ and τ^- leptons, resulting in polarization vectors which are invariant under the CP operation.

1.5   Tau Decay Spectra

The technique of using the momentum spectra of the tau lepton decay products to spin analyze the underlying tau state is well established in particle physics. At LEP, for instance, the longitudinal polarization of the tau leptons is measured in this fashion as a function of the production angle, and used to fit for the Standard Model coupling parameters using Equation 1.31.[6] In this analysis, the tau decay spectra will be used to analyze both the longitudinal and transverse tau polarizations as a function of production angle, and used to fit for the strengths of the anomalous coupling parameters. It is assumed in this analysis that any possible new physics enters at the $Z \rightarrow \tau^+\tau^-$ vertex, and the subsequent decay of the tau leptons is accurately described by the Standard Model charged current interaction.[7]

In the tau rest frame, the partial width for a particular tau decay can be written in terms of a spin independent decay function $f(\mathbf{q}^\star)$ and a spin dependent decay

---

[6] See [9] and the references contained therein.

[7] It has recently been noted by T. Rizzo that gauge invariance would require a similar anomalous coupling to be present at the charged current $W \rightarrow \tau\nu$ vertex. The effect of this additional charged current anomalous coupling on the observed tau decay spectra is very small, however.[11]

Table 1.2: Tau Decay Spin Analyzing Powers

Decay Mode	Analyzing Power
$\tau^- \to \pi^- \nu_\tau$	+1
$\tau^- \to e^- \bar{\nu}_e \nu_\tau$	-1/3
$\tau^- \to \mu^- \bar{\nu}_\mu \nu_\tau$	-1/3
$\tau^- \to \pi^- \pi^0 \nu_\tau$	-0.06

function $g(\mathbf{q}^\star)$ as

$$
\begin{aligned}
\frac{d\Gamma}{d\mathbf{q}^\star}(\tau^- \to b(\mathbf{q}^\star) + X) &\propto f_b(\mathbf{q}^\star) + g_b(\mathbf{q}^\star)\, \hat{\sigma} \cdot \hat{\mathbf{q}}^\star \\
\frac{d\Gamma}{d\mathbf{q}^\star}(\tau^+ \to a(\mathbf{q}^\star) + X) &\propto f_a(\mathbf{q}^\star) - g_a(\mathbf{q}^\star)\, \hat{\sigma} \cdot \hat{\mathbf{q}}^\star
\end{aligned}
\tag{1.46}
$$

where $\hat{\sigma}$ represents the tau spin direction and $\mathbf{q}^\star$ is the momentum of the observed tau decay product in the tau rest frame.[12] Not all tau decays retain much useful spin information about the underlying tau lepton, and in this analysis only two single-prong hadronic decay modes, $\tau \to \pi \nu_\tau$ and $\tau \to \rho \nu_\tau$, along with the two leptonic decays $\tau \to e\bar{\nu}_e\nu_\tau$ and $\tau \to \mu\bar{\nu}_\mu\nu_\tau$ will be identified and analyzed. For these four decay modes, the decay functions f and g depend only upon the scaled energy $(x^\star = 2E^\star/m_\tau)$ of the observed charged track in the tau rest frame. An estimate of the sensitivity of each decay mode can be made by considering the inclusive analyzing power

$$
\alpha = \int g(x^\star)/f(x^\star)dx^\star
\tag{1.47}
$$

as shown in Table 1.2. In actuality, somewhat better sensitivities are achieved when the full $x^\star$ dependence of the decay functions are explicitly considered, although experimental effects like backgrounds and resolution will degrade this sensitivity somewhat.

The tau decay matrix $\mathcal{D}(\mathbf{q}^\star_\mp)$ is proportional to the tau decay partial widths given in Equation 1.46 written explicitly in the Pauli spin space of the chosen tau

spin basis as

$$\mathcal{D}(\mathbf{q}^\star_\mp) = \begin{pmatrix} f(x^\star) \pm g(x^\star)\cos\theta^\star & \pm g(x^\star)\sin\theta^\star e^{-i\phi^\star} \\ \pm g(x^\star)\sin\theta^\star e^{+i\phi^\star} & f(x^\star) \mp g(x^\star)\cos\theta^\star \end{pmatrix}, \tag{1.48}$$

where $\theta^\star$ and $\phi^\star$ are the polar and azimuthal angles between the the momentum vector $\mathbf{q}^\star_\mp$ and the $+\hat{\mathbf{z}}$ axis in the $\tau^\mp$ center of mass frame. In this form, the decay spectrum for a polarized tau can be written as

$$\frac{d^3\Gamma}{dx^\star d\Omega^\star} \propto (\mathbf{1} + \mathcal{P}_i\hat{\sigma}_i)\cdot\mathcal{D}(\mathbf{q}^\star), \tag{1.49}$$

and by contracting both decay matrices with the production spin density matrix χ, the multi-differential cross section can be obtained. The advantage of this notation is that $\mathcal{D}(\mathbf{q}^\star)$ depends only upon Standard Model parameters and encapsulates all of the physics governing the particular tau decay mode, while χ contains all of the dependence upon the anomalous couplings and is completely independent of the tau decay mode.

Appendix A describes in detail the process of changing variables from the tau center of mass frame to the lab frame, and writing the matrix $\mathcal{D}(\mathbf{q}^\star)$ in terms of the experimentally accessible variables x and ϕ, which are the scaled energy and azimuthal decay angle of the single observed charged particle from each tau lepton decay in the lab frame.

1.6   Likelihood Fitting

The strengths of the anomalous couplings are found by performing a likelihood fit to the observed hemisphere decay observables $(x^+, x^-, \phi^+, \phi^-)$ at a given production angle and electron polarization $(\cos\theta, \mathcal{P}_e)$ as a function of the anomalous coupling

parameters $(d_\tau, \tilde{d}_\tau)$. The likelihood of each observed event is given by

$$\mathcal{L}(d_\tau, \tilde{d}_\tau | \cos\theta, \mathcal{P}_e, x^+, \phi^+, x^-, \phi^-) =$$
$$\tilde{\chi}^{\alpha'\alpha\beta'\beta}(d_\tau, \tilde{d}_\tau | \cos\theta, \mathcal{P}_e) \, \mathcal{D}^{\alpha'\alpha}(x^+, \phi^+) \, \mathcal{D}^{\beta'\beta}(x^-, \phi^-), \quad (1.50)$$

where $\mathcal{D}(x, \phi)$ is the tau decay matrix for a given identified tau hemisphere, and $\tilde{\chi}$ is the normalized production spin density matrix given by

$$\tilde{\chi}^{\alpha'\alpha\beta'\beta} = \chi^{\alpha'\alpha\beta'\beta} / (\chi^{\alpha'\alpha\beta'\beta}\delta_{\alpha'\alpha}\delta_{\beta'\beta}), \quad (1.51)$$

such that the likelihood of each event is normalized over the phase space of all possible decay parameters $(x^+, x^-, \phi^+, \phi^-)$:

$$\int \mathcal{L}(d_\tau, \tilde{d}_\tau | \cos\theta, \mathcal{P}_e, x^+, \phi^+, x^-, \phi^-) \, dx^+ d\phi^+ dx^- d\phi^- = 1. \quad (1.52)$$

Normalized in this fashion, the likelihood of the observed data depends only upon the net spin polarization of the produced tau pairs, and not upon the total rate of tau production as a function of the production angle $\cos\theta$. From Equation 1.24 it can be seen that the differential cross section $d\sigma_0/d\Omega$ has a very weak dependence on the strength of the anomalous coupling terms. Without this normalization, any difference between the observed and expected event rate as a function of the production angle $\cos\theta$ will cause the likelihood fit to favor very large values for the the anomalous coupling strengths in an attempt to modify the overall shape of the differential cross section. Any slight misunderstanding of the detector acceptance can cause these small deviations, and the associated uncertainty becomes greatly magnified in the final determination of the anomalous coupling strengths. Since there is very little physics information to be gained by including this small cross section dependency anyway, it is far better to divide this information out as shown in Equation 1.50.

Chapter 2 presents the equipment used in this analysis, and Chapter 3 explains the measurement of the electron beam polarization in detail. Chapter 4 describes the process of selecting and identifying the tau lepton decays using the SLD detector, while Chapter 5 contains a more complete description of the likelihood formalism including modifications to Equation 1.50 to account for the imperfect identification and reconstruction of the various tau decay products. The results and a discussion of the systematic uncertainties is found in Chapter 6.

Chapter 2

The Machine

The pursuit of knowledge in particle physics has, over the past few decades, taken on a truly inhuman scale. Both in terms of the physical size of the equipment and the human effort necessary, a modern particle physics experiment requires the participation and collaboration of many hundreds of physicists, engineers and support staff. For this reason, a comprehensive description of the equipment used in this analysis is beyond the scope of this document. Rather, this chapter will give a broad overview of the equipment and techniques used in the production and detection of polarized Z bosons at the SLC.

2.1 SLAC Linear Collider

The SLAC Linear Collider represents a major achievement in particle accelerator technology. The first and only high energy linear collider, at the SLC single bunches of electrons and positrons are accelerated together down a two-mile linear accelerator and brought into collision at the center of the SLD detector at a rate of 120 Hz. Officially proposed in 1980[13] as a quick and low-cost alternative to the massive storage ring design of LEP, the SLC has endured a somewhat rocky past, including
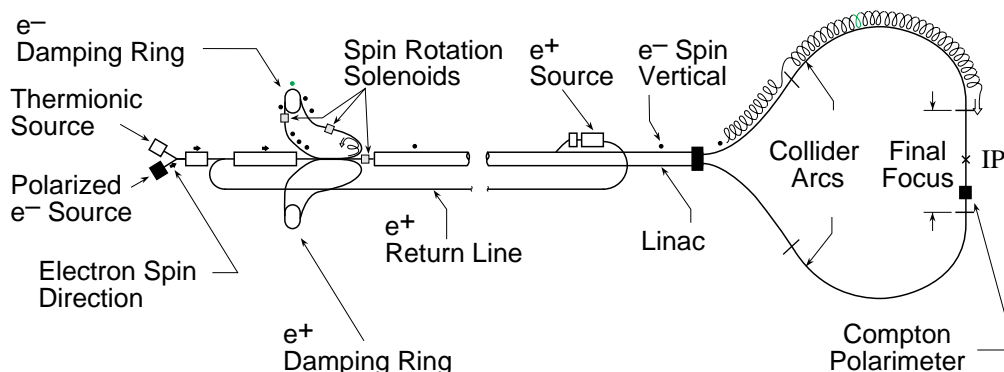
Figure 2-1: The layout of the SLC is shown. The spin of the polarized electron beam
is indicated by the small arrows along the way. Not shown are the beam
dumps, which are just past the outgoing final focus section.

the 1989 Loma Prieta earthquake, but has proven to be a useful research tool in its
ability to accelerate polarized electrons.

The layout of the SLC is shown in Figure 2-1. Two bunches of polarized elec-
trons are produced by photoemission from a strained gallium arsenide cathode and
injected into the head of the linac.[14] After a short acceleration section, the 1.2 GeV
electron bunches are injected into the North Damping Ring (NDR) where the phase
space (emittance) of the beam is reduced.[15] After a damping time of 8.3 ms, the
electrons are extracted from the NDR and injected, along with a bunch of positrons
from the South Damping Ring (SDR), into the main accelerating section of the
linac. Two thirds of the way down the linac, the trailing electron bunch is stripped
off to the positron target, a thick water-cooled chunk of tungsten,[16] to produce the
positrons used on the following machine cycle. These positrons are brought back
up to the head of the linac in a separate beamline and injected into the SDR where
they are stored for 16.6 ms waiting for the next machine cycle. After acceleration
to around 46.5 GeV, the electron and positron bunches are separated in the beam
switchyard and fed into the North and South arcs respectively. The 5.6 kGauss
dipole magnetic fields in the arcs bend the two beams with a 279 m effective radius,
loosing nearly 1 GeV each to synchrotron radiation in the process, and bring them

Table 2.1: SLC Collision Beam Parameters

Parameter		1993 Run	1994-95 Run
Horizontal beam size	σ_x	2.6 μm	2.1 μm
Vertical beam size	σ_y	0.8 μm	0.6 μm
Horizontal divergence	$\sigma_{x'}$	300 μRad	300 μRad
Vertical divergence	$\sigma_{y'}$	200 μRad	200 μRad
Energy divergence	σ_E/E	0.30%	0.15%
Bunch intensity	$n_{e\pm}$	3.0×10^{10}	3.5×10^{10}
Electron polarization	$\mathcal{P}_e$	$(63.0 \pm 1.1)\%$	$(77.2 \pm 0.5)\%$
Total Luminosity	$\mathcal{L}_{tot}$	1.6 pb^{-1}	3.5 pb^{-1}

Typical single beam parameters at the SLC interaction point are listed for the 1993 and 1994-95 running periods. The beam sizes and divergences shown represent single bunch RMS values. The electron beam polarization is luminosity weighted over the course of each running period, while the error represents the overall systematic uncertainty.

to the final focus section and the SLD detector.[17] In the final focus, the two beams are compressed by a pair of superconducting quadrupole triplets to a FWHM size of roughly 4 x 2 μm^2 at the center of the SLD detector where the collision takes place. Most of the beam continues unscathed, traveling upstream through the opposing final focus elements until they are kicked out of the main beamline and dumped.

2.1.1 Polarized Electron Source

It has long been known that polarized electrons can be photoemitted from the surface of a semiconductor, but through the use of a strained-lattice GaAs photocathode, polarizations in excess of 80% have been achieved at the SLC.[18] Figure 2-2 shows the energy levels at the top of the valence band and the bottom of the conduction band in strained gallium arsenide (GaAs). An incident circularly polarized photon near the band gap energy of 1.52 eV will excite only the transitions from the top of the valence band into the conduction band as shown. In conventional GaAs, two transitions producing opposite spin electrons are possible from the degenerate
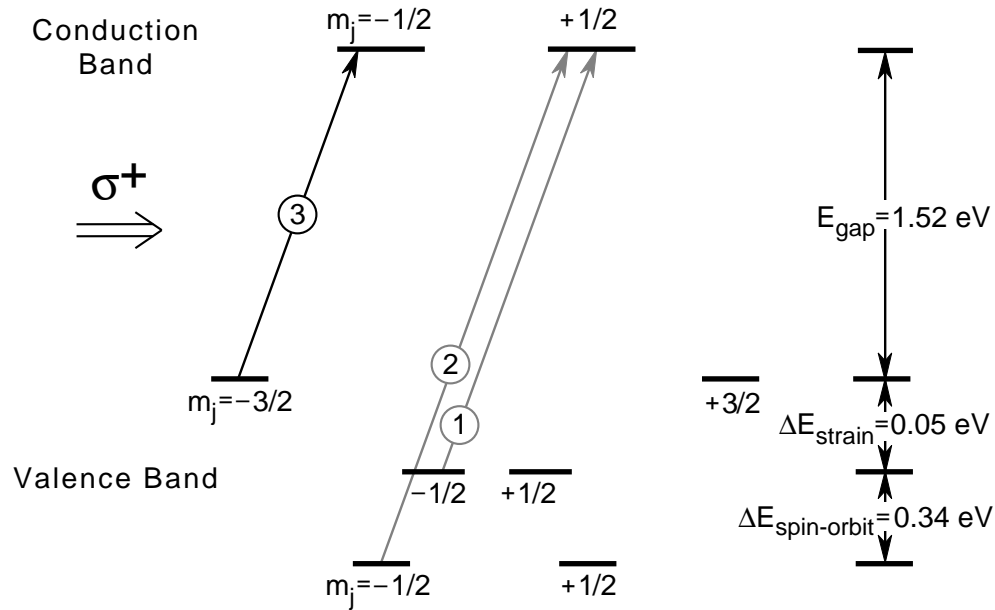
Figure 2-2: The energy levels are shown at the top of the valence band and the bottom of the conduction band for conventional (top) and strained (bottom) Gallium Arsenide. The Clebsh-Gordon coefficients for the various spin transitions are also shown for a right handed incident photon. In bulk GaAs, spin-orbit interactions separate the $P_{1/2}$ and $P_{3/2}$ energy levels to provide a maximum polarization of 50%. With a strained lattice, the degenerate $P_{3/2}$ energy levels can also be separated and a polarization of nearly 100% can be achieved.

$P_{3/2}$ energy level at a rate of 3 to 1 as given by the Clebsh-Gordon coefficients. By growing a small layer of GaAs on top of a substrate of gallium arsenide phosphide (GaAsP), which has a different lattice spacing than bulk GaAs, the degeneracy in the $P_{3/2}$ energy levels can be broken and polarizations above 50% can be achieved. The exact dimensions of the various cathode layers has a significant effect on the performance of the source, and an improvement in the beam polarization from 63% in 1993 to over 77% in 1994 can be directly attributed to reducing the active layer from 300 μm to 100 μm in thickness.[19]

By applying a thin coating of cesium to the face of the photocathode, the work function of the surface can be reduced, and a modest voltage will extract the polarized electrons from the conduction band. Applying cesium improves the quantum

efficiency for producing electrons from the cathode, but as more charge is extracted there is a corresponding loss in net beam polarization. To provide the 6×10^{10} electrons needed to drive the SLC, the cathode is maintained near a QE of 0.4%.

A pair of YAG pumped Ti:Sapphire lasers provide linearly polarized photons which are circularly polarized by use of a of Pockels Cell. These electro-optic crystals can be used to select left or right handed light on a pulse by pulse basis by reversing the drive voltage applied. In normal SLC operations the polarization of the incident photons, and hence the polarization of the produced electrons, are selected by a pseudo-random sequence on each machine cycle in an effort to average out any periodicities in the accelerator performance between the two polarization states. The wavelength of the drive laser is empirically set near 850 nm to maximize the polarization of the produced electrons.

2.1.2   Linear Accelerator

The linear accelerator (*linac*) used at the SLC is a 3 km long sequence of 30 conventional copper S-band waveguides each driven by eight 60 MWatt peak power RF klystrons. An accelerating gradient of 17 MeV/m is achieved in the copper structures, providing a possible single beam energy of up to 50 GeV.

2.1.3   Spin Transport

Electrons are produced longitudinally polarized at the source, and special care must be taken to preserve this polarization as the electrons travel through the accelerator to the SLD. In a magnetic field, the spin precession of a relativistic particle is described by the BMT equation,[1] which for planar motion through a transverse

---

[1] See any graduate-level electromagnetism text.
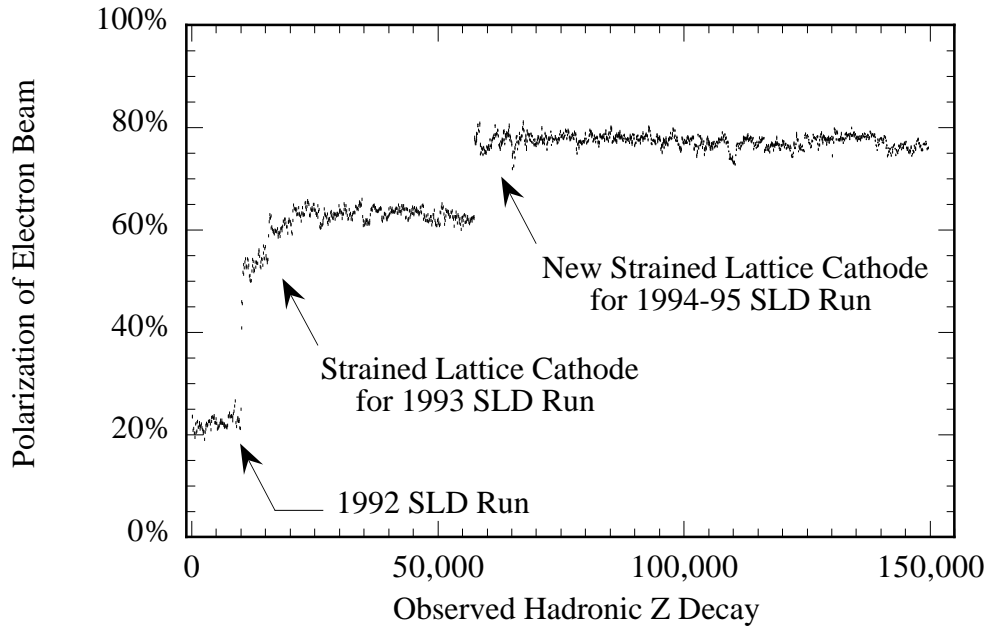
Figure 2-3: The polarization history of the SLC is shown. The measured electron beam
polarization is plotted versus the number of hadronic Z decays observed.

bending field can be written as

$$\frac{d\theta_{spin}}{d\theta_{bend}} = \gamma \frac{g-2}{2}, \tag{2.1}$$

where θ_{spin} is the precession angle of the component of the spin vector perpendic-
ular to the magnetic field with respect to the momentum vector, and θ_{bend} is the
revolution angle of the particle along its circular path in the bending plane. Note
that if g were exactly equal to 2, the longitudinal polarization of an electron would
be maintained as the precession frequency would exactly match the cyclotron fre-
quency. Alternately, for a mono-energetic beam of electrons at some integer multiple
of the 'magic energy' $\gamma = \frac{2n}{g-2}$, the spin orientation at any particular point along the
circular beam orbit will remain unchanged during subsequent revolutions. This is,
in fact, the technique used to measure the muon magnetic moment to high precision.

Because this spin precession is energy dependent, and the SLC electron bunch
always has some energy width, any polarization component lying in the bending

plane as the electrons enter the North damping ring will be quickly averaged away to zero. To preserve the electron polarization, the combination of a 164° bend followed by a 6.34 Tesla-meter solenoidal magnetic field region are used to precess the incoming electron polarization vector first transverse to the direction of motion, and then up into the vertical plane. Because this spin rotation was designed for a 1.21 GeV incident electron bunch, but the actual injection is performed at 1.19 GeV, the spin rotation transverse to the bending plane is not perfect. This results in a 1% polarization loss by the time the electrons are extracted from the NDR.

An additional pair of spin rotation solenoids were built to allow arbitrary control of the polarization vector at the SLD, however these have not been used since the advent of *flat beam* running in 1993. A significant increase in luminosity was realized by abandoning a symmetric beam profile and colliding at the SLD with beams which are much broader in the horizontal plane.[20] As a result, however, any solenoidal fields after the damping rings, where the flat beams are created, introduce skew correlations between the horizontal and vertical planes which are generally undesirable. As a result, the electron polarization is left in the vertical plane through the acceleration process, and the magnetic fields in the North arc are used to align the final polarization vector at the SLD.

The mechanism for aligning the electron polarization in the arcs is colloquially known as *spin bumps*.[21] The SLC North arc is composed of 23 achromats, each containing 20 combined function magnets to provide both bending and focusing of the beam. Due to a design flaw, the spin precession frequency in each achromat is nearly resonant with the betatron oscillation frequency.[2] As shown in Figure 2-4, this near resonance can be exploited to precess the polarization vector out of the vertical plane and into the horizontal plane. Two large betatron oscillations, or spin bumps, are applied to the electron beam late in the arc to rotate the polarization

---

[2] Betatron oscillations are the vertical displacements from the ideal orbit the electrons experience as they are corrected by the quadrupole focusing fields.
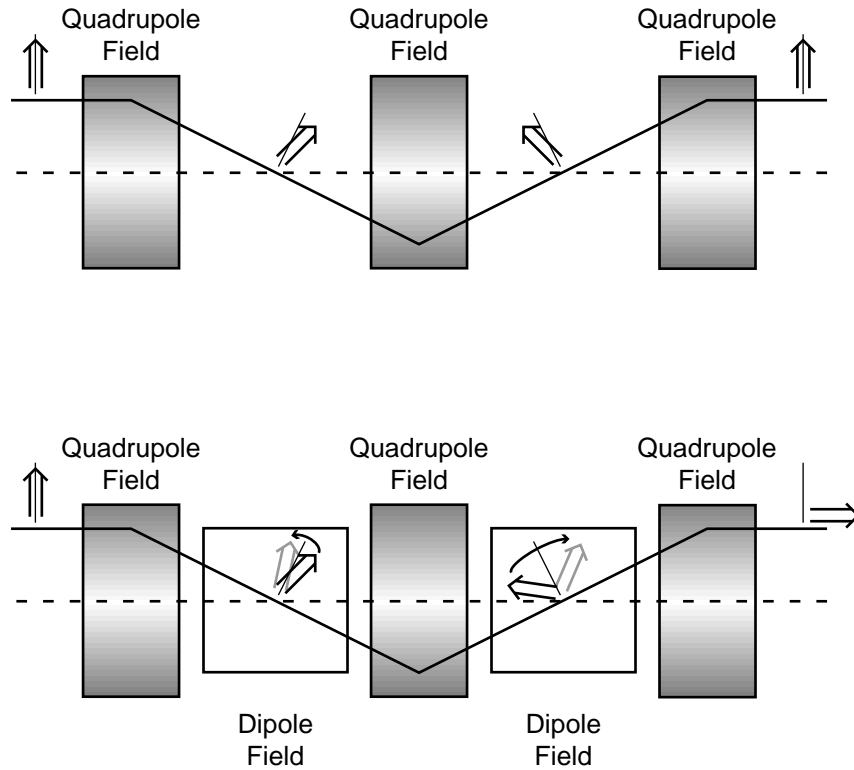
Figure 2-4: The spin orientation of a vertically polarized electron is schematically shown. The first example shows vertical betatron oscillation through a chain of quadrupoles. The spin precession induced by every quad element cancels out preserving the original spin orientation. In the second example, the intermediate vertical dipole fields precess the spin vector so that the next quad precession adds coherently. In this manner, the spin vector can be rotated into the dipole bending plane. The rate of this rotation depends upon the amplitude of the vertical oscillation.

vector into the bending plane where it begins precessing. The amplitude of these two bumps is phenomenologically chosen to maximize the longitudinal polarization at the SLD.

Because the spin precession frequency is energy dependent, the longitudinal polarization of the electron bunch at the SLD is also energy dependent, which causes some problems as discussed in Chapter 3. This energy dependency grows with the number of spin precessions experienced by the electrons in the North arc, so by keeping the spin orientation vertical for as long as possible the magnitude of this ef-
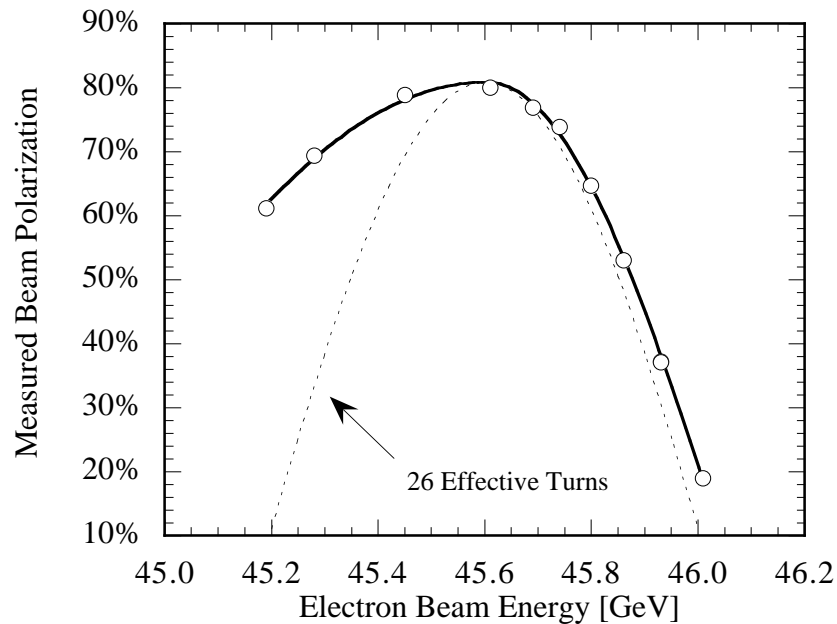
Figure 2-5: The energy dependence of the electron beam polarization was directly measured a number of times during the 1994-95 SLD run. This particular scan was taken in February 1995, near the end of the run. The measured polarization dependence (circles) is weaker than the dependence expected from the spin precession of an electron bunch launched into the arc horizontally polarized (dashed line).

fect can be reduced. At 46 GeV, the spin of an electron launched into the North arc longitudinally polarized will precess a total of 26 times over the net 90 degree bend. Unfortunately, the SLC arcs are not flat, but rather were constructed to follow the bumps and rolls of the surrounding terrain. This convoluted geometry makes an accurate prediction of the spin dynamics through the North arc spin bumps nearly impossible to simulate, and direct measurements must be made. A second set of spin bumps, set earlier in the North arc, are used to reduce the observed polarization dependence on beam energy. A polarization versus energy scan, shown in Figure 2-5, shows an effective turn number of 12 on the low energy side, although the high energy side shows a much steeper dependence with an effective turn number of 24. As shown, the longitudinal electron polarization is maximized at the beam collision energy near 45.6 GeV.

2.1.4   Energy Spectrometer

The beam energy at the SLC is measured on each machine pulse with a pair of wire imaging synchrotron radiation detectors (WISRD).[22] These devices are located in the extraction lines immediately before the beam dumps. Each WISRD consists of three dipole magnets and a pair of copper wire screens. The vertical separation between the synchrotron light swaths emitted by the beam in the first and third horizontally bending dipoles is measured by the wire arrays. Combined with the precisely measured field strength of the intermediate vertically bending analyzing dipole, the beam energy can be deduced. On each machine cycle, the instantaneous energy of each beam can be determined to an error of 22 MeV, which is dominated by electronics noise. Averaging over many beam pulses, this error can be reduced to about 12 MeV per beam where the remaining irreducible error is dominated by the uncertainty in the wire plane geometry and orientation. Taking this error to be correlated between the two detectors results in a 25 MeV total error on the center of mass collision energy at the SLD. The energy measured for each beam at the WISRD must be corrected by +45 MeV to account for synchrotron radiation losses between the SLD and the dump, and by +5 MeV to account for additional photons radiated in beam-beam interactions related to the collision process. The luminosity weighted center of mass collision energy for the 1993 and 1994-95 running periods was measured to be (91.26 ± 0.02) GeV and (91.28 ± 0.02) GeV respectively.

2.2   Compton Polarimeter

Located 33 meters downstream from the SLD, the Compton polarimeter is the primary instrument used in measuring the electron beam polarization at the SLC. A circularly polarized 2.33 eV photon beam is Compton scattered off the exiting 45.6 GeV electron bunch just before the beam enters the first set of dipole magnets of the SLC South arc heading towards the electron beam dump. These magnets
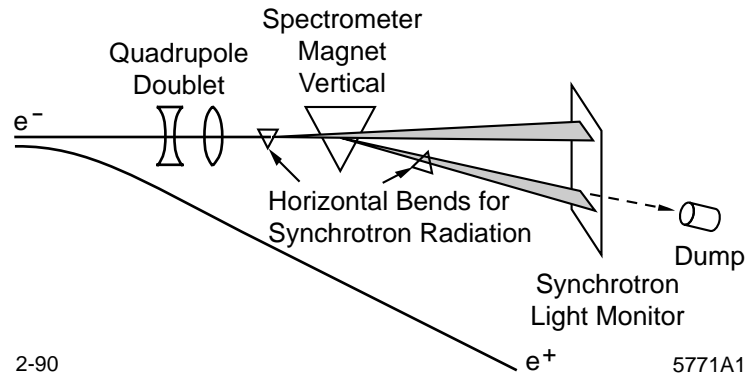
Figure 2-6: The layout of the WISRD energy spectrometer is shown.

act as a spectrometer sweeping the scattered electrons out of the main SLC beam line and into a multichannel Cherenkov detector where the momentum spectrum of the electrons is measured in the interval from 17 to 30 GeV/c. Data from the Compton polarimeter are acquired continuously during normal operations of the SLC, providing a $\sim 1\%$ statistical measurement of the electron beam polarization approximately every three minutes. The calibration and analysis of the Compton polarimeter data will be described in more detail in Chapter 3.

2.2.1   Compton Laser

The scattering 'target' used in the Compton polarimeter is a ~ 30 mJ per pulse beam of circularly polarized photons produced at 532 nm by a Q-switched, frequency doubled Nd:YAG laser running at 17 Hz. The circular polarization state of the photon target is selected with a pair of Pockels Cells similar to those used at the electron source, and the polarization of the laser at production is measured with a series of diagnostic photodiodes installed on the laser bench. The laser beam is brought down into the SLC South final focus tunnel through a vent shaft by means of a transport line consisting of four pairs of phase-compensated mirrors. The photons enter the SLC beamline through a low birefringence window, and collide with the
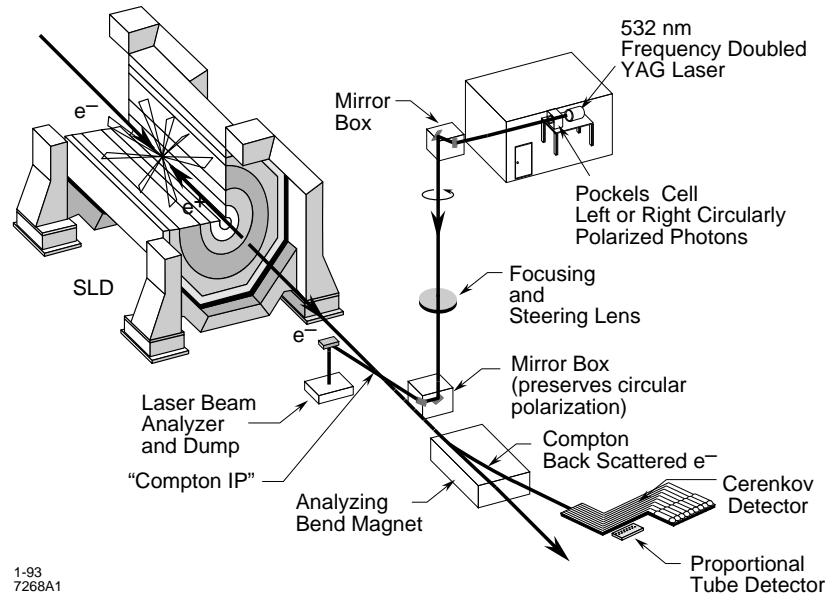
Figure 2-7: The components of the Compton Polarimeter are shown.

outgoing electrons at a crossing angle of 10 mRad. The timing of the 8 ns long laser pulse must be carefully maintained to optimally coincide with the 3 ps long electron bunch, and a series of lenses and other optical elements are used to keep the ~ 1 mm in diameter photon beam centered on the outgoing $\sim (1.0 \times 0.4)$ mm^2 electron bunch. The laser beam continues out of the SLC vacuum enclosure and into an analysis box in the SLC tunnel where the polarization of the photons can be analyzed on a series of photodiodes.

2.2.2　Electron Transport

Due to the large boost from the incident 45.6 GeV electron bunch, the scattered electrons remain with the main outgoing beam until the first bending element of the SLC South arc is reached. The Compton scattering cone in the lab frame of ~ 10 μRad is, in fact, insignificant when compared to the ~ 80 μRad horizontal and ~ 25 μRad vertical beam divergence at the Compton interaction point. Two dipole
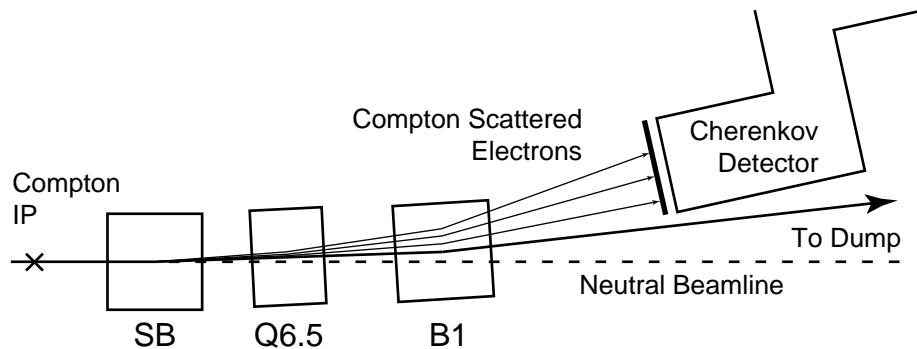
Figure 2-8: The spectrometer used in the Compton polarimeter is shown. The Q6.5
quadrupole was added before the 1994-95 run as part of an SLC final focus
upgrade. This figure is not drawn to scale.

and one quadrupole magnet are used as an analyzing field to sweep the scattered
electrons out of the main SLC beam line, exiting the SLC vacuum enclosure through
a thin stainless steel window, and into the Compton Cherenkov Detector (CKV).

The path of the Compton scattered electrons through the spectrometer elements
and into the CKV detector is shown schematically in Figure 2-8. The exact param-
eters of the spectrometer beam elements are listed in Table B.3.

2.2.3   Compton Cherenkov Detector

Shown in Figure 2-9, the CKV is a segmented threshold Cherenkov counter with
nine readout channels instrumented with Hamamatsu R1398 photomultiplier tubes.
Originally filled with *cis*- and *trans*-2-butene, the radiating gas was changed near the
start of the 1994 run to propane which provides better resistance to radiation dam-
age and polymerization which was believed to be fouling the detector in 1993. At a
slight overpressure of 1.1 atmospheres, this gas provides a Cherenkov threshold for
relativistic electrons at roughly 10 MeV which is crucial for avoiding the abundance
of low energy (< 2 MeV) background associated with the main electron beam. Rela-
tivistic electrons passing through the CKV detector produce UV Cherenkov photons
at a characteristic polar angle of 55 mRad which are reflected by thin aluminum
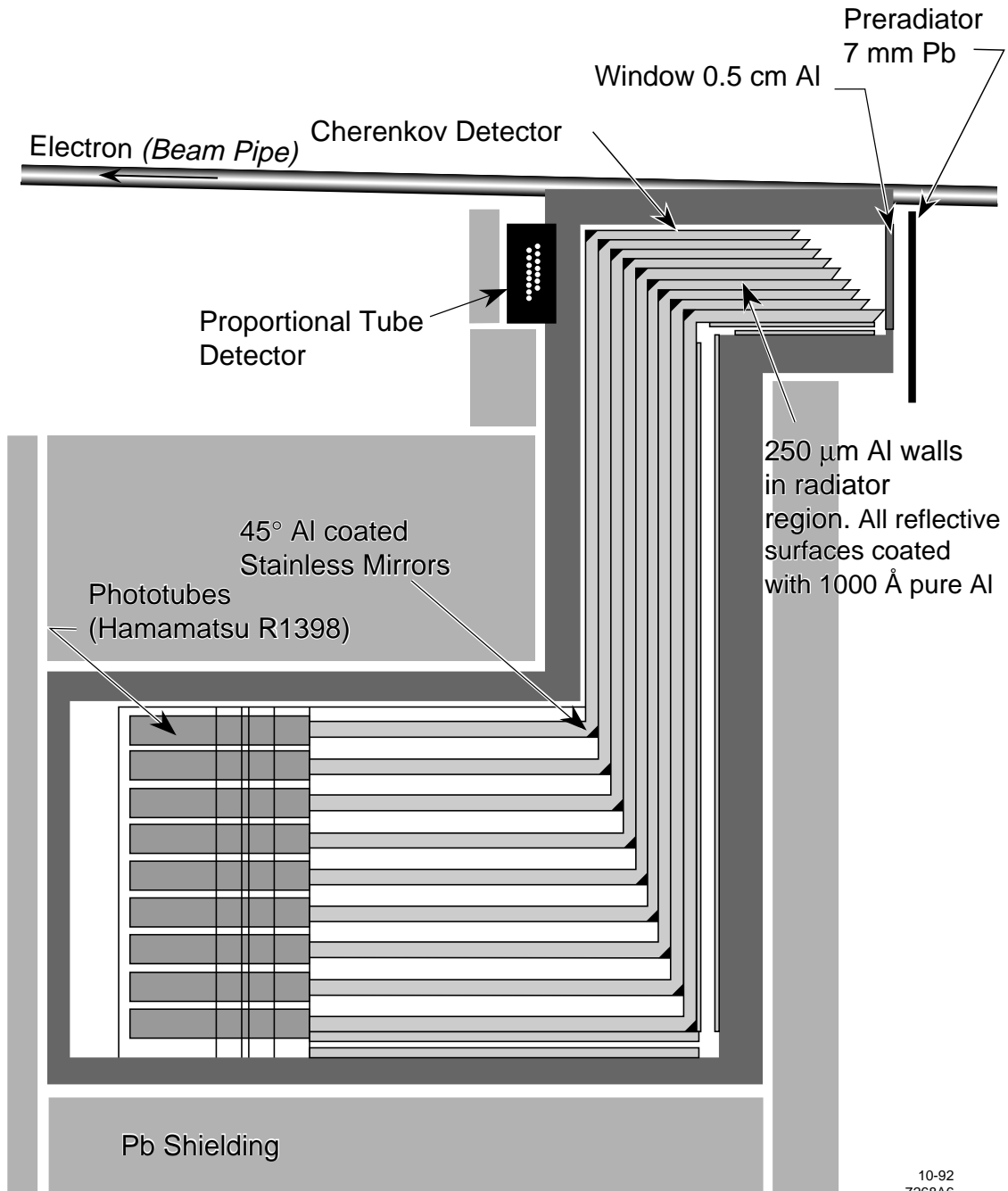
Figure 2-9: The layout of the multi-channel Cherenkov detector for the Compton Polarimeter is shown.

vanes away from the beamline and into the heavily shielded photomultiplier tubes. To boost the signal seen in the CKV, a 6.86 mm (1.2 χ_0) preradiator is placed immediately in front of the detector face, providing a signal amplification factor of ~ 4. The proportional tube detector seen immediately behind the CKV in Figure 2-9 was not used in the 1994-95 data taking, and has since been removed.

2.2.4   Compton Data Acquisition

The data acquisition for the Compton polarimeter is separate from the main SLD data acquisition system, and consists of a variety of modules housed in three Camac crates. These three crates are linked by a Kinetic Systems Serial Highway driver controlled by an M2ELN microVax minicomputer, allowing for a list-based readout at the beam rate of 120 Hz. This system is not triggered in any way, but rather takes data from all polarimeter channels on each and every SLC beam crossing. As the Compton laser is only running at 17 Hz, this provides six laser-off background measurements in each channel for every laser-on signal measurement. The microVax buffers the raw polarimeter data for a few seconds, and ships this raw data to the SLDACQ Vax where the online data analysis is performed and the data is eventually logged to tape. The helicity of each Compton laser pulse is determined according to a pseudo-random sequence so that CKV data from all four electron-photon helicity combinations can be recorded.

This system had been in place since 1992 and performed admirably until early December 1994, when the list readout function of the Kinetic Systems Serial Highway driver failed. Unable to repair or replace this somewhat obsolete piece of hardware, the polarimeter channels were pared down to the bare minimum necessary to perform the polarization measurement, and a standard Camac block transfer was employed for readout. This operation is significantly slower than the list-based readout around which the system was designed, and this crippled system could only keep up an acquisition rate of ≈ 30 Hz. With the Compton laser slowed down to

13 Hz, this allowed for only one laser off background measurement for each laser on pulse, although this is adequate for performing the polarization measurement. The Compton data was acquired in this fashion for the remainder of the 1994-95 SLD run. Before the start of the 1996 SLD run, this entire system was replaced by a Vax-based Camac controller which provides the same crate readout and buffering functions previously provided by the microVax system directly from the backplane of the SLDACQ computer.

2.3   SLD Detector

Originally proposed in 1984[23] and completed in 1991, the SLC Large Detector (SLD) is a general purpose solenoidal particle detector intended to be the main instrument for detecting Z boson decays at the SLC. The various SLD subsystems shown in Figure 2-10 provide simultaneous measurements of the charge, momentum, and energy of the observable particles created by the decay of Z bosons. The event triggering and physics reconstruction procedure will be described more fully in Chapter 4.

2.3.1   Data Acquisition

Monitoring and control of the SLD data acquisition, as well as other detector functions, is performed 'on-line' by various independent processes running on the SLD Vax cluster. The real work of the SLD data acquisition, however, is performed 'below-line' by an assortment of FASTBUS based processing modules which typically provide both event buffering and processing by means of embedded Motorola 68020 CPUs.[24] While the details of the data acquisition system vary somewhat for each SLD subsystem, in general the analog signals are conditioned and digitized by hybrid front end electronics modules mounted directly on the detector, and this data is then shipped serially over optical fiber links to the FASTBUS based pro-
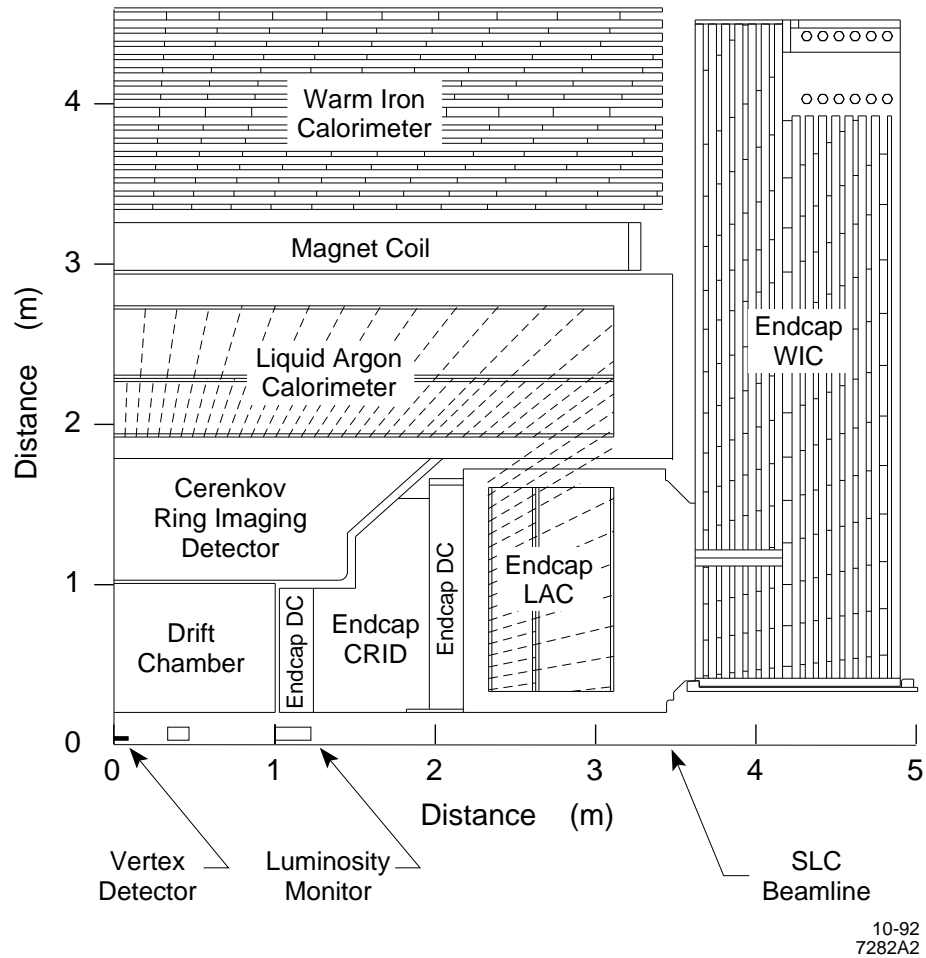
Figure 2-10: The SLD detector is shown in quadrant view with the IP at the lower left corner. The detector is designed to be both radially and longitudinally symmetric.

cessing modules. These FASTBUS modules apply various calibrations to the raw data, and then perform a wide variety of basic analysis tasks including waveform hit finding, rudimentary particle tracking, and the calculation of other useful quantities to provide information for the trigger decision. A trigger decision is made on every SLC beam crossing, and for all triggered interactions the data is collected from the various subsystems, packaged into an event, and written to a shared event pool on the SLDACQ Vax. At this stage, the various on-line processes can access this information to provide monitoring information and graphical one-event displays, and

from this pool the events are eventually written to tape.

The FASTBUS modules for the various subsystems generate and store their own calibration constants by injecting reference charges into the front end electronics modules to generate an observed channel response curve. This calibration procedure cannot be performed while the detector is taking data, but rather the detector subsystems are recalibrated on a roughly daily basis when the opportunity presents itself.

Since the beginning of the 1994-95 SLD run the below-line data acquisition system has been fully pipelined, allowing the various subsystems to acquire data in an autonomous fashion so that the faster subsystems and the trigger do not incur any appreciable dead-time from the slower wire chamber subsystems which can take many beam crossings to complete the processing of a triggered event.

2.3.2   Vertex Detector

At the heart of the SLD, wrapped immediately around the beampipe at the Interaction Point (IP), is the SLD silicon vertex detector (VXD).[25] Based on the same charged coupled device (CCD) technology found in modern video cameras, this instrument provides full three dimensional pixel-based measurements of the passage of ionizing (charged) particle tracks with an intrinsic ~ 5 micron resolution. Built out of 480 individual 9 mm by 13 mm CCD wafers with $(22 \ \mu\mathrm{m})^2$ pixel size, the VXD consists of 60 ladders arranged in four radial layers to provide position measurements from a radius of 3.0 cm to 4.2 cm from the incoming beam axis. Due to the somewhat convoluted geometry required by these small individual CCD elements, a typical track will hit two of the four radial layers providing an absolute resolution on the three dimensional track origin near the IP of 10 μm in the r-ϕ plane and 36 μm in the r-z plane. With an overall length of 20 cm, this detector provides nearly uniform coverage out to a production angle of $|\cos\theta| < 0.71$.

With a total of 120 Megapixels, it takes nearly 160 ms (19 beam crossings) to read
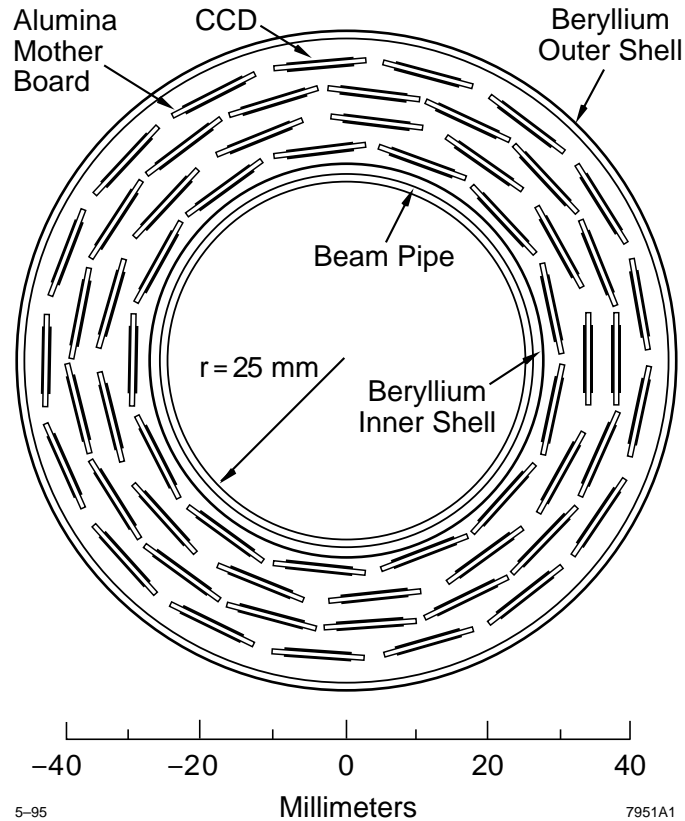
Figure 2-11: The radial layout of SLD Vertex Detector is shown. This device provides a three dimensional impact parameter resolution of ~ 10 microns.

all of the pixel data out of this device. Although CCDs are an unsuitable technology for higher rate machines, this readout time does not contribute any dead-time to the data acquisition system at the SLD, as the device is continuously integrating charge and being read out. With a typical trigger rate of 0.3 - 0.5 Hz, the random coincidence rate for hits from overlapping triggers is extremely low. Single pixel noise thresholds and a clustering algorithm are applied by the FASTBUS based readout electronics to reduce this data stream to a more manageable size of 50-80 kilobytes per triggered event.

2.3.3   Central Drift Chamber

Immediately surrounding the Vertex Detector is the Central Drift Chamber (CDC) which provides charge and momentum measurements for each of the charged tracks present in an event.[26] The CDC consists of a 2 m long by 1 m radius cylinder of gas which is instrumented with $\sim 35,000$ thin tungsten wires. A charged particle passing through the drift chamber will ionize the drift chamber gas along its path, depositing on the order of 5 keV/cm for a minimum ionizing track. The 150 μm field wires in the CDC, arranged as shown in Figure 2-12, have high voltage applied to create evenly spaced cells of parallel electric field. The electrons liberated in the ionization process drift with a uniform velocity of 8 microns/ns within the 0.9 kV/cm field of each cell towards a plane of instrumented 25 μm sense wires. Immediately on either side of the sense wires is a plane of guard wires which define the boundary of the drift cell. A voltage difference of 3 kV between the guard and sense wires provides some signal amplification as the individual electrons avalanche down onto the sense wires. The CDC gas is a mixture of 75% carbon dioxide, 21% Argon, 4% isobutane, and 0.3% water chosen to provide good ionization properties and drift velocity, while being resistant to electrical breakdown and charge diffusion.

The electrical pulse resulting from the charge deposited on both ends of each sense wire is sampled at 119 MHz and stored in a 512 channel switched capacitor array. A discriminated charge sum for each wire is also provided on every beam crossing to the FASTBUS based trigger logic algorithm. For triggered events, these waveforms are digitized by 12 bit Analog to Digital Converters (ADCs) and shipped to the FASTBUS based waveform analyzing processor (WASM). This processor calculates the time, charge, pulse height, and pulse width of the observed waveform which, when combined with the known drift time of the gas and detector geometry, allows a track position in space to be reconstructed. Double hits observed on a single wire can be resolved with reasonable efficiency down to a transverse track separation of 1 mm. The CDC data acquisition requires 80 ms (10 beam crossings) to fully
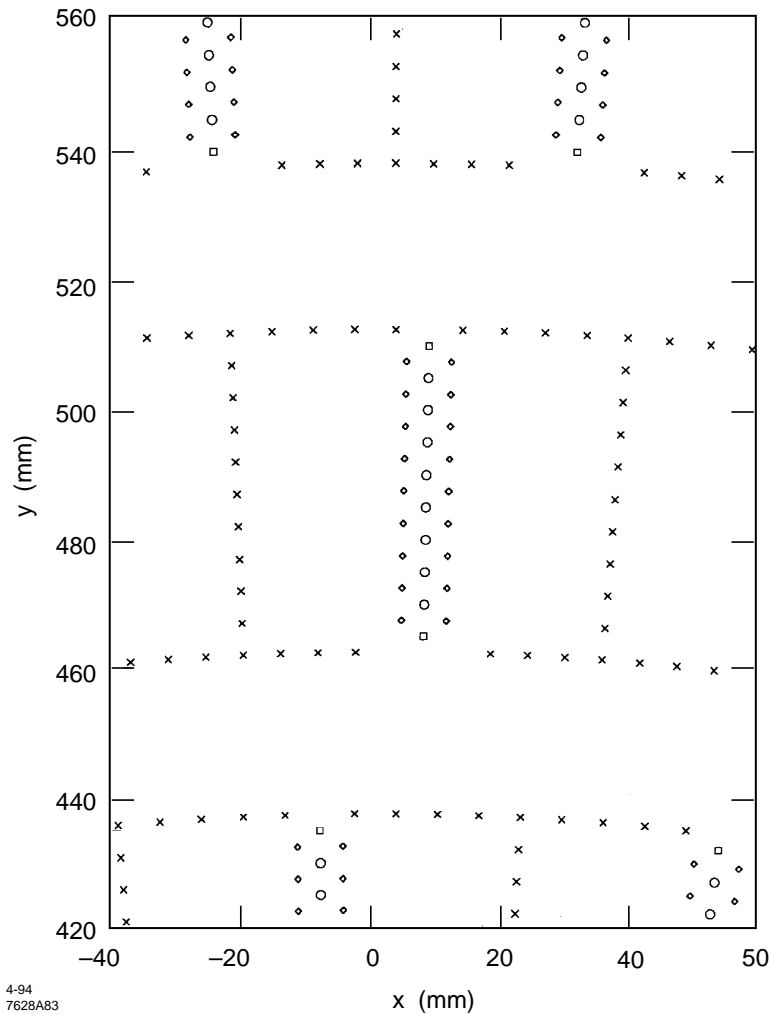
Figure 2-12: A closeup of a single drift cell in the CDC is shown. Voltage applied to the field wires (crosses) defines a nearly constant electric field running the length of the cell towards the guard wires (diamonds). Only the eight sense wires (circles) are instrumented for readout.

digitize, read out, and analyze the CDC waveforms. Due primarily to budgetary constraints, multiple CDC events cannot be buffered, and during this readout time the CDC electronics are insensitive to any new incoming data. A small number of complete waveform shapes are also preserved on each event to provide a check of the WASM algorithm.

Each CDC cell consists of eight sense wires sensitive to an volume of roughly 6 cm by 5 cm in cross section along the entire 2 m length of the chamber. The 640 cells are arranged in 10 radial superlayers to measure the curvature of a charged track, and hence its momentum, as it passes through the 0.6 Tesla solenoidal magnetic field provided by the SLD's 6.6 kAmp, 5.0 MWatt conventional magnetic coil. The transverse distance of a track from an individual sense wire is measured to an intrinsic resolution of approximately 70 microns in each cell, although uncertainties in the wire locations and changes in the drift velocity degrade this to an effective resolution of around 100 microns. While the longitudinal location of a track can be roughly estimated to a few centimeters by the amount of current produced at either end of the highly resistive tungsten wires, a more precise determination is made by combining the data from several layers which are slightly skewed with respect to the longitudinal axis of the chamber. There are six of these so called stereo layers, skewed by ± 41 milliradians with respect to the remaining axial layers. The relative inverse momentum resolution provided by the CDC alone has been measured to be $\sigma^2_{p^{-1}}/p^{-2} = (0.95\%)^2 + p^2(0.49\%/GeV)^2$, while the relative resolution of the combined CDC and VTX systems has been measured to be $\sigma^2_{p^{-1}}/p^{-2} = (0.95\%)^2 + p^2(0.26\%/GeV)^2$.[27]

The CDC can detect tracks with a uniform 96% efficiency with a momentum above 4 GeV/c, degrading only to 93% at 100 MeV/c. The geometry of the CDC provides uniform acceptance out to a production angle of $|\cos\theta| < 0.65$, and some tracks can be reconstructed out to a production angle of $|\cos\theta| < 0.87$. To extend the reach of the SLD tracking, two planar endcap drift chambers were installed at

either end of the CDC, although the analysis of the data from these chambers has proven to be difficult and will not be used in this analysis.

Drift chambers are somewhat sensitive devices in that excessive charge deposition can weaken and eventually break the fine sense wires. This would be a catastrophic failure in a chamber the size of the CDC, and some care is taken not to apply voltage to the chamber when SLC beam conditions are particularly bad. For this reason, the CDC was turned on for only 95% of the 1993-95 SLC running period.

2.3.4 Cherenkov Ring Imaging Detector

Particle identification is one of the most challenging experimental problems in any particle physics experiment. The high momentum tracks produced in Z boson decays are particularly ill suited to conventional techniques which measure the energy loss (dE/dx) or time of flight of an observed track in an attempt to identify the particle type through an estimate of its mass. Situated just outside of the CDC, the Cherenkov Ring Imaging Detector (CRID) identifies particles by observing the cone of Cherenkov light produced by the track as it traverses either a gas or liquid radiating medium.[28] The radius of this cone of Cherenkov light, or the absence of this cone altogether, as a function of track momentum provides the information necessary to identify various particle species.

In order to extend the useful momentum range of the device, two radiating materials are used. A liquid radiator composed of C_6F_{14} provides good $\pi/K/p$ particle identification in the momentum range from 0.5 to 3.0 GeV/c, while a gas radiator composed of C_5F_{12} covers the higher momentum range up to 35 GeV/c.[29] As shown in Figure 2-13, the Cherenkov photons from both radiators are detected in a time proportional chamber (TPC) which is little more than a really long drift chamber. Each TPC cell is filled with an ethane drift gas doped with a 0.1% concentration of the photoreactive substance tetrakis(dimethylamino)ethylene (TMAE), which provides good quantum efficiency for converting Cherenkov photons into elec-
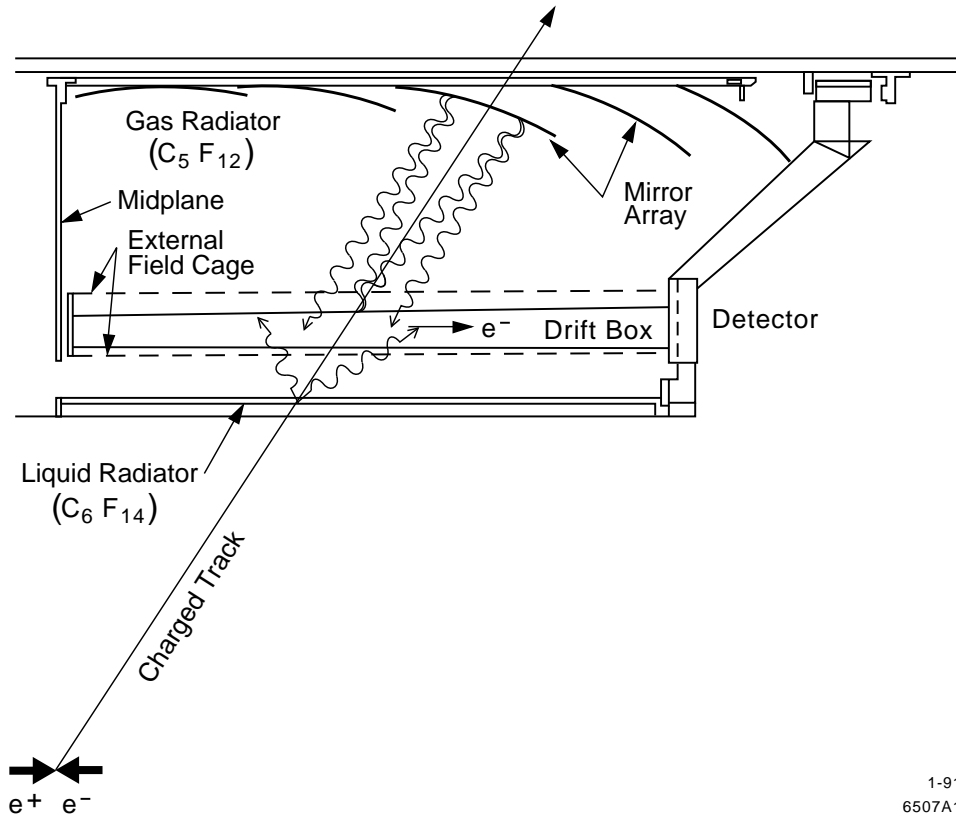
Figure 2-13: The geometry of a single CRID module is shown. Photoelectrons from both the liquid and gas radiator are detected on opposite sides of the same TPC.

trons. These electrons drift the length of the TPC and are detected by an array of 93 sense wires which are read out by identical electronics as those used in the CDC.

A typical track will have on the order of 10 detected photoelectrons from which to reconstruct a ring radius and make a particle identification, although the high quantum efficiency of the TMAE doped gas makes these chambers extremely sensitive to beam-related backgrounds. The possibility of high backgrounds breaking CRID sense wires is a constant concern during SLD operations, and while not catastrophic in the same sense that breaking a CDC wire would be, it does put that particular CRID module out of commission until it can be fixed. This was observed to happen a handful of times during the 1994-95 running period, and to protect the device it was typically turned off during periods of particularly bad backgrounds. For this

reason, CRID data is only available for 80% of all data taken with the drift chamber on. The CRID data has a comparable readout time as that of the CDC, and typically generates 200 k of data for hadronic Z events.

The barrel CRID has 40 modules arranged azimuthally around the CDC cylinder to provide complete particle ID coverage for the barrel region. Each module is divided into two independent longitudinal sections, each of which is read out independently at its outer end. The 1.2 meter long drift boxes provide particle ID coverage out to a production angle of $|\cos\theta| < 0.72$ which is well matched to the CDC tracking coverage.

The endcap CRID modules, sandwiched between the endcap drift chambers, were designed to extend the particle ID capabilities of the SLD into the forward region. Unfortunately, without a mature endcap tracking system these chambers are largely unusable, and will not be considered in this analysis.

2.3.5   Liquid Argon Calorimeter

The workhorse of the SLD detector is the Liquid Argon Calorimeter (LAC).[30] Located just inside the SLD coil from 1.8 m to 2.9 m of radius in the barrel, the LAC is a sampling calorimeter which provides an energy measurement of neutral and charged hadronic as well as electromagnetic particles over 98% of 4π in solid angle. A calorimeter works by putting enough radiating material in the way of an incoming particle to stop that particle through interactions and energy loss. In a sampling calorimeter, instrumented layers of some ionizing medium are interspersed with the radiator material to sample the energy deposited as a function of shower depth. The sum of this sampled energy is proportional to the total energy of the incident particle. The choice of liquid argon and lead was made to provide the most cost effective large area coverage with uniform energy response, good radiation resistance, and fine spatial segmentation.

The LAC is constructed in modules out of lead sheets and tiles as shown in
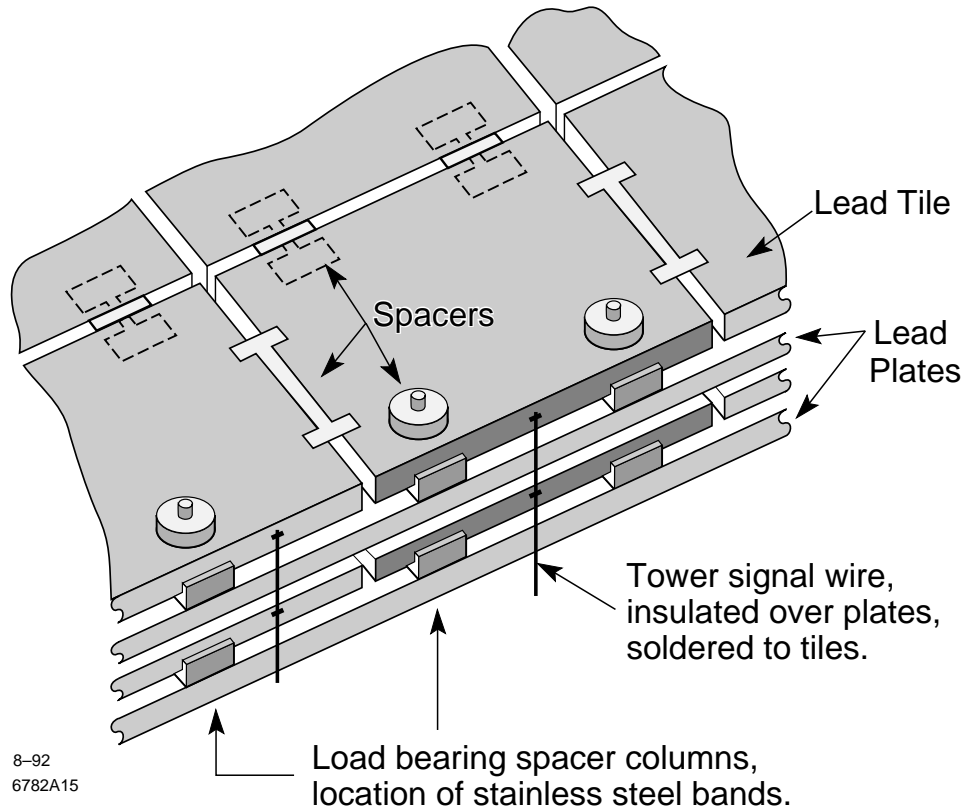
Figure 2-14: The arrangement of lead sheets and tiles which make up the LAC are shown. Voltage is applied to the lead sheets and signals are read out on the lead tiles. The geometry of the individual tiles defines the transverse segmentation of the LAC.

Figure 2-14, bathed in a common volume of liquid argon. The barrel LAC section and two endcap LAC sections are each housed in a separate cryostat containing a combined 35,000 liters of liquid argon. The innermost module consists of 56 lead plates, each 2 mm thick, spaced 2.75 mm apart to provide space for the liquid argon to fill the active layer. This electromagnetic (EM) section provides a total of 21 radiation lengths (21 χ_0) of material which will absorb 98% of the energy from a 50 GeV electron. High voltage applied between the lead sheets and tiles collects the ionization from the liquid argon onto the lead tiles which are electrically connected to form a single readout layer. In the EM section, the first 16 and remaining 40 planes are connected in this way to provide two longitudinal readout layers of 6 χ_0
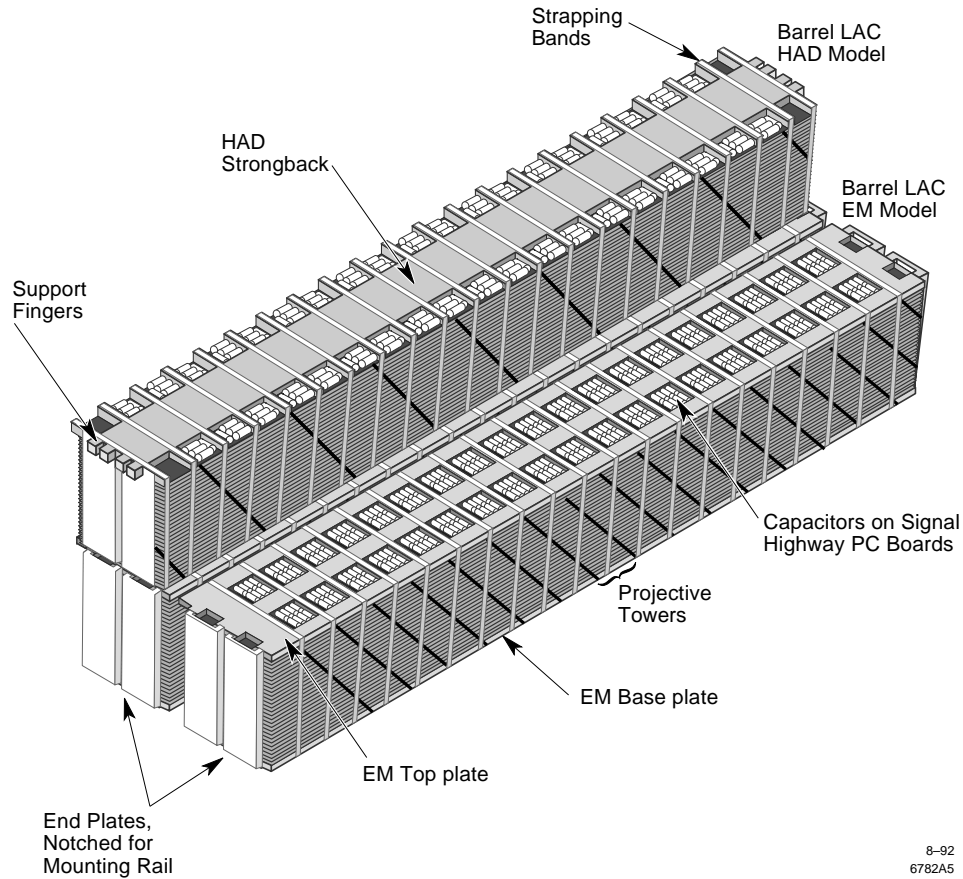
Figure 2-15: The geometry of a LAC module is shown. The longitudinal segmentation of the Lead-Argon sandwich is ganged together into four logical readout layers to reduce the total number of detector channels.

and 15 χ_0 respectively. The energy resolution of the EM section to either electrons or photons is measured to be $15\%/\sqrt{E(\text{GeV})}$.

The outer module consists of 26 lead plates, each 6mm thick, spaced 2.75 mm apart. This hadronic (HAD) section is evenly divided into two longitudinal readout layers of 1 absorption length (1 λ_0) each, which when combined with the EM section provides a total of 2.8 λ_0 of material. This calorimeter will contain around 90% of the energy from a hadronic shower providing a hadronic energy resolution of $65\%/\sqrt{E(\text{GeV})}$.

The spatial resolution of the LAC is determined by the segmentation of the

readout tiles, which are arranged in a roughly projective tower geometry. The 6 m long barrel LAC is divided into 96 polar and 192 azimuthal towers in the EM section with each EM tower subtending an angle of $\delta\phi = 33$ $(mRad)$ in azimuth and ranging from $\delta\theta = 36$ $(mRad)$ in polar angle at the center of the barrel to $\delta\theta = 21$ $(mRad)$ at the end of the barrel to maintain a constant projective area. The HAD towers match the projective geometry of the EM section, although more coarsely segmented by a factor of two in both the polar and azimuthal dimensions. The barrel LAC provides full coverage in production angle out to $|\cos\theta| < 0.84$, while the endcap LAC provides coverage in the forward region from $0.82 < |\cos\theta| < 0.99$. The endcap LAC modules are wedge shaped with a tower size adjusted with polar angle to keep the towers roughly square.

There are a total of 32,448 individual channels in the barrel LAC with an additional 8,640 channels in the endcap. Each channel is digitized after a dual gain charge sensitive preamplifier by a multiplexed 12 bit ADC to provide an effective 15 bit dynamic range. The digitized data, along with baseline information, is then shipped by serial fiber link to one of the 32 FASTBUS based Calorimetry Data Modules (CDMs) where the raw data is converted into a single measured energy per channel. Energy sums are also calculated by detector region and readout layer to be used in the trigger decision. The entire LAC can be read out and analyzed in ~ 4 ms providing a nearly dead-time free acquisition system.

2.3.6 Warm Iron Calorimeter

Outside of the magnetic coil is the Warm Iron Calorimeter (WIC).[31] The massive WIC structure provides muon tracking with 18 layers of Iarrochi tubes sandwiched between the 1 inch plates of WIC steel, some amount of additional calorimetry information, as well as a flux return path for the solenoidal magnetic field. The Iarrochi tubes used are small 1 cm square plastic wire chambers operated in limited streamer mode with a single wire running the length of the 6.8 m barrel modules.

The wires themselves are not instrumented, but rather capacitive strips and pads immediately outside the Iarrochi tubes detect the current streamers produced by muons passing through the tubes. In the barrel, there are 14 layers of longitudinal strips parallel to the beam axis, and 4 layers of transverse strips used to track muons as they pass through the WIC steel. The endcap modules have a similar thickness with half of the tubes running vertically and the other half running horizontally. The WIC strips are a binary system, with each strip being discriminated to provide a true or false hit record on every beam crossing.

The barrel chambers provide an overall efficiency of 85% for detecting penetrating muons (above about 2.5 GeV) out to a production angle of $|\cos\theta| < 0.6$. Due to constraints imposed by strict earthquake standards at SLAC, there is something of a hole in the WIC coverage before the endcap module becomes useful between $0.74 < |\cos\theta| < 0.95$. For this reason, muon identification in this region must rely upon LAC shower information only, with a corresponding loss in efficiency.

The WIC pads were designed to be an extension of the calorimetry system, providing information on the tails of hadronic showers which have leaked from the LAC. This information has not been used in this analysis, however.

2.3.7   Luminosity Monitor

The SLD luminosity monitor (LUM) is a pair of compact, finely segmented silicon-tungsten calorimeters installed immediately around the beampipe on either side of the SLD IP.[32] The LUM is used to identify low-angle Bhabha scattering between 23 mr and 68 mr in polar angle, which is dominated by the well understood electromagnetic process of t-channel photon exchange. The LUM is triggered and read out at 120 Hz as part of the LAC data acquisition to provide a nearly dead-time free count of the number of low-angle bhabha events which can then be used to estimate the total luminosity delivered by the SLC. As the SLD data does not have the statistics necessary to make competitive measurements of absolute cross sections,

this luminosity information is used more as a diagnostic tool than as an input to physics results.

2.3.8 Detector Simulation

Due to the complexity of modern particle physics detectors, it has become common practice to generate simulated data, generally referred to as *Monte Carlo*, to aid in the understanding of a variety of instrumental and systematic effects. The process of generating Monte Carlo data is typically divided into three distinct phases.

The first step, known as the generation phase, involves simulating some real physical process by generating momentum four vectors representing the produced particles from a set of theoretical cross sections. A number of packages are available to simulate the most common physics processes at the Z pole. The most heavily used in this analysis is the KORALZ tau pair generator which simulates both the production and decay of tau pairs using the TAUOLA decay simulation package.[33, 34] Limitations of the KORALZ generator for simulating tau production in the presence of the anomalous dipole couplings will be discussed in Chapter 5.

The second step, known as the simulation phase, involves tracking these produced particles through a model of the SLD detector and simulating the interactions between these particles and the various detector components. Most of the work of the simulation phase is performed by the widely used GEANT detector simulation package.[35] For any simulated particle traversing an instrumented region of the detector, simulated raw data is generated at the individual hit level to match as closely as possible what would be observed in the real detector.

In the third step, known as the reconstruction phase, the simulated detector hits are overlayed with real detector noise sampled from a set of random detector triggers to produce simulated events. One random trigger is taken every 20 seconds during normal SLD data logging and provides a snapshot of the typical beam-related background present in the detector. These simulated events are then run

through the full SLD reconstruction package so that a direct comparison can be made between the reconstructed or 'observed' quantities and the generated or 'true' values produced by the event generator.

As will be seen, the SLD Monte Carlo provides a crucial tool for understanding the sensitivity and accuracy of this analysis.

Chapter 3

Compton Polarimetry

The single most important attribute of the SLC program is the ability to accelerate polarized electrons. Consequently, the accurate measurement of this electron beam polarization is of fundamental importance to almost every physics analysis performed by the SLD collaboration. The Compton polarimeter system has evolved considerably since its conception in 1985, and currently represents the most accurate high energy electron polarimeter in the world. This chapter will describe how this polarization measurement is performed, and the techniques used to continually calibrate and monitor the polarimeter over the course of many months of SLD data taking. This chapter explicitly describes the polarization analysis applied to the 1994-95 SLD run, and further details can be found in[36, 37]. The 1993 analysis has been described previously.[38, 39]

3.1 Compton Scattering

The elastic scattering of photons from electrons is a well understood QED process known as Compton scattering. The tree-level polarized differential Compton cross

section can be written in the electron rest frame as [40]

$$\frac{d^2\sigma}{d\Omega} = \frac{r_0^2}{2}\left(\frac{k'}{k}\right)\left[\frac{(k-k')^2}{kk'} + (1+\cos^2\theta_0)\right]\{1 - \mathcal{P}_\gamma\mathcal{P}_e A_{e\gamma}(\mathbf{k},\mathbf{k}')\} \qquad (3.1)$$

where $r_0 = 2.82$ fm is the classical electron radius, k and k' are the momenta of the incoming and outgoing photons, θ_0 is the photon scattering angle, $\mathcal{P}_\gamma$ is the circular polarization of the incident photon, and $\mathcal{P}_e$ is the polarization of the incident electron. The asymmetry function $A_{e\gamma}(\mathbf{k},\mathbf{k}')$ is then given by

$$A_{e\gamma}(\mathbf{k},\mathbf{k}') = \frac{\left(\frac{1}{k'} - \frac{1}{k}\right)\left[\mathbf{k}\cos\theta_0 + \mathbf{k}'\right]\cdot\boldsymbol{\sigma}}{\frac{(k-k')^2}{kk'} + (1+\cos^2\theta_0)}, \qquad (3.2)$$

where $\boldsymbol{\sigma}$ is the spin vector of the electron.

In order to write this cross section in terms of lab frame variables, it is useful to define two kinematic variables (x, y) in terms of the incident and scattered electron (E, E') and photon (K, K') energies as

$$y \equiv \left[1 + \frac{4KE}{m_e^2}\right]^{-1} = \frac{E'_{min}}{E} \qquad (3.3)$$

$$x \equiv \left[1 + y\left(\frac{E\theta_K}{m_e}\right)^2\right]^{-1} = \frac{K'}{K'_{max}}, \qquad (3.4)$$

where θ_K is the photon emission angle in the lab frame. At the SLC, a $K = 2.330$ eV photon is collided with an $E = 45.64$ GeV electron resulting in a kinematic limit $(x = 1)$ of

$$E'_{min} = y\, E = (0.3804)(45.64\text{ GeV}) = 17.36\text{ GeV} \qquad (3.5)$$

$$K'_{max} = (1-y)\, E = 28.28\text{ GeV}, \qquad (3.6)$$

which represents a complete backscatter $(\theta_0 = \pi)$ in the electron rest frame.

After a change of variables to the lab frame, Equation 3.1 can be written as[41]

$$\frac{d^2\sigma}{dxd\phi} = \left.\frac{d^2\sigma}{dxd\phi}\right|_{unpol} \{1 - \mathcal{P}_\gamma[\mathcal{P}_e^z A_{e\gamma}^z(x) + \mathcal{P}_e^t A_{e\gamma}^t(x)\cos\phi]\}, \qquad (3.7)$$

where ϕ is the azimuthal angle of the scattered photon with respect to the transverse electron polarization vector, $\mathcal{P}_\gamma$ is again the circular polarization of the incident photon, and now the electron polarization has been decomposed into a longitudinal component ($\mathcal{P}_e^z$) and a transverse component ($\mathcal{P}_e^t$). The unpolarized cross section in the lab frame can be written in terms of the kinematic variables as

$$\left.\frac{d^2\sigma}{dxd\phi}\right|_{unpol} = r_0^2 y \left\{ \frac{x^2(1-y)^2}{1-x(1-y)} + 1 + \left[\frac{1-x(1+y)}{1-x(1-y)}\right]^2 \right\}, \qquad (3.8)$$

while the asymmetry functions are given by

$$A_{e\gamma}^z(x) = r_0^2 y[1-x(1+y)]\left\{1 - \frac{1}{[1-x(1-y)]^2}\right\} \cdot \left.\frac{d^2\sigma}{dxd\phi}\right|_{unpol}^{-1} \qquad (3.9)$$

$$A_{e\gamma}^t(x) = r_0^2 xy(1-y)\frac{\sqrt{4xy(1-x)}}{1-x(1-y)} \cdot \left.\frac{d^2\sigma}{dxd\phi}\right|_{unpol}^{-1}. \qquad (3.10)$$

These functions are shown in terms of the kinematic variable x in Figure 3-1.

The first order radiative corrections to polarized Compton scattering have been calculated at a variety of collision energies.[42] These results have been extrapolated to the SLC beam energy and the inclusion of the higher order terms are found to modify the asymmetry function by less than 0.1%.[43]

The longitudinal Compton asymmetry function $A_{e\gamma}^z$ has a number of nice features from an experimental point of view. The kinematic limit at $x = 1$ provides a sharp Compton edge beyond which no scattered electrons will be produced. This proves to be an invaluable calibration tool, as the CKV detector position can be measured to a precision of $\approx 100\mu$m by measuring the signal drop in the outer channels while the detector is moved transversely from its nominal position. Calibrating the detector
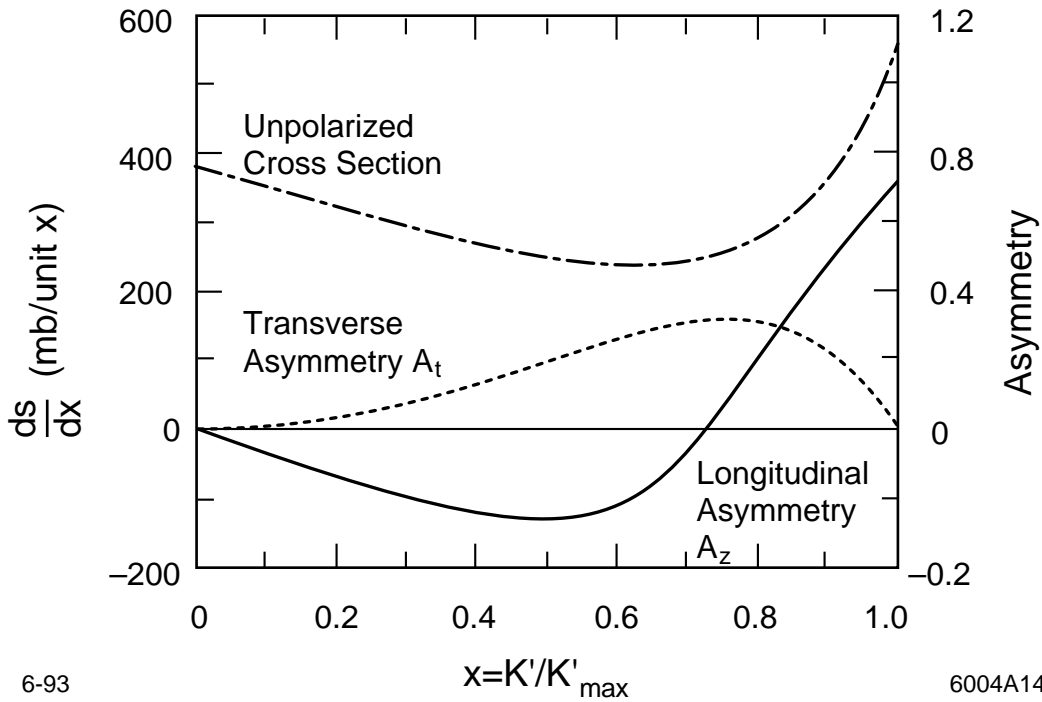
Figure 3-1: The unpolarized cross section and asymmetry functions in polarized Compton scattering are shown as a function of the kinematic variable x.

with this *table scan* technique will be described in more detail in Section 3.5. Another nice feature comes from the relatively large asymmetry seen in Compton scattering. The asymmetry at the Compton kinematic endpoint is given by

$$A_{e\gamma}^z(1) = \frac{1-y^2}{1+y^2} \tag{3.11}$$

which gives an endpoint asymmetry of 74.7% at the SLC. This is much larger than the $\approx 5\%$ asymmetry typically seen in polarized Møller scattering for instance, and provides a statistically precise measurement in a relatively short amount of time.

The Compton polarimeter is designed to measure the longitudinal polarization of the electron beam only. The CKV detector has a uniform acceptance in the azimuthal scattering angle ϕ, and all transverse polarization information is lost. A device that could measure the transverse electron polarization has been built

and is currently being commissioned. It consists of a finely segmented Quartz fiber calorimeter sitting in the neutral beamline to detect the backscattered photons from the Compton process. A transversely polarized electron beam would produce a shift of 25 microns in the centroid of the scattered photons as the incident laser polarization is reversed. Measuring this small displacement in the high background environment of the SLC final focus is challenging at best, and work on commissioning this detector continues.

3.2   Polarization Calculation

The Compton asymmetry in each CKV detector channel A_C^i is defined to be the asymmetry in the scattering cross section when the electrons and photons collide with their polarization vectors aligned forming a $J_z = 3/2$ spin state, and collisions with their polarization vectors opposed forming a $J_z = 1/2$ spin state. This asymmetry can be written as

$$A_C^i \equiv \frac{\sigma^i(J_z = 3/2) - \sigma^i(J_z = 1/2)}{\sigma^i(J_z = 3/2) + \sigma^i(J_z = 1/2)}$$
$$= |\mathcal{P}_e||\mathcal{P}_\gamma|a^i \tag{3.12}$$

where it is understood that $\mathcal{P}_e$ denotes the longitudinal electron polarization, and a^i is the analyzing power of each CKV channel which is given by

$$a^i = \frac{\int \frac{d\sigma}{dx}\big|_{\text{unpol}} A_{e\gamma}^z(x)\mathcal{R}^i(x)dx}{\int \frac{d\sigma}{dx}\big|_{\text{unpol}} \mathcal{R}^i(x)dx}. \tag{3.13}$$

This analyzing power a^i is the cross section weighted asymmetry integrated across the response function $\mathcal{R}^i(x)$ for the particular channel, normalized to the total channel response.

From Equation 3.12, the measurement of the electron polarization requires three
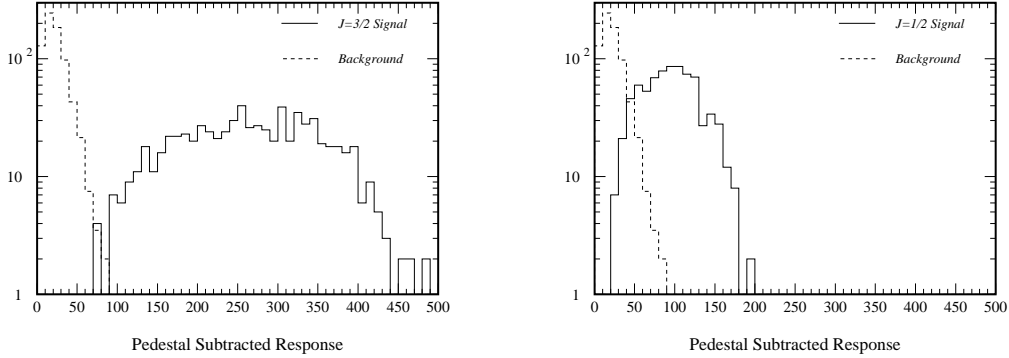
Figure 3-2: Raw data from the CKV channel 7 is shown for the $J_z = 3/2$ and $J_z = 1/2$ helicity configurations. The common laser off background is also shown. Channel 7 contains the kinematic endpoint and thus displays the largest raw asymmetry.

components:

- The raw asymmetry A_C^i measured in a particular CKV detector channel;

- The channel response function $\mathcal{R}^i(x)$, determined by a calibration procedure;

- The circular polarization $\mathcal{P}_\gamma$ of the incident laser beam.

The remainder of this chapter will describe in detail the process of determining these three quantities as well as the systematic uncertainty associated with each. Since the Compton polarimeter can make a polarization measurement to a statistical precision of $\delta\mathcal{P}_e/\mathcal{P}_e \sim 1\%$ in about three minutes, the uncertainty in the electron beam polarization measurement is entirely dominated by these systematic errors.

3.3 Experimental Asymmetry

Experimentally, the Compton asymmetry in channel i is formed from the mean channel responses $\langle N \rangle$ measured separately for the four possible electron-photon helicity combinations. The two spin aligned configurations are combined to give the

mean channel response in the $J_z = 3/2$ state $\langle N \rangle_{3/2}^i$, while the two spin opposed configurations are similarly combined to provide $\langle N \rangle_{1/2}^i$. As shown in Figure 3-1, the $J_z = 3/2$ cross section is larger at the kinematic endpoint than the $J_z = 1/2$ cross section, resulting in a positive asymmetry. Since the Compton system acquires data at the SLC beam rate of 120 Hz, while the Compton laser only fires at 17 Hz, the mean channel response is also measured in the intervening six beam crossings when the laser does not fire. This laser off channel response $\langle N \rangle_{off}^i$ measures the sometimes substantial background present in each CKV channel due to the passage of the outgoing SLC electron bunch. The resulting measured asymmetry

$$A_m^i = \frac{\langle N \rangle_{3/2}^i - \langle N \rangle_{1/2}^i}{\langle N \rangle_{3/2}^i + \langle N \rangle_{1/2}^i - 2\langle N \rangle_{off}^i} \tag{3.14}$$

is then equal to the compton asymmetry A_C^i aside from small corrections which are applied to account for electronics noise and detector linearity issues as discussed in Section 3.7.

3.4   Polarimeter Operations

Not every beam pulse observed by the Compton system goes into calculating the mean channel responses used in Equation 3.14, but rather an attempt is made to remove any beam crossings which would clearly not produce Z bosons at the SLD. This includes the obvious case of when the SLC is not delivering beam at all, but also includes various garbage pulses which are usually far off the Z pole energy and could bias the beam polarization measurement. The five online vetoes which are applied to the data have the following selection criteria:

- *Electron Toroid:* The current measured in the inbound North Final Focus beam toroid must be above a threshold selected to ensure that nearly the full beam current is being delivered;

- *Positron Toroid:* The equivalent current measured in the South Final Focus beam toroid must also be above a threshold;

- *CKV Channel 9:* The signal seen in this channel, which is well beyond the Compton kinematic endpoint, must be below 1000 ADC counts to reject pulses saturated with beam noise;

- *Electron Dumper:* The electron dumper module must not have fired, signaling SLC's intention to dump the beams at the end of the linac;

- *Beam Deflection Scan:* The final focus beam optics must be set for collisions at the SLD, rather than scanning the beams across each other.

Only those beam crossings which pass these five requirements are used in the polarization measurement.

To reduce the amount of data written to tape by the polarimeter, as well as to aid the offline calculation of the observed Compton asymmetry, the channel response sums, squared channel response sums, and total number of non-vetoed beam crossings are accumulated separately for each electron-photon helicity state over the course of a polarimeter run. This data is then written to tape as a *summary data bank*, along with a variety of monitoring information reflecting the current operating conditions of the polarimeter, and it is from this data that the measured asymmetries are calculated offline. In order to allow for a re-processing of the data offline, the raw data from all of the laser on beam crossings and one of the intervening six laser off pulses are also written to tape as a *raw data bank*.

Each polarimeter run nominally covers 20,000 SLC beam crossings, although a run will be stopped early if the electron beam disappears for an extended period of time. This run length was chosen so that the statistical error of any single run is comparable to the overall systematic accuracy to which the system can be calibrated. Each polarimeter run is then treated as an independent measurement of the electron beam polarization at that particular moment in time.

In order to achieve a systematically precise measurement, approximately two out of every three polarimeter runs takes data with some attribute of the system set outside of its nominal operating range. One example is taking data with the CKV detector moved transversely from its normal operating position to calibrate the detector location. Another example is varying the Compton laser Pockels cell voltages which allows a measurement of the laser polarization to be performed. These calibration runs are automatically interspersed with the nominal polarization measurements by a list-based scheduling algorithm in the Compton data acquisition software. Each calibration cycle is completed in about three hours of data taking, providing many independent calibration measurements each day with only minimal manual intervention. The data from these off-nominal calibration runs are removed in the offline polarimeter analysis, and are not used to directly measure the electron polarization. As a result, a good beam polarization measurement is recorded by the system approximately every 10 minutes, which is more than adequate to track the slow drifts in the electron beam polarization observed at the SLC. Primarily due to changes in the electron beam orbit through the North SLC arc, these drifts tend to have a time scale on the order of hours rather than minutes.

3.5   Cherenkov Detector Calibration

As shown in Equation 3.13, the analyzing power of a particular CKV detector channel depends upon three functions. The unpolarized cross section $\frac{d\sigma}{dx}\big|_{\text{unpol}}$ and the Compton asymmetry function $A_{e\gamma}^{z}(x)$ are both well known theoretical functions listed in Section 3.1. The channel response function $\mathcal{R}^{i}(x)$, however, must be determined for each CKV channel in order to calibrate the detector. The acceptance of a given detector channel as a function of scattered energy is primarily a function of two free parameters:
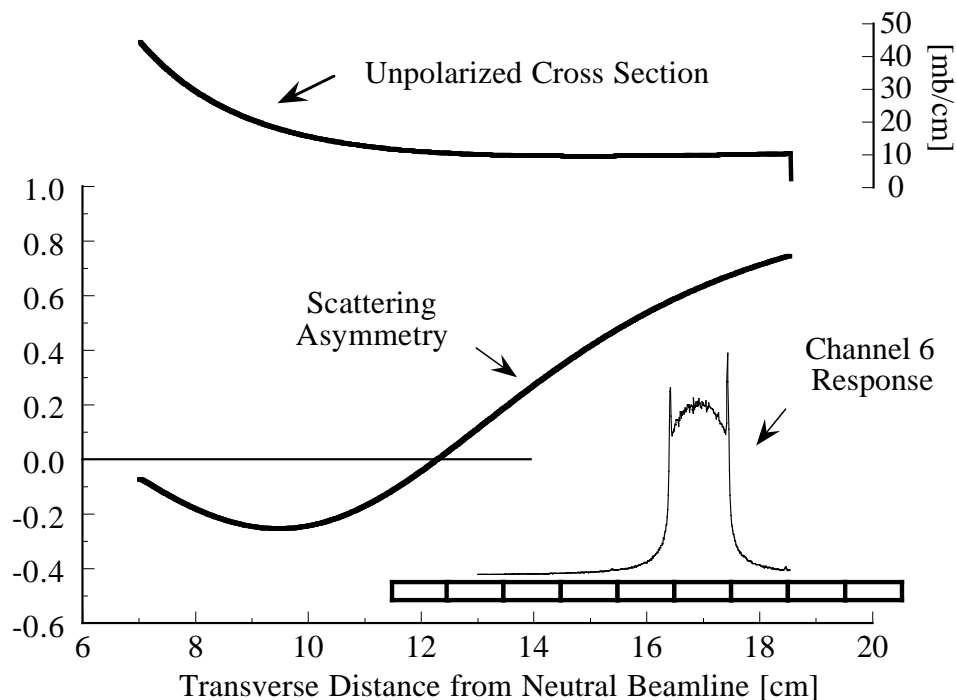
Figure 3-3: The three functions needed to calculate the analyzing powers are shown as a function of transverse distance from the neutral beam line. A scale representing the nine CKV detector channels is also shown.

- The energy to position mapping determined by the combination of dipole and quadrupole magnetic fields in the analyzing spectrometer magnets;

- The location of the detector with respect to the neutral (undeflected) beam axis.

The magnetic quadrupole field, not a tremendously advantageous feature in spectrometer design, was added before the beginning of the 1994-95 SLD run as part of an SLC Final Focus upgrade. Although this field makes the functional form of the energy to position mapping much more complex with respect to a purely dipole field, it does not in any way change the overall function of the spectrometer in the polarization analysis.

To first order, the projective CKV detector channels provide a uniform acceptance over the transverse width of each detector channel. This idealized detector

response must be modified, however, to account for the real life smearing of the detector response which is exacerbated by the presence of a 1.2 χ_0 lead preradiator immediately in front of the detector. The true detector response function is estimated with a Monte Carlo simulation of high energy electrons incident on the CKV detector. Based on the EGS4 electromagnetic shower simulation package,[44] this model includes a complete simulation of the electron transport into the detector, a detailed description of the CKV detector geometry, as well as a full simulation of the Cherenkov light transport through the detector to the photomultiplier tubes. A description of this detector simulation can be found in Appendix B. The inclusion of the complete detector response functions modifies the derived analyzing powers by only $\sim 1\%$, although this is significant when compared to the few tenths of a percent accuracy to which the analyzing powers are calibrated.

Table Scan

The CKV detector is accurately calibrated at one point in time by taking a special set of polarimeter runs called a *table scan*. A typical table scan consists of consecutive polarimeter runs taken while stepping the detector position transversely from its nominal position with respect to the neutral beamline. Data is recorded at 16 scan points with detector translations spanning the range from 0 to 2.5 cm. With 7 channels observing the backscattered electrons at 16 positions, there are 112 independent measurements of both the total cross section and the Compton asymmetry function at various spatial locations. This combined data set is fit using input from the EGS4-generated response functions to simultaneously determine 1 relative detector position, 1 free spectrometer parameter, 1 polarization product $(\mathcal{P}_e \mathcal{P}_\gamma)$, 6 relative channel gains, and 16 overall luminosity normalizations. The detector position measured is the relative position of the kinematic endpoint with respect to the CKV channel walls, while the one free spectrometer parameter used is the relative transverse location of the quadrupole element in the spectrometer bending

field. Since a quadrupole field increases linearly with transverse distance, shifting this field has the effect of changing the total dipole strength seen by the scattered electrons.

Although all of the data is used in the table scan fit, the detector position is primarily determined by the drop in total signal seen in CKV channels 6 and 7 as the kinematic endpoint sweeps through, while the spectrometer strength is primarily determined from the shape of the asymmetry observed across all of the CKV detector channels. Typical data from a table scan are shown in Figure 3-4. Once the detector position and spectrometer strengths are known, the integral in Equation 3.13 can be performed to generate a set of calibrated analyzing powers for the detector.

Table scans were performed approximately twice a week during the 1994-95 SLD run, with each scan determining the relative detector position to $\approx 100\mu$m, which corresponds to a statistical determination of the analyzing power of $\simeq 0.1\%$. The typical $\chi^2/d.o.f.$ for each table scan fit is between 1.5 and 2.0, indicating that the systematic uncertainties are comparable to the statistical precision.

Analyzing Power Tracking

While each table scan provides a precise analyzing power determination at one point in time, some effort must be made to monitor this calibration during the interval between scans. The most likely cause of a calibration shift is a real displacement of the outgoing electron bunch trajectory with respect to the CKV detector and the Q6.5 axis. The presence of this quadrupole field amplifies any displacement of the on-energy beam, so that a 100 μm shift in the outgoing electron trajectory will result in a 310 μm shift in the kinematic endpoint. As the relative analyzing power will change by roughly 1%/mm in the inner channels (1-6), and around 0.5%/mm in channel 7 (which contains the kinematic endpoint), even very small beam motion can have an observable effect on the polarization measurement.

To track the CKV detector calibration over time, two asymmetry ratios A_C^4/A_C^7
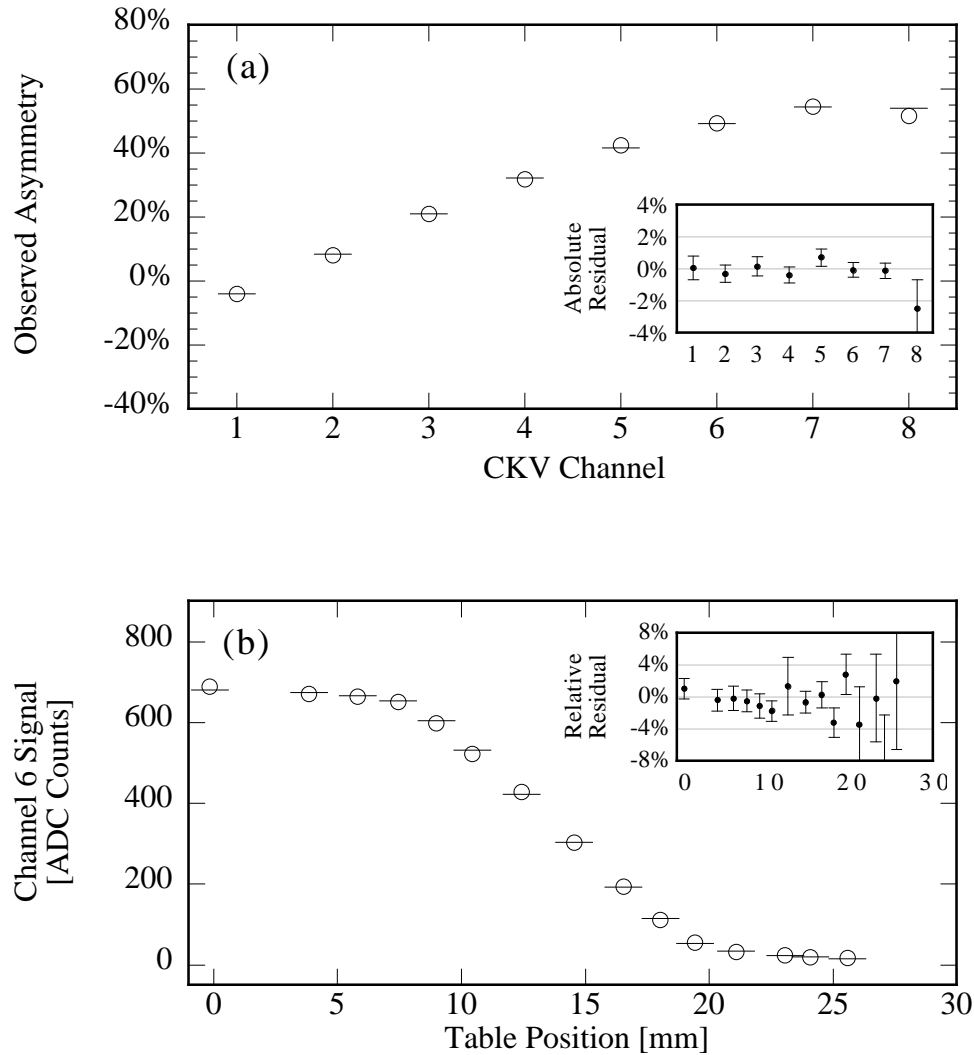
Figure 3-4: Results from a single table scan fit are shown. Figure 3-4a shows the observed asymmetry in each detector channel at the nominal table position, while Figure 3-4b shows the Channel 6 response as a function of table position. Also plotted are the residuals from the table scan fit results, where the errors are statistical only. This is only a small amount of the total data available in this table scan as there are asymmetry curves from 15 table positions and channel responses from 7 CKV channels which are all fit simultaneously.
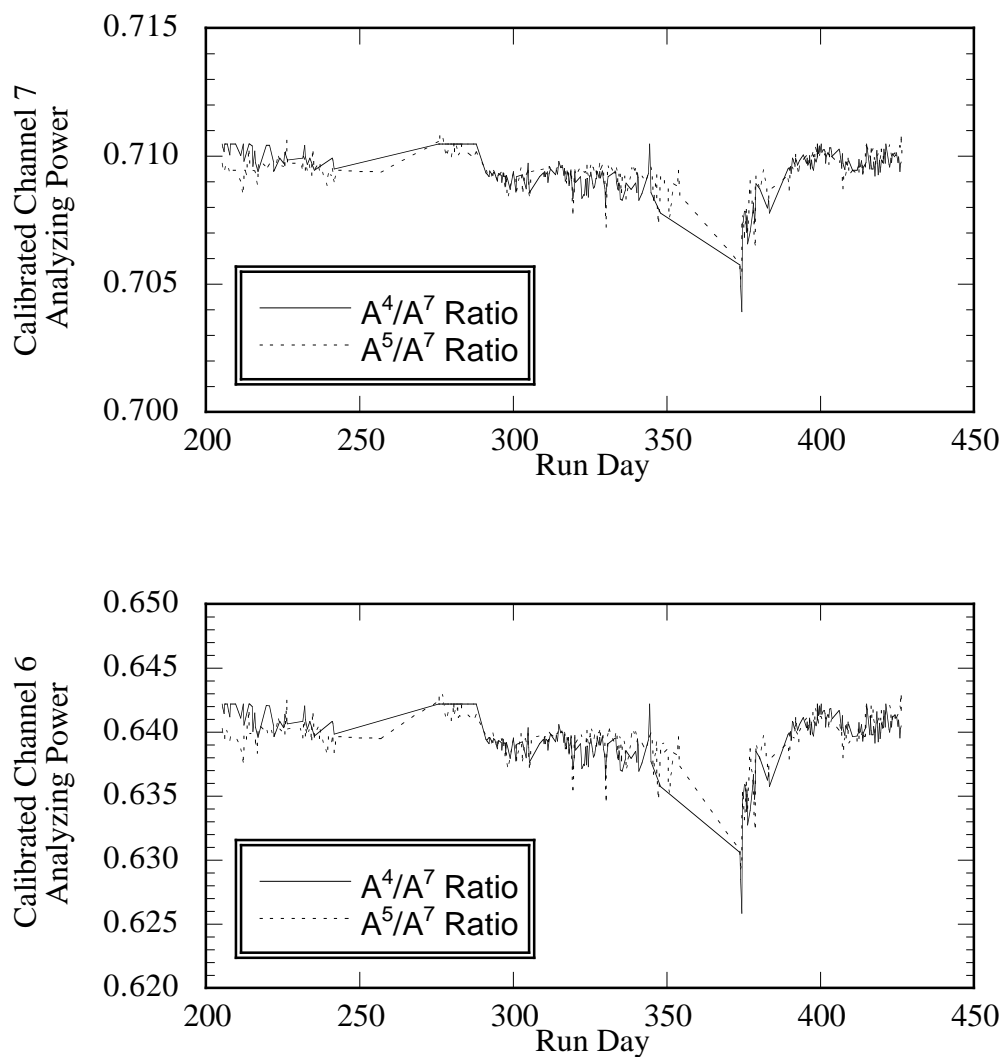
Figure 3-5: The CKV channel 6 and 7 analyzing powers are shown as a function of time as determined by interpolating between the table scan calibrations. The solid curve shows the analyzing powers as determined by the A_C^4/A_C^7 ratio, while the dashed line results from using the A_C^5/A_C^7 ratio.

and A_C^5/A_C^7 are considered. Because the Compton asymmetry function has a non-zero curvature, especially near the kinematic endpoint, each of these two ratios will change as the Compton spectrum is shifted with respect to the detector channels providing two redundant monitors of the detector calibration. The dependence of the analyzing powers on these asymmetry ratios can be empirically measured by considering data taken close in time (within 3 hours) of a table scan, and the observed dependence agrees well with the theoretical expectation predicted by the EGS4 detector model. The relative change in the asymmetry ratio observed is roughly a factor of 2 larger than the relative change in the analyzing power, providing ample statistical power to track the detector calibration over time. Using this technique, the analyzing powers for channels 5 through 7 are interpolated between the table scan points to provide a continuous time-dependent detector calibration for the entire 1994-95 SLD run. The difference in the interpolated analyzing powers found using the two asymmetry ratios is less than 0.1%.

Calibration Systematics

The primary systematic uncertainty in the calibration process arises from the accuracy of the EGS4 generated response functions. Without direct test beam data, the best way to test the accuracy of these response functions is through the table scans themselves. A number of ad-hoc parameterized response functions were used in the table scan fits, such that the response function was actually fit to the data itself. In addition, fits were performed to the EGS4 generated response functions with an additional scaling factor applied to the tails. The goodness of fit achieved by modifying the response functions in this way was never significantly improved, and the variation of 0.20% observed in the derived channel 7 analyzing power is taken as an estimate of the systematic uncertainty.

The radiative corrections to the tree level Compton scattering cross section have not been applied in this analysis. The expected relative change in the asymmetry
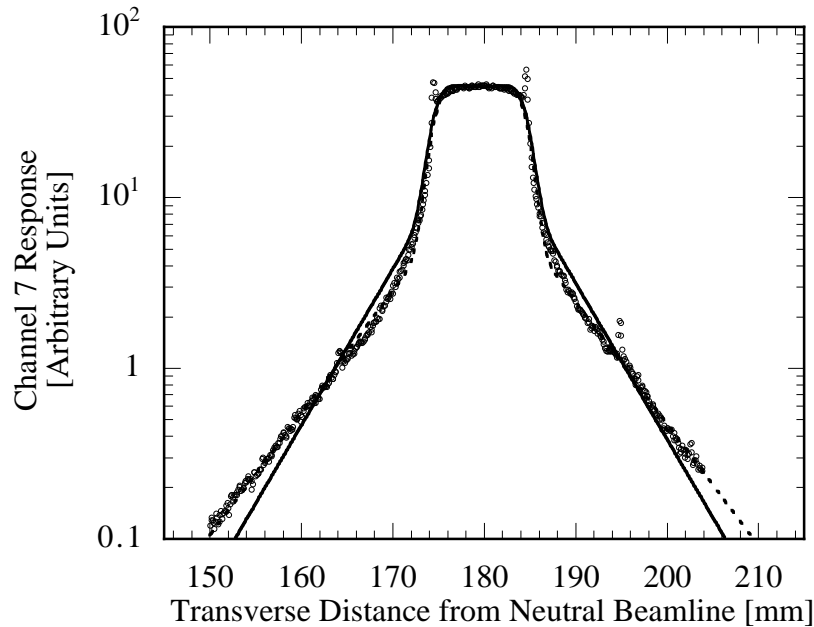
Figure 3-6: The EGS4 derived Channel 7 response function (circles) is shown along with the best ad-hoc response function (solid line) fit directly to the table scan data. The dashed curve shows this same ad-hoc function fit to the EGS4 data directly.

function is less than 0.1% near the endpoint, and is being assumed as a systematic error.

The question of whether low asymmetry signal is being rescattered into the outer detector channels in a manner that is not properly modeled can be addressed with the observed channel 8 asymmetry. Since the kinematic endpoint lies in channel 7, the signal observed in channel 8 comes entirely from the tails of the resolution function, and amounts to roughly 7% of that seen in its inner neighbor. Assuming that any additional low asymmetry signal is roughly uniform between these two outer channels, the asymmetry measured in channel 8 is then 14 times more sensitive to this possible contamination than channel 7. For a ten day period in January 1995, a preradiator for a neutral beamline counter got stuck in the inserted position, and the channel 8 asymmetry was observed to drop by over 5%. Presumably, the backscattered Compton photons were showering into the CKV detector at high

Table 3.1: Systematic uncertainties affecting the CKV channel 7 calibration

Systematic Uncertainty	$\delta P_e^7/P_e^7$
Response Function	0.20%
Analyzing Power Tracking	0.10%
Radiative Corrections	0.10%
BSM Preradiator Correction	0.09%
Residual Contamination	0.12%
Total Uncertainty	0.29%

angle, although the detector simulation was never able to adequately model this effect. The beam polarization measurement was corrected by nearly 1% during this period to account for the observed contamination, and a systematic uncertainty equal to 100% of this correction has been assumed. Since less than one tenth of the total 1994-95 SLD data was collected in this period, the overall error is less than 0.1%.

Table 3.1 lists the systematic uncertainties associated with the detector calibration for the 1994-95 run. While each detector channel makes an independent measurement of the electron beam polarization, the calibration uncertainties grow for channels away from the well determined kinematic endpoint. For this reason, only CKV channel 7 is used exclusively to measure the electron beam polarization, while the relative agreement of 0.3% between channels 6 and 7 provides a nice cross check of the overall calibration procedure. Other cross checks, such as the asymmetries observed when the lead preradiator is removed, further verify this calibration accuracy.

3.6   Laser Polarization

As the asymmetry seen in the CKV detector is the product of the electron and photon polarizations, an accurate measurement of the Compton laser polarization must be performed in order to determine the electron beam polarization.   The

E Field Vector

$$\begin{pmatrix} 1 \\ 0 \end{pmatrix} \qquad \begin{pmatrix} \cos(\phi_{cp}/2) \\ -i \sin(\phi_{cp}/2)\, e^{i\phi_{ps}/2} \end{pmatrix} \qquad \begin{pmatrix} 1 \\ i \end{pmatrix}$$
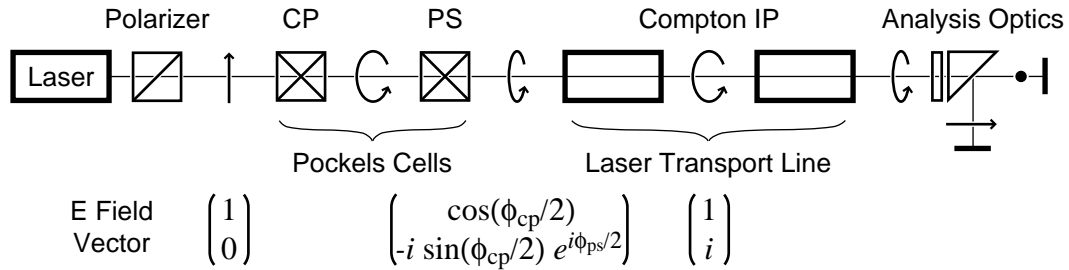
Figure 3-7: The linear polarization states of the Compton laser beam are shown at various points along the laser transport line. Phase shifts added by the CP and PS Pockels cells cancel out the phase shifts in the first part of the transport line, resulting in circular laser polarization at the Compton IP.

circular polarization of a laser can be measured in a straightforward manner on an optics bench using a quarter-wave plate and a calcite prism to separate the two orthogonal circular polarization states of the incident beam. The relative intensities of the two beams separated by the prism, measured with a pair of photodiodes or other suitable optical detectors, then gives a direct measurement of the left and right handed components present in the original beam. In the Compton polarimeter, the laser polarization is measured in this fashion both before and after the collision process. The laser polarization of interest, however, is at the Compton IP inside the SLC vacuum enclosure where a direct measurement of this type is impossible. Due to phase shifts induced by the laser transport line, the laser beam polarization at the CIP can vary by up to a few percent compared to the polarization directly measurable at the Compton laser bench and the analysis box.[1]

A block diagram of the Compton laser system is shown in Figure 3-7. The linear polarization state produced by the frequency doubled Nd:YaG laser is converted into circular polarization by means of a Pockels cell. This electro-optic crystal produces a phase shift between the two linear polarization components defined by the optical

---

[1] The phase compensated mirrors in the laser transport line keep this difference to only a few tenths of a percent between production and collision. In exiting the SLC vacuum, however, the beam must pass through a large window stressed by the pressure differential. This is the only element between the CIP and the analysis box, although it causes a polarization difference of over a percent.

axis of the device. The magnitude of the phase shift is determined by the applied Pockels cell drive voltage, and in this case a large voltage ($\sim$ 1700V) is applied to create an effective quarter-wave plate. As in the polarized electron source, the sign of the applied voltage determines the helicity of the circular polarization state produced. A second Pockels cell, rotated by 45° with respect to the first, is operated at a voltage near zero to provide an additional phase shift so that light with an arbitrary elliptical polarization can be generated. If the phase shifts produced by the Pockels cells are chosen to compensate for the net phase shift induced by the first laser transport line, the photons will arrive completely circularly polarized at the Compton IP. The two Pockels cells are denoted the CP cell and the PS cell respectively.

Pockels Cell Scans

Since the asymmetry seen in the CKV detector is proportional to the Compton laser polarization, and lasers can be routinely polarized to nearly 100%, the change in the observed CKV asymmetry as a function of the Pockels cell voltage settings can be used to measure the deviation from an optimally polarized laser beam at the CIP. This technique is implemented through a procedure known as a *Pockels cell scan.* First, the CP cell voltage is set to produce optimal circular polarization on the laser bench where it can be measured with a prism and photodiodes. This voltage is typically near $\pm$1700 volts, while the PS cell voltage is held near zero. Compton polarimeter runs are then taken at different voltage settings for the CP and PS cells. To first order, the observed CKV asymmetry will have a sinusoidal dependence on the Pockels cell voltages, with the peak indicating the optimal operating point.

These scans are performed automatically as part of the list driven scanning sequence as described in Section 3.4, and an example is shown in Figure 3-8. This provides two important pieces of information. First, the nominal operating voltages for the Pockels cells can be monitored and adjusted to account for slow drifts in the
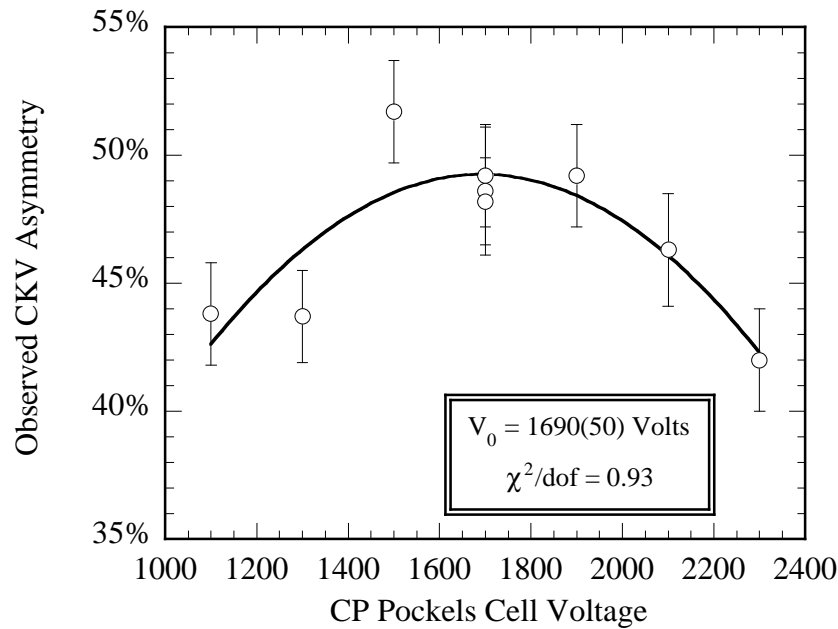
Figure 3-8: Data from a CP Pockels cell scan is shown. The observed CKV channel 7
asymmetry is shown as a function of CP voltage setting. The nominal CP
cell voltage in this case was 1700 volts, while the optimal setting is measured
to be 1690 ± 50 volts.

Compton laser system. These adjustments to the nominal setpoints typically do not
have to be performed more often than a few times a month, and this constant mon-
itoring ensures that the Compton laser is always operating very close to its optimal
polarization at the Compton IP. Second, every scan makes a direct measurement
of what laser polarization is being generated by the nominal operating voltages by
measuring the difference between the nominal and optimal settings. Diurnal tem-
perature variations in the laser and the transport line can cause changes on the
order of a few tenths of a percent which must be measured. A single Pockels cell
scan can measure the optimal operating voltages to a statistical precision of ~ 50
volts which measures the difference between the nominal and optimal laser polar-
ization to better than 0.1% at the peak. As this error grows quadratically as the
nominal operating voltage is moved off peak, an added benefit of keeping the laser
polarization optimized is a better measurement of its value.

Unpolarized Fraction

While the Pockels cell scan technique can make a relative polarization measurement with respect to the maximum achievable laser polarization, an absolute measurement is not being performed. In order to determine the absolute polarization of the laser beam at the Compton IP, some estimate must be made of the unpolarized fraction present in the laser beam at that point. The initial linear polarization state before the CP cell is produced with a precision linear polarizer. At this point the unpolarized fraction is less than 1×10^{-4}. The unpolarized fraction present after the Pockels cells can be directly observed on the laser bench by measuring the extinction of the circularly polarized beam by the helicity selecting waveplate-prism combination. In practice, the left and right photodiode signals are measured while scanning the Pockels cell voltages across their entire operating range. No evidence for any unpolarized component is seen, and the residuals from zero near the extinction point provide a measurement accuracy of better than 0.1%. To limit the possibility that the laser beam becomes unpolarized on its way through the transport line, an identical measurement is made at the same time with photodiodes in the analysis box after the Compton IP. These photodiodes also measure complete extinction, although with somewhat worse accuracy due to the noisy environment in the SLC tunnel where the analysis box is located.

These extinction scans only take ten minutes to complete, and are performed every few hours immediately after a Pockels cell scan as a part of the normal Compton polarimeter running. The systematic uncertainty associated with measuring the unpolarized fraction is estimated to be 0.2% over the course of the 1994-95 SLD run from the observed residuals of these extinction scans on the analysis box photodiodes. This turns out to be the dominant systematic uncertainty in the entire laser polarization measurement, as the Pockels cell scan method has been shown to be an unbiased measurement to better than its inherent statistical precision of 0.1%. The individual Pockels cell scans are then used as a time dependent measurement of the

laser beam polarization over the course of the entire 1994-95 running period. The luminosity weighted laser polarization in 1994-95 was found to be $(99.63 \pm 0.20)\%$ where the uncertainty is entirely systematic. A more complete treatment of the laser polarization measurement can be found in[39, 37].

3.7 Asymmetry Corrections

There are a number of small, instrumentation related corrections which must be applied to the raw asymmetry measured by the Compton polarimeter. In addition, while knowledge of the overall gain is not important in making an asymmetry measurement, the extent to which the CKV detector response is linear directly limits the accuracy of the overall measurement.

The CKV Cherenkov signal is directly measured with highly linear Hammamatsu R1398 photomultiplier tubes. The signals from these tubes are transported out of the SLC final focus on 60 meter lengths of RG-214 signal cables which are terminated into PE-8304 decoupling transformers to suppress common-mode noise and ground loops. The signals are then amplified by LeCroy 612A fixed-gain ($\times 10$) current amplifiers which directly drive the Lecroy 2249W AC coupled ADCs. The amplifiers and isolation transformers were added before the 1994-95 SLD run in an attempt to better match the linear output of the photomultiplier tubes to the dynamic range of the Lecroy ADCs. While all of this hardware is, in principle, highly linear across its normal operating range, it is important to measure and directly test the entire readout system under normal operating conditions.

Laser Pickup

The first correction which must be applied results from electronic noise generated in the readout electronics by the fast, high-voltage pulse used to Q-switch the Compton YaG laser. The power supply driving the Compton laser is not perfectly isolated

from the rest of the system, and as a result an observable shift of the ADC pedestals can be seen when the laser fires. Since the laser-off machine pulses are used to subtract the beam related background present in the CKV channels, this laser pickup of a few tenths of an ADC count directly biases the asymmetry measurement.

It is a fact of life at the SLC that not every machine pulse brings beam all the way through the machine to the SLD. Aside from the periods of time when the beam is actually shut off, even when SLC is nominally delivering luminosity running there are always a large number of machine cycles in which the electrons are absent. These SLC beam dropouts provide the ability to directly measure and monitor the laser pickup in every CKV detector channel during the course of normal operations. The observed difference in ADC pedestals for the laser-on and laser-off dropout data is used offline as a time-dependent correction to the measured asymmetry. The laser pickup is reasonably stable in Channel 7 with a value around -0.25 ADC counts over the course of the entire 1994-95 run. The associated systematic uncertainty on asymmetry measurement due to this correction is much less than 0.1%.

Electronic Cross Talk

Other sources of electronics noise can come from cross talk between the various CKV detector channels, either in the amplifier or in the ADC directly. To check for this sort of noise the following two tests were performed.

In the first test, the voltage on one CKV photomultiplier tube was turned up to provide a large signal while the remaining channels were turned off. The cross talk from this channel into the other eight was then measured by comparing the pedestals observed with and without signal present, after correcting for laser pickup. This procedure was repeated for all nine CKV detector channels to map out the 'one to many' cross talk characteristics. No observable effect was measured at the level of a few tenths of an ADC count.

In the second test, the 'many to one' cross talk characteristics were tested by

consecutively turning off only one CKV photomultiplier tube and measuring the signal leakage into this channel from the other eight. Again, no clear evidence for any channel cross talk is seen beyond the 0.2 - 0.3 ADC count level, which corresponds to a systematic uncertainty on the measured CKV asymmetry of 0.2%.

Detector Linearity

The Compton asymmetry formed in Equation 3.14 implicitly assumes that the observed detector response has a linear dependence on the actual input signal. Any deviation from a linear response will directly effect the measured asymmetry, and it is important to limit or correct any non-linearities in the system to a few tenths of a percent. Unfortunately, this is always easier said than done.

The electronics component of the readout chain can be tested to high precision through the use of an electronics linearity tester. For this test, a Phillips 7120 Precision Charge/Time Generator was inserted into the Compton data acquisition to provide a controlled reference pulse with the approximate rise time and pulse width of the actual CKV PMT signal. In special tests running at 120 Hz, this device was used to map out the linearity response of each of the electronics channels to a fraction of an ADC count.[45] All of the electronics channels display some deviation from linear behavior especially at the low end, an example of which is shown in Figure 3-9. The high end linearity is not really an issue as the CKV signal plus background levels are typically below 500 ADC counts. To verify that this is a real problem with the electronics, and not a problem with the linearity tester itself, a number of additional tests were made using a variety of signal attenuators and different hardware configurations.

It is not enough to simply measure these linearity curves, as they do not directly indicate what the net effect might be on the measured asymmetry. Correction functions based on these measured electronic linearity responses are applied directly to a uniform sampling of the raw polarimeter data, and the difference between the
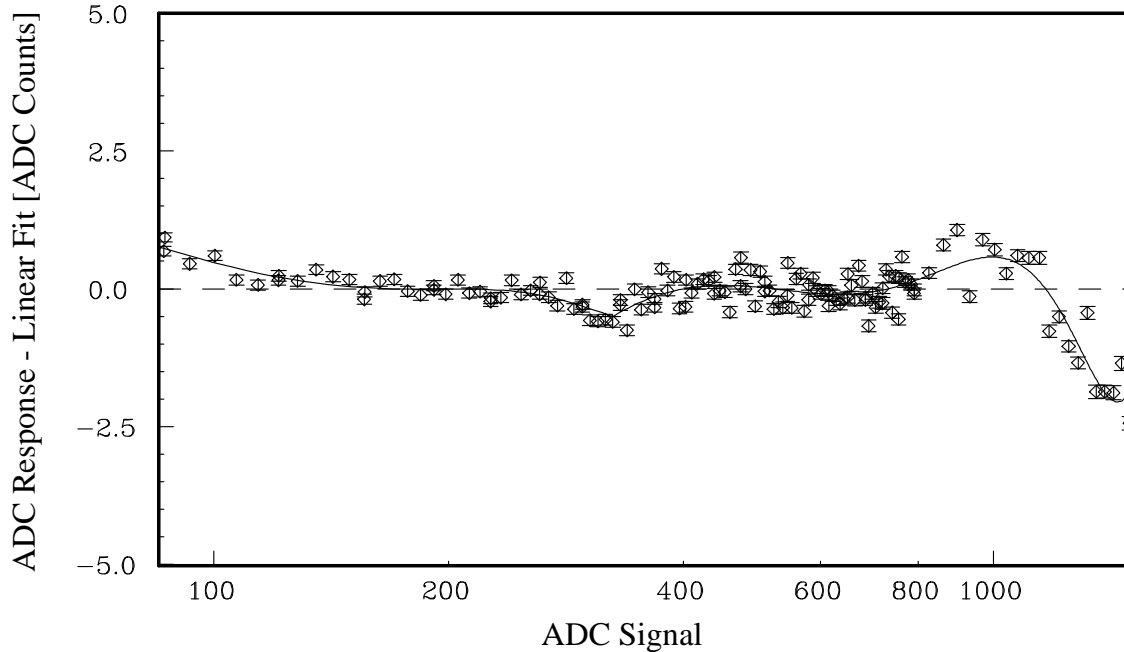
Figure 3-9: The deviation from a linear response for the CKV channel 6 readout electronics is shown as a function of ADC response. The solid curve is the result of a polynomial fit. Some deviation is seen at the low end near the 80 ADC count pedestal, along with the expected ADC saturation at large pulse heights.

corrected and uncorrected asymmetries were calculated for channels 6 and 7. Since a full reprocessing of the raw data is a somewhat painful (although not impossible) task, the observed difference in this sampling of the raw data has been applied as a global correction the raw asymmetries calculated from the summary banks. The corrections applied are listed in Table 3.2, and were not observed to have any significant time dependent structure over the course of the 1994-95 run.

While this technique provides a nice test of the electronics themselves, it does not test the entire (PMT + electronics) readout system. A scheme is currently under development to test the full system to high precision using a UV laser to inject reference pulses directly into the CKV detector, however the commissioning of this calibration system is still in progress. In the absence of a direct comprehensive test, two data based methods have been developed to limit the size of possible

non-linearities in the system. Both of these methods involve taking data automatically using the list-based scanning technique employed successfully to measure the Compton laser polarization.

The first test, a *laser power scan*, involves taking consecutive polarimeter runs while adjusting the laser power transmitted to the Compton IP. As the observed signal size is directly proportional to the laser spot intensity, the measured Compton asymmetry can then be compared at different signal sizes to test the linearity of the entire system. The main problem with this technique is that while the signal size can be reduced, the beam-related background response remains constant, limiting the ability of this technique to probe the lowest end of the ADC dynamic range. One can argue that this is somewhat irrelevant since it is the differential linearity between the background and the two signal states which really matters, although this is only approximately true. The data for channel 6 is shown in Figure 3-10, with no apparent change in the measured asymmetry beyond $\sim 0.3\%$ across the accessible dynamic range.

The second test, a *PMT voltage scan*, involves taking consecutive polarimeter runs while adjusting the applied photomultiplier tube voltage. Normally, changing the voltage applied to a PMT merely changes the gain of the tube. The PMT bases used in the Cherenkov detector, however, are constructed with a two stage design whereby the front end voltage can be varied while the voltage across the last few dynodes is held fixed. In the 1993 SLD run, before the $\times 10$ amplifier was installed, the largest linearity problem in the system was with the high end saturation of the photomultiplier tubes caused by space-charge effects in these last few dynodes. In this case, changing the front end voltage provides a direct measurement of this saturation. The addition of the $\times 10$ amplifier for the 1994-95 SLD run eliminated this source of non-linearity, however, and the applicability of the voltage scan data for exploring the remaining linearity problems at low pulse height is not clear.

For each voltage scan run a ratio is formed between the asymmetry measured in
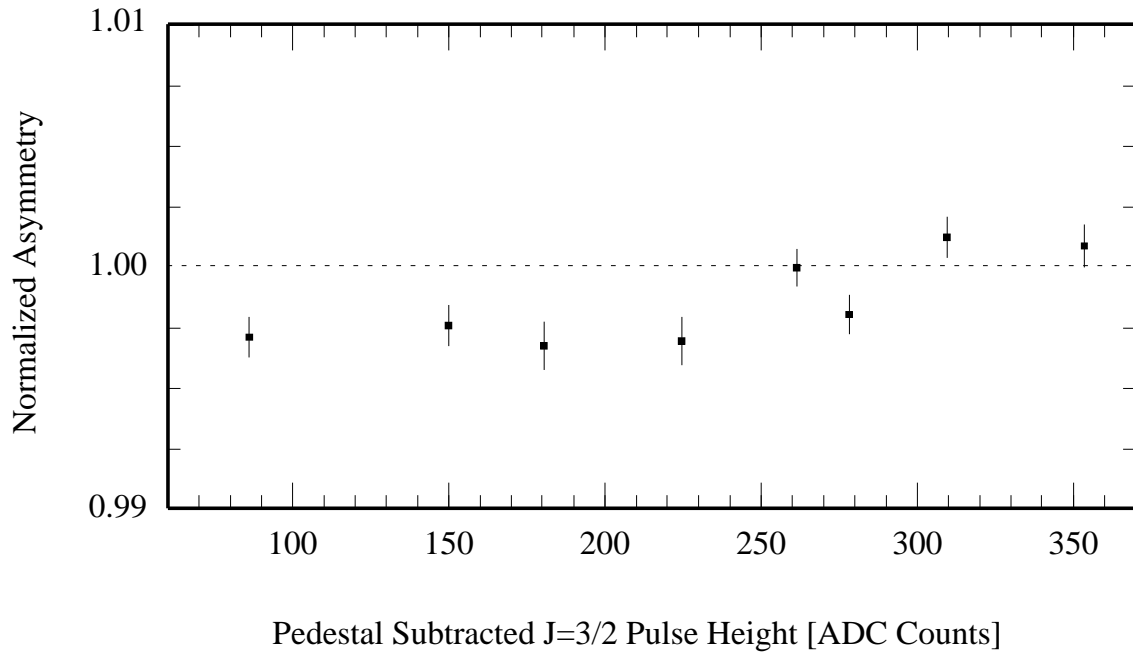
Figure 3-10: The normalized channel 6 asymmetry is shown as a function of the pedestal
subtracted J=3/2 ADC response for data taken during a laser power scan.
The measured asymmetry observed at various levels of incident laser power
are normalized to the asymmetry measured at nominal power close in time
to the power scan data to take out real changes in the beam polarization.

the channel of interest and a reference channel, typically channel 4, the voltage of
which is held fixed. The data, shown if Figure 3-11, shows reasonable behavior at
high pulse height, but exhibits a large deviation of a few percent at lower response.
To assess the impact of this possible non-linearity over the course of the run, an ad-
hoc response function was generated to effectively flatten out the observed voltage
scan asymmetry ratios. These ad-hoc functions are then applied to the sampling of
raw data in the same way as the electronic corrections to calculate the net effect
on the measured raw asymmetry. The results, shown in Table 3.2, show a large
-0.5% effect on the asymmetry measured by CKV Channel 7. The RMS width of
the asymmetry correction associated with the ad-hoc linearity correction is 0.2% in
Channel 7.

With a -0.22% correction already being applied to account for the precisely
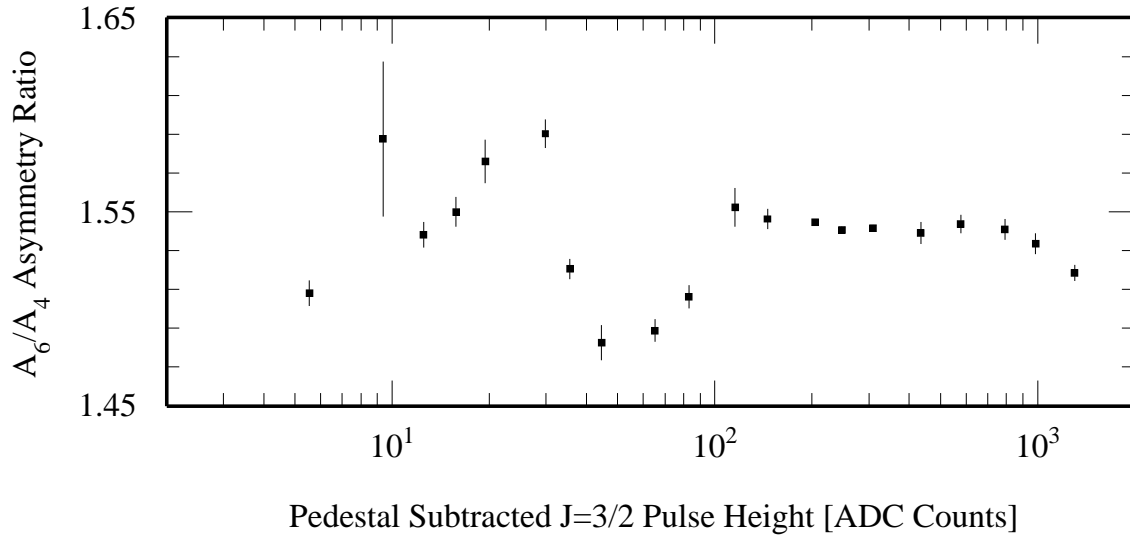
Figure 3-11: The normalized asymmetry measured in CKV channel 6 during a voltage
scan is shown as a function of the pedestal subtracted J=3/2 ADC re-
sponse. During a voltage scan, the front end PMT voltage in a particular
channel is varied while the channel 4 voltage is held fixed to normalize
out any real polarization drifts. Excursions of up to 4.5% are seen at
low pulse heights, although all of the data used in the beam polarization
measurement are taken above 100 ADC counts.

measured electronics-only linearity deviations, a systematic uncertainty of 0.5% is
conservatively estimated to bound the maximum possible size of any additional
linearity problems in the system. At the present time, the low pulse height voltage
scan anomaly is believed to be a relic of the low PMT voltages, and not a real
linearity problem at low pulse height. Without any data to prove otherwise, however,
the systematic uncertainty associated with the detector linearity can not be reduced
below the 0.5% level.

Table 3.2: CKV Linearity Test Results

Correction Applied	$\mathcal{P}_e$ (Ch. 6)	$\mathcal{P}_e$ (Ch. 7)
None	0.77325	0.76860
Electronic Only	0.77232 (-0.12%)	0.76692 (-0.22%)
Volt Scan *ad-hoc*	0.77279 (-0.06%)	0.76481 (-0.49%)

3.8   Compton - SLD Differences

The Compton polarimeter system sits 30 meters downstream from the SLC interaction point, and it is important to determine how closely the longitudinal polarization measured at the Compton polarimeter corresponds to the polarization of the electrons colliding at the SLD. While there are no dipole magnetic fields between the SLC interaction point and the Compton IP to precess the polarization vector away from a longitudinal orientation, there are a number of small effects which are important at the level of a few tenths of a percent accuracy.

Final Focus Spin Precession

The electron motion through the various quadrupole and sextupole magnets between the SLC IP and the Compton IP has been studied to determine the size of any possible net spin precession.[46, 47]

The single largest spin precession effect in the SLC Final Focus involves the strong focusing provided by the pair of superconducting quadrupole triplets immediately on either side of the SLC IP. The angular beam divergence at collision is approximately $350 \times 250 \mu$Rad which, when combined with the factor of $\gamma(g-2)/2$ leads to a spin precession of roughly 36×26 mRad. A direct spin rotation of 30 mRad will reduce the longitudinal spin polarization of the 45.6 GeV electron beam by only 0.05%. To determine the actual size of this effect, the spin precession must be integrated across a realistic Gaussian beam divergence profile to arrive at the net depolarization factor. In this calculation, the non-zero beam divergence at the Compton IP is taken into account, while the possibility of pulse to pulse jitter in the incident electron position determines the systematic uncertainty. Since the electron transport is operationally tuned to optimize the polarization measured at the Compton polarimeter, the longitudinal polarization present at the SLC IP is less

than the measured value by a factor of

$$\frac{\mathcal{P}_e^{SLC}}{\mathcal{P}_e^{CIP}} - 1 \simeq -(0.112 \pm 0.012)\%, \tag{3.15}$$

which is directly applied as a correction to the electron polarization measurement.

The possible spin precession resulting from the outgoing electron beam traveling off center through the remaining quadrupole lattice elements due to beam steering effects is found to be negligible.

Depolarization Effects

The possible depolarization of the electron beam by the collision process itself has been calculated in terms of the observed beam disruption.[48] Using the typical disruption observed in the collision process, the predicted electron depolarization is less than 0.1%. This depolarization was directly measured towards the end of the 1995 run with a special test. For a four hour period, the beams were taken out of collision every 20 seconds by dumping the positron beam at the end of the linac for a duration of 10 seconds. The measured polarization difference is consistent with zero, and has been used to set a depolarization limit of

$$\frac{\mathcal{P}_e^{SLC}}{\mathcal{P}_e^{CIP}} - 1 < 0.08\% \qquad (95\% \; C.L.). \tag{3.16}$$

Chromaticity Effects

While the Compton polarimeter measures the polarization of the entire electron bunch, chromatic aberrations in the SLC final focus optics reduce the luminosity generated from the off-energy beam tails. Because of the energy-dependent spin precession experienced by the electrons in the SLC North Arc, these off-energy beam tails have a systematically lower net longitudinal polarization than the beam core. This effect, known as the *chromaticity effect*, was the single largest correction
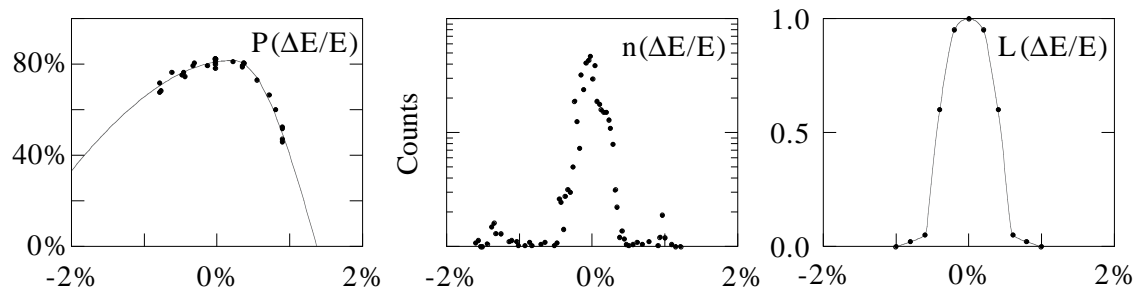
Figure 3-12: The three functions contributing to the chromaticity effect are shown as a function of relative energy. The first figure is an example of a measurement of the polarization dependence on energy. The second figure, on a logarithmic scale, is wire scan data measuring the energy profile of the electron beam. The third figure shows the most conservative model-based luminosity prediction resulting from the final focus optics design. While the polarization producing Z bosons at the SLC IP can be found by integrating the product of all three figures, the Compton polarimeter has a much larger energy acceptance and the measured polarization is essentially the product of the first two figures only.

applied to the 1993 beam polarization measurement and contributed a 1.1% relative systematic uncertainty to the knowledge of the beam polarization at the SLC IP in that year.

For the 1994-95 SLD run, a number of measures were taken to control the chromaticity effect both in terms of reducing the overall size of the effect through machine operations, as well as better monitoring procedures so that the size of the effect could be directly measured. The three components needed to produce a polarization difference are shown in Figure 3-12. Improving any of the three distributions will reduce the size of the chromaticity effect, either flattening the polarization dependence on energy, reducing the energy tails in the electron bunch, or improving the energy acceptance of the SLC Final Focus.

A significant low energy tail on the electron beam, present in the 1993 run, was eliminated in the 1994-95 run by adjusting the bunch compression provided at the exit of the North damping ring. The energy profile of the electron beam is now directly measured approximately every two hours by a wire scanner located

in the North Final Focus at a point of high dispersion where the transverse beam position is highly correlated with energy. A total of four measurements of the polarization dependence on beam energy were performed to characterize the electron spin transport through the North Arc. Additionally, extra care was taken during the 1994-95 running in the North arc spin bump setup to keep this energy dependence as low as possible.

The final focus improvements installed before the start of the 1994 run were supposed to reduce the luminosity-limiting, third-order chromatic aberrations present in the final focus optics. While accurately measuring this luminosity dependence on beam energy is tricky at best, an approximate comparison can be made between the observed rate of Z boson production as a function of beam energy, and an optics motivated luminosity model. Additional measurements of the beam spot sizes as a function of energy also support the optics motivated model. The actual cross section dependence on energy determined by the Z boson lineshape is small compared to the predicted luminosity cutoff and can be safely ignored.

Using the data acquired during the course of the 1994-95 SLD run, the size of the chromaticity effect can be computed entirely from measured quantities. Ultimately, the systematic uncertainty for determining the size of the chromaticity effect in the 1994-95 SLD run is found by comparing the size of the effect using the most extreme distributions for both the polarization dependence on energy and the luminosity dependence on energy. The luminosity weighted polarization due to the chromaticity effect in the 1994-95 SLD run is determined to be

$$\frac{\mathcal{P}_e^{SLC}}{\mathcal{P}_e^{CIP}} - 1 = (0.20 \pm 0.14)\%, \tag{3.17}$$

which is applied as a correction to the beam polarization as measured by the Compton polarimeter.[49] The equivalent correction to the 1993 polarization measurement

was

$$\frac{\mathcal{P}_e^{SLC}}{\mathcal{P}_e^{CIP}} - 1 = (1.7 \pm 1.1)\%, \tag{3.18}$$

which was much larger both in terms of the size of the effect as well as the accuracy to which it was measured.[50]

3.9   Polarimeter Summary

Every aspect of the Compton polarization measurement has been improved for the 1994-95 SLD run. The complete list of systematic uncertainties can be found in Table 3.3. Currently, the single largest uncertainty is due to the ability to measure the linearity of the entire Cherenkov detector readout chain. Improvements in the near future, including a laser-based linearity calibration system, will probably reduce this error to the level of 0.3%. The luminosity weighted beam polarization determined by matching individual polarization measurements to hadronic Z boson decays observed over the course of the 1994-95 SLD run is found to be

$$< \mathcal{P}_e >= (77.23 \pm 0.52)\%, \tag{3.19}$$

where the uncertainty is purely systematic due to the various effects summarized in this chapter.[51] The interchannel consistency uncertainty applied to the 1993 data is due to an observed discrepancy in the beam polarization measured by the various CKV detector channels which was larger than the expected calibration uncertainty. In the 1994-95 data, the polarization measured by the two outer channels agrees quite well, and this additional source of systematic uncertainty has been eliminated.

Table 3.3: Total systematic uncertainties for the electron polarization measurement

Systematic Uncertainty	$\delta\mathcal{P}_e/\mathcal{P}_e$ (1993)	$\delta\mathcal{P}_e/\mathcal{P}_e$ (1994-95)
CKV Detector Calibration	0.4%	0.29%
Laser Polarization	1.0%	0.20%
Electronics Noise	0.2%	0.20%
CKV Linearity	0.6%	0.50%
Interchannel Consistency	0.5%	-
IP to CIP Differences	1.1%	0.17%
Total Uncertainty	1.7%	0.67%

Chapter 4

Event Selection and Reconstruction

The SLD is a general purpose particle detector designed to efficiently detect all interesting physics processes generated by e^+e^- collisions near the Z pole energy. For the most part, the triggering and reconstruction of the events observed by the SLD is shared among the various physics analyses performed on this data. From this common pool of interesting 'physics' events, an event selection is then performed by each particular analysis to isolate only that set of data which is useful in each particular instance. This chapter will briefly summarize the general detector triggering and reconstruction process, as well as describe the particular selection used in this analysis to identify and classify the various observed decays of tau lepton pairs.

4.1 Detector Trigger

The expected rate of interesting physics events produced by the SLC is on the order of one per minute. With a collision rate of 120 Hz, it is infeasible to record every beam crossing seen by the SLD, and some amount of detector triggering logic is employed to reduce the amount of data written to tape. Compared to other particle physics experiments, the demands on the SLD trigger logic is quite mild, and a

straight forward set of criteria are sufficient to reduce the detector trigger rate to an acceptable 0.3 - 0.5 Hz. A variety of different triggers are independently evaluated to ensure the efficient detection of interesting physics events.

For the selection of tau pair events, there are four triggers which have a significant probability of being satisfied:

- The track trigger, which requires a minimum of two tracks at least 120° apart in the CDC;

- The energy trigger, which requires at least 6 GeV of total energy observed in the LAC;

- The hadron trigger, a hybrid of the energy and track triggers, which requires at least one track plus over 2 GeV of LAC energy;

- The wide-angle Bhabha (WAB) trigger, which requires at least 15 GeV of energy to be deposited in the LAC EM section;

As the trigger decision is made on every beam crossing, there is only a rudimentary amount of information available on which to base the trigger algorithm.

At the trigger level, tracking is performed by comparing the pattern of CDC wire hits with a lookup table stored in the memory of the below-line FASTBUS modules. If nine out of the ten possible layers contain hits on at least six of the possible eight sense wires, that sequence of hit cells is defined to be a *track*. For the observed LAC energy, a threshold is applied to each tower to reject electronics and beam related noise. Only those towers recording energies above this threshold, set at approximately twice the energy which would be deposited by a minimum ionizing particle, can contribute to the energy sum. Each of the four triggers listed above also contain vetoes to reject clearly unusable events. The track trigger, for instance, will be vetoed if more than 275 of the 640 CDC cells satisfy the six hit criterion.

Every triggered event observed by the SLD is written to tape for future processing. While knowledge of the absolute trigger efficiency is not required in this analysis, it has been estimated that the combination of the four triggers listed above are effectively 100% efficient for triggering tau pair events produced within the fiducial volume of $|\cos\theta| < 0.7$ where nine out of ten CDC layers can be intersected.[52]

4.2 Tau Filter and Reconstruction

The rate of triggered data which is written to tape is still a factor of at least 30 larger than the expected interesting physics rate. As the full reconstruction of an event is a tremendously resource intensive operation in terms of computing time, a preselection process known as *filtering* is applied to the triggered data to determine which events to reconstruct.[1] Of the variety of filters applied to the data, only those events which pass the Tau selection filter are used in this analysis, although all filtered events are treated identically by the reconstruction process. At the filter stage, a somewhat more sophisticated fast tracking algorithm is applied, although still far short of the full tracking reconstruction that will eventually be performed. The only requirement to satisfy the tau filter is that the scalar momentum sum from all observed tracks is greater than 1 GeV/c. This simple filter is adequate to reduce the triggered data sample by a factor of around ten, and all filtered events are then fully reconstructed by the offline reconstruction package.

The process of reconstruction involves turning the observed raw detector hits into physically motivated objects like tracks representing the passage of charged particles. Each detector component is first reconstructed individually: tracks are found in the CDC, energy clusters are formed in the LAC, Cherenkov rings are found in the CRID, etc. After all of these fundamental objects are found, the data

---

[1] Reconstruction times vary widely, primarily due to the track finding pattern recognition algorithm used in the CDC. The reconstruction of a typical hadronic Z decay can take up to several seconds of computer time.

from the various detectors which appear to be related to the same physical particle are connected, or *linked*, across all of the detector components into one logically grouped data structure.

In the resulting data, there are two distinct classes of objects: *tracks* and *unassociated clusters*. A track represents a single charged particle traversing the detector, and will include information from at least the CDC, and quite possibly every detector component. Unassociated clusters, meanwhile, are individual clusters of energy observed in the calorimeter which are not linked to a CDC track segment. These clusters mostly correspond to neutral particles such as individual photons, although there is always some amount of calorimeter noise which will create extra clusters.[2] Additionally, the track-cluster association algorithm is not perfect and there is always a chance that a cluster produced by a charged track will not get linked properly and an extra unassociated cluster will be found instead.

4.3   Tau Event Selection

At this point the event has been reconstructed, and all of the physics information of interest is now available to select and classify the tau pair decays. As Z bosons decay to tau pairs only 3% of the time, most of the events selected by the tau filter are not tau pair events at all. The dominant process of hadronic Z decays are quite distinct from the low multiplicity tau pair events, and a general purpose set of tau selection criteria is applied to isolate a pure sample of tau pair events.

To perform this selection, a number of event quantities are calculated from the reconstructed data. First, the event is divided into two hemispheres based upon its

---

[2] One particular source of calorimeter noise unique to the SLC environment are muons created upstream of the IP by the incoming beams scraping off collimators and other structures. A set of large toroids deflect these muons away from the main beamline, and most of these particles end up traveling longitudinally through the LAC. Depending on beam conditions, there can be several of these SLC muons per event, and a special algorithm is used in the calorimeter reconstruction to identify and ignore the energy deposited from this source.[53]

thrust axis. The thrust axis is the vector from which the transverse momentum sum of all observed tracks in the event is minimized. Around the thrust axis, a cone of $15°$ is defined, within which tracks from a real tau pair event are expected to be found. The particles in each hemisphere lying within this cone are defined to be *jets*, and each jet direction is iterated to minimize the transverse track momenta in each hemisphere independently. The invariant mass of each jet is calculated assuming that the charged tracks are pions and the unassociated clusters are photons. The following selection criteria are then applied to select tau pair events:

- At least one track is found in each hemisphere;

- At least one jet has a charge sum $|\sum Q| = 1$;

- Total visible energy of the event is greater than 10 GeV;

- Number of tracks in jets is less than 7;

- Number of unassociated clusters in jets is less than 9;

- No tracks are found outside of the jet cones;

- Total visible energy outside jets is less than 5 GeV;

- Acolinearity angle between the jets is less than $20°$;

- Multi-track jets have invariant mass less than 2.3 GeV/c^2;

- 1-1 events have a track acolinearity angle greater than 10 mrad;

- Scalar sum of two largest track momenta less than 65 GeV/c;

- Total EM LAC energy less than 62.5 GeV;

- Missing momentum vector in the event satisfies $|\cos\theta_{\mathrm{miss}}| < 0.88$.
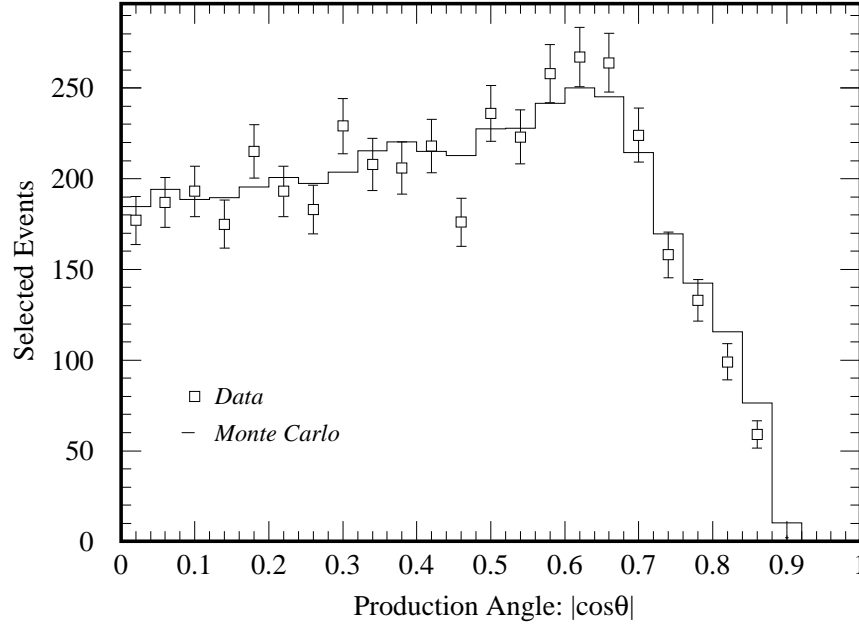
Figure 4-1: The number of events passing the generic tau selection are shown as a function of production angle. The expected distribution as estimated by Monte Carlo data shows good agreement. The total number of Monte Carlo events has been normalized to the data.

For the tau event selection, visible energy is defined as the observed track momenta plus the energy deposited in the LAC from unassociated clusters.

Using samples of tau Monte Carlo data, this selection procedure is estimated to be nearly 80% efficient for selecting true tau pair events out to a production angle of $|\cos\theta| < 0.65$, and then tails off as the tracking efficiency drops. Using Monte Carlo generated samples of other physics processes, the selected events are estimated to be 98% pure, with the dominant contamination coming from wide-angle Bhabha events (0.9%) and muon pair production (0.7%).[52]

The number of selected events are shown in Table 4.1 along with a Monte Carlo estimate of the selection efficiency and non-tau background. Using these Monte Carlo estimates, the effective luminosity can be found using 1.467 nb as the cross section for tau pair production at the Z pole. The total effective luminosity of 5.14 pb^{-1} is approximately 96% of the 5.34 pb^{-1} value directly measured by the

Table 4.1: Tau Selection Results

Run Period	*Events*	*Efficiency*	*Purity*	$\mathcal{L}_{eff} [pb^{-1}]$
1993	1,295	0.527	0.979	1.64
1994 Summer	544	0.512	0.979	0.71
1994 Fall	1,494	0.577	0.979	1.73
1995	950	0.596	0.979	1.06
Total	4,283	0.556	0.979	5.14

luminosity monitor for the same running period. This difference agrees well with the estimated CDC duty factor of $\sim 95\%$.

Since the electron beam polarization is an important component of this analysis, an accurate measurement of the electron beam polarization is required to have been made within one hour of each event considered. For every selected tau event, the polarimeter run closest in time is associated with that event to provide a measure of the electron beam polarization at the time when the event was recorded. This polarization matching is successful for 95.4% of all selected tau events.

4.4   Particle Identification

In order to spin analyze the produced tau leptons, the decay products of the taus must be properly identified. Four spin-sensitive one prong decay modes are used in this analysis, while the remaining unidentified decays are classified according to their track topology. The muonic decay mode $\tau \to \mu \bar{\nu}_\mu \nu_\tau$ is readily identified by the penetration of the muon through the WIC tracking planes. The electronic decay mode $\tau \to e \bar{\nu}_e \nu_\tau$ is also readily identified by considering the characteristic large energy deposition of the electron in the EM section of the LAC.

The two hadronic decay modes are somewhat more difficult to isolate from other processes. The single pion decay channel $\tau \to \pi \nu_\tau$ is identified by considering the penetration and shape of the hadronic shower produced in the LAC. No attempt is
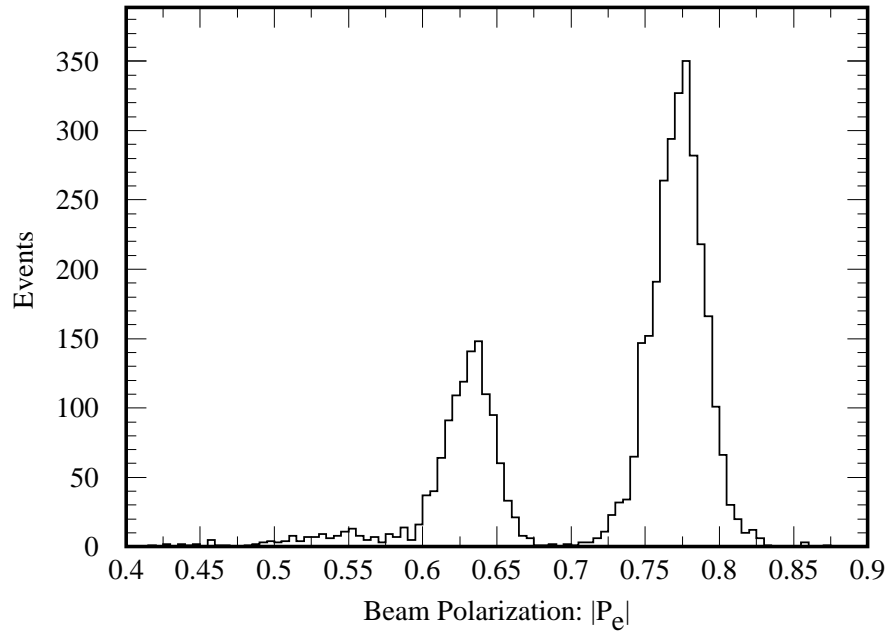
Figure 4-2: The measured beam polarization associated with each selected tau event is shown. The polarization values below 70% all come from the 1993 data. The electron beam polarization during the 1994-95 SLD run was very stable near 77%.

made to separate the pion decay modes from the kaon decay modes in this channel, and in fact both are selected with reasonable efficiency. Rather, a small admixture of kaon decays is then assumed to be present in the identified sample. The rho decay mode is actually the process $\tau \to \pi\pi^0\nu_\tau$ which is dominated by the rho resonance. This mode is separated from the single pion and non-resonant multi-pion channels by attempting to reconstruct the invariant mass of the underlying rho meson.

The identification of the fully leptonic and hadronic tau decay modes has been largely the work of J. Quigley and N. Allen respectively, and has been used in an analysis measuring the Lorentz structure of the tau decay.[54] A more complete description of the identification method can be found in their respective theses,[52, 55] and while the selection strategy used in this analysis has not been modified from their original work, the actual steps of the analysis itself are slightly different so that minor differences in the performance of the selection algorithm can be expected.

For each selected tau event, the decay mode of each hemisphere is determined independently. As these are all single prong decay modes, a single charged track in the hemisphere is an initial requirement common to all four selection criteria. In addition, the single charged track must have been produced within a fiducial tracking volume of $|\cos\theta| < 0.74$. This number is somewhat arbitrary, although it provides a nice clean cutoff just before the tracking efficiency falls steeply. The identification criteria are then sequentially applied to perform an exclusive classification, meaning that each hemisphere will at most be identified as only one of the four possible decay channels.

Muon Decays

The SLD reconstruction package provides some amount of muon identification for all observed tracks by means of an integer status word `MUSTAT`. Based primarily on the matching of the CDC track to observed hits in the WIC, the `MUSTAT` selection alone does a very good job for tracks produced within the barrel WIC coverage of $|\cos\theta| < 0.62$. For these hemispheres, the following selection criteria are sufficient:

- `MUSTAT = 0` or `MUSTAT = 2`;

- Measured track momentum $p_0 > 1$ GeV/c.

For tracks produced in the region between $0.62 < |\cos\theta| < 0.74$, the muon identification must rely upon the observed energy deposition in the LAC. For this region, the following selection criteria are used to identify muon decays:

- Energy to momentum ratio $E/p_0 < 0.3$;

- Number of associated EM LAC towers hit $N_{tow} < 4$;

- No unassociated neutral clusters are within the jet cone;

- Pseudo mass < 180 MeV/c^2;

- $p_0 > 2$ GeV/c.

The E/p_0 ratio is the deposited KAL energy of the associated cluster, calculated according to the MIP energy scale, divided by the measured track momentum. The pseudo mass is the invariant mass of the track and its associated cluster assuming that the track is a pion and the associated cluster is a photon which has been incorrectly associated with the track.

The muon selection is estimated by Monte Carlo data to have an absolute efficiency of 42% with a total purity of 93%. This selection efficiency includes all tau selection and geometrical efficiency factors, while the background is evenly split between mis-identified tau decays (mostly pions) and non-tau background from dimuon production.

Electron Decays

The SLD reconstruction package also provides an integer status word ESTAT to identify electrons. Based primarily on the E/p_0 ratio as well as the shower shape in the LAC, the ESTAT selection was primarily designed to identify electrons with high efficiency in hadronic jets. In the sparsely populated tau events, the ESTAT selection is fairly loose, and additional cuts are applied to clean up the selected events. The following criteria are then used to select electron decays:

- ESTAT < 4 or CRID likelihood difference $\mathcal{L}(e) - \mathcal{L}(\pi) > 20$;

- No energy deposited in outermost LAC layer HAD2;

- Number of EM LAC towers hit $3 < \mathrm{N}_{tow} < 25$;

- No unassociated clusters with Pseudo mass < 500 MeV/c^2, or
  1 or 2 unassociated clusters with Jet mass < 500 MeV/c^2;

- $p_0 > 1$ GeV/c.

This selection is estimated to be 34% efficient with a purity of 97%. The primary background comes from hadronic tau decays (1.6%), as well as the other physics processes with real electrons in the final state which pass the tau selection like wide angle Bhabhas (0.5%) and two photon events (0.5%).

Pion Decays

After the muon and electron hemispheres have been identified, the more difficult task of selecting the hadronic tau decays is attempted. Even though the efficiency for identifying the fully leptonic decays from the sample of selected tau events is around 70%, there is still a substantial amount of electron and muon background present to separate from the pion channel. Hemispheres which pass the following criteria are then classified as pion decays:

- `MUSTAT` $\neq 0$ and `MUSTAT` $\neq 2$;

- `ESTAT` > 2;

- No unassociated clusters within the jet cone;

- $E_{\mathrm{EM}}/p_0 < 0.42$ using LAC EM energy only;

- For $|\cos\theta| < 0.6$, $0.14 < E/p_0 < 0.62$;

- For $|\cos\theta| > 0.6$, $0.31 < E/p_0 < 0.62$;

- Pseudo mass < 300 MeV/c^2;

- $p_0 > 3$ GeV/c.

In addition there is an electron veto so that if $p_0 < 30$ GeV/c and no energy is deposited in HAD2 and the CRID likelihood difference $\mathcal{L}(e) - \mathcal{L}(\pi) > 20$, the hemisphere is not classified as a pion. The total efficiency of the pion selection is 20% with a purity of 81%. The background is almost entirely from the rho channel where the photons from the extra neutral pion have been lost.

Rho Decays

To separate the rho decays from the non-resonant multi-pion background, an attempt is made to fully reconstruct the invariant mass of the underlying rho meson. The gold-plated rho decay will have one track with a pion-like associated cluster, as well as two unassociated clusters from the neutral pion decay to two photons. Often, however, there are either extra clusters found by the clustering algorithm, or some of the real clusters have been merged together. To keep the selection efficiency reasonable, the invariant mass is calculated for all hemispheres with up to four observed neutral clusters, although the algorithm used is different for each topology. For instance, in the gold plated case the two unassociated neutrals are combined to form a neutral pion, which is then combined with the charged track to reconstruct the rho mass. With only one unassociated cluster, however, the two neutral clusters from the neutral pion are assumed to be merged, and the unassociated neutral cluster is combined directly with the momentum of the charged track. The following criteria are then used to select rho decays:

- `MUSTAT` $\neq 0$ and `MUSTAT` $\neq 2$;

- `ESTAT` > 2;

- Total neutral clusters in hemisphere $1 \leq N_{clu} \leq 4$;

- Reconstructed rho mass 440 MeV/c^2 $< m_\rho < 1.2$ GeV/c^2;

- Calorimeter-based event thrust axis $|\cos\theta_{KAL}| < 0.74$;

- $p_0 > 1$ GeV/c.

The rho selection is estimated by the Monte Carlo data to have a total efficiency of 29%, with a purity of 75%.
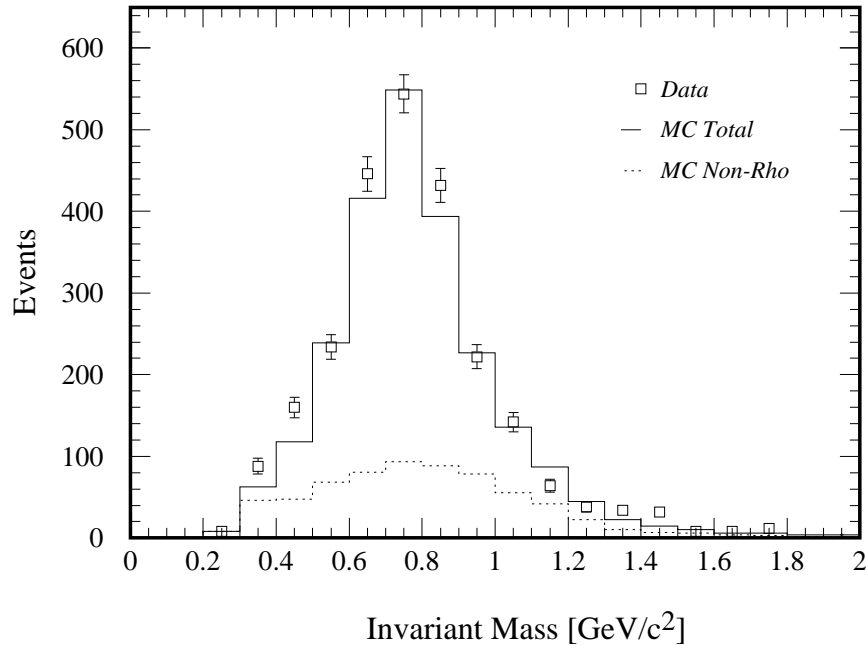
Figure 4-3: The invariant mass distribution is shown for the rho candidate hemispheres. The Monte Carlo prediction is also shown, including the expected background from non-rho tau decays.

Unidentified Decays

The remaining tau decays are classified into inclusive categories according to their track topology. Hemispheres with one or two charged tracks are classified as unidentified one prong or two prong hemispheres respectively. Hemispheres with three charged tracks are required to have a charge sum equal to either $+1$ or -1, and if the invariant mass of the three tracks is greater than 950 MeV/c^2 the hemisphere is classified as an a1 decay, while the remaining are classified as unidentified three prong decays.

There are then a total of eight possible classifications for each hemisphere (e, μ, π, ρ, 1pr, 2pr, 3pr, a1), which encompasses almost all possible tau lepton decay modes.[3] For an event to be useful to this analysis, at least one of the hemispheres

---

[3] The branching fraction for a tau lepton decaying to five charged hadrons has been measured to be under 0.2%.

must be identified as one of the four spin-sensitive tau decay channels, while the other hemisphere must be classified into one of the eight categories listed above.

4.5   Kinematic Tau Reconstruction

To determine the azimuthal decay angle of the observed charged track with respect to the tau production direction, the momenta of the underlying tau pairs must be reconstructed from the visible tracks. The four momentum of the underlying tau (p^μ) can be written in terms of the observed track four momentum (q^μ) and the unobserved missing decay momentum (k^μ) as

$$p^\mu = q^\mu + k^\mu. \tag{4.1}$$

For the two body tau decays like $\tau \to \pi\nu_\tau$, k is nothing more than the momentum of the unobserved neutrino, and $k^2 = 0$ can be used as a constraint. Two other constraints are available from $p^2 = m_\tau^2$ and the assumption that the tau energy is half of the collision energy. When combined with the four measured components of q, there is only one free parameter left per hemisphere.

The remaining free parameter is the azimuthal decay angle (ϕ) of the observed track about the tau which produced it, so that the tau momentum is constrained to lie on a cone of opening angle $\cos\psi = f(k^2, q^0)$ around the observed charged track. A similar cone is defined by the track observed in the opposite hemisphere, and under the assumption that the two taus are produced back-to-back with equal momentum, the intersection of these two cones determines the tau production direction up to a two-fold ambiguity, as illustrated in Figure 4-4. This ambiguity can be resolved by considering the track impact parameters as measured by the vertex detector, although in practice this does not dramatically improve the resolution on the azimuthal decay angle ϕ.
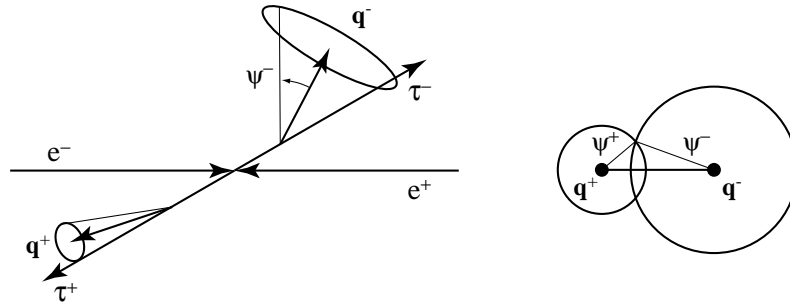
Figure 4-4: The underlying tau momentum vector is reconstructed by considering the decay kinematics of the two observed charged tracks. Each hemisphere constrains the tau momentum vector to lie on a cone of opening angle ψ about the observed charged track. The intersection of the two cones determines the tau momentum up to a two-fold ambiguity, which can be resolved using the precision vertex detector.

For the three body leptonic decay modes where the additional missing neutrino spoils the $k^2 = 0$ constraint, the tau direction can still be reconstructed with somewhat reduced resolution by using the most likely value of k^2 for each particular decay mode as the constraint. If both tau hemispheres decay leptonically, the two cones describing the most likely tau momentum vector will not actually intersect, and so in practice a fit is performed using the predicted Monte Carlo k^2 distribution to provide a likelihood for each hemisphere as a function of tau direction. This likelihood fit technique is, in fact, used with all eight hemisphere categories so that the underlying tau direction, and hence the azimuthal decay angle ϕ, can be determined for every selected tau event.

As will be more completely discussed in Chapter 5, the resolution on the angle ϕ depends strongly upon the particular decay modes observed, along with the momenta of the tracks involved, but in general the three body decay modes contain nearly as much useful information as the pure two body modes. To improve the ϕ resolution somewhat in those decay modes which are likely to contain neutral pions (ρ, 1pr, 2pr, 3pr), the unassociated neutral clusters are added into the observed hemisphere four momentum q^μ for the purposes of fitting the tau momentum vector.
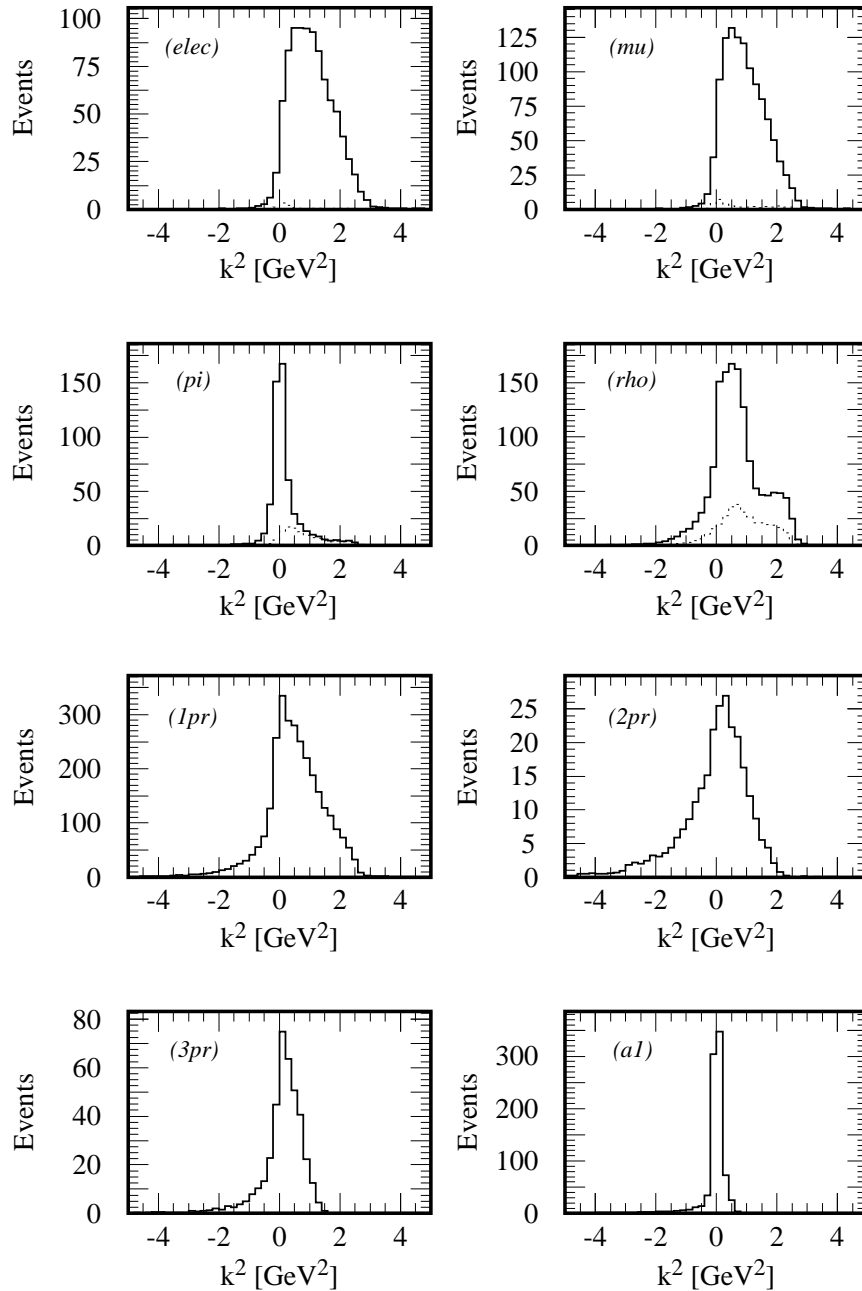
Figure 4-5: The invariant mass of the missing momentum vector (k^2) is shown for each of the eight hemisphere categories as predicted by the Monte Carlo data. These distributions are used to perform a likelihood fit for the unobserved tau production momentum so that the azimuthal decay angle ϕ can be calculated for each identified hemisphere.

Table 4.2: Selected Events by Identified Decay Topology

	e	μ	π	ρ	*1pr*	*2pr*	*3pr*	*a1*
e	43	135	60	163	224	25	38	96
μ		87	58	225	308	28	49	133
π			15	83	118	16	24	50
ρ				120	425	47	58	158

4.6   Event Selection Summary

The assignment of which hemisphere contains the τ^+ or τ^- lepton is made based on the charge of the observed decay products. The 2pr hemispheres are assumed to have the opposite charge of the opposing identified hemisphere, but of the remaining events, only 1.0% have the same charge reconstructed in both hemispheres. These events are removed from the selected data sample, and assuming that the probability of mis-identifying the charge is uncorrelated between the two hemispheres, one would expect 0.01% of the remaining events to have the charge in both hemispheres mis-identified. This amounts to less than 0.3 events in the selected data sample, and it is assumed that the remaining events have their charge correctly reconstructed.

One final selection cut which is applied to ensure that the event is well contained within the tracking acceptance of the detector is that the reconstructed tau momentum vector must lie within the $|\cos\theta| < 0.74$ fiducial volume. This only removes a handful of events, and the final data sample which is used in this analysis is shown in Table 4.2. The selection efficiency and purity as predicted by the Monte Carlo data in each usable event topology is summarized in Table 4.3 and Table 4.4 respectively. Complete energy dependent efficiency and background distributions which are necessary to properly calculate the likelihood of each observed event will be presented in the next chapter.

Table 4.3: Monte Carlo Efficiency Estimate by Identified Decay Topology

	e	μ	π	ρ	any
e	23.4%	28.2%	14.4%	19.9%	34.2%
μ		32.4%	17.1%	25.1%	41.7%
π			7.9%	11.3%	20.0%
ρ				16.0%	28.8%

Table 4.4: Monte Carlo Purity Estimate by Identified Decay Topology

	e	μ	π	ρ	$other$
e	94.2%	94.9%	82.0%	75.6%	96.7%
μ		77.7%	79.1%	73.5%	95.4%
π			68.1%	61.3%	79.5%
ρ				55.0%	74.9%

For topologies where both hemispheres are identified, the purity gives the percentage of events where both identifications are correct. For the remaining topologies, the purity gives the percentage of events where the (e, μ, π, ρ) hemisphere has been identified correctly.
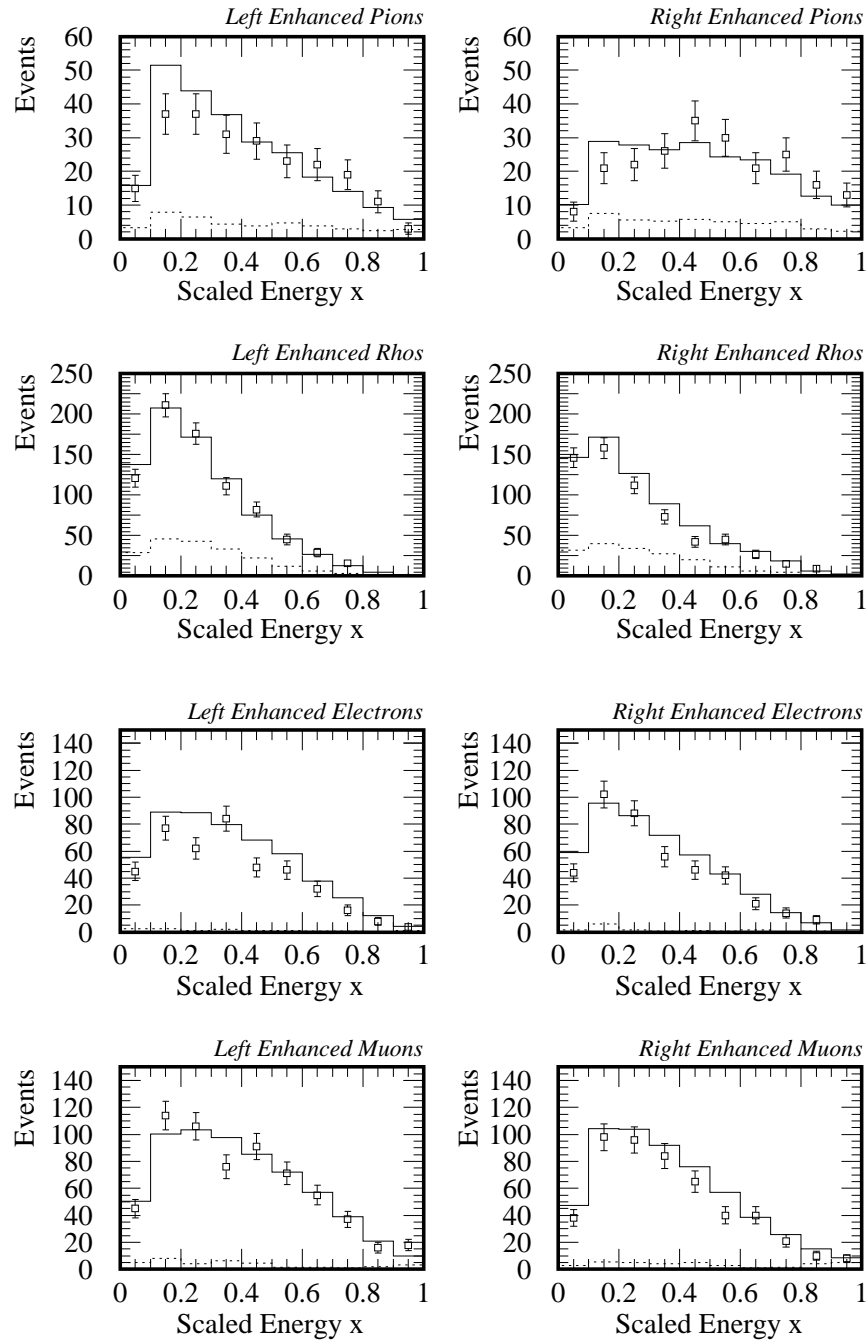
Figure 4-6: The observed scaled energy distributions are shown for the identified leptonic and hadronic decay modes. These data samples have been separated into left and right longitudinally polarized tau samples by combining decays from forward left-handed events ($\cos\theta > 0, \mathcal{P}_e < 0$) with decays from backwards right-handed events ($\cos\theta < 0, \mathcal{P}_e > 0$), and vice versa. The expected Monte Carlo distributions show good agreement with the data, and the underlying background is also shown.

Chapter 5

Likelihood Function

Each selected and identified tau decay provides useful information which can be used in the likelihood fit for the anomalous couplings of interest. In principle, the observed track four vectors could be plugged into the partial differential cross section to give an event probability as a function of the anomalous dipole moments. In practice, however, there are a number of experimental issues like the background from mis-identified tau decays and the imperfect tracking resolution which all must be properly accounted for. This chapter describes the various corrections and approximations which must be applied to the theoretical likelihood function to obtain an accurate fit result.

5.1   Likelihood Formalism

The theoretical likelihood function has been introduced in Chapter 1 as the product of the normalized production spin density matrix and the tau decay matrices,

$$
\mathcal{L}(d_\tau, \tilde{d}_\tau \,|\, \cos\theta, \mathcal{P}_e, x^+, \phi^+, x^-, \phi^-) =
$$
$$
\tilde{\chi}^{\alpha'\alpha\beta'\beta}(d_\tau, \tilde{d}_\tau \,|\, \cos\theta, \mathcal{P}_e)\; \mathcal{D}^{\alpha'\alpha}(x^+, \phi^+)\; \mathcal{D}^{\beta'\beta}(x^-, \phi^-), \quad (5.1)
$$

where the normalized production spin density matrix is given by

$$\tilde{\chi}^{\alpha'\alpha\beta'\beta} = \chi^{\alpha'\alpha\beta'\beta}/(\chi^{\alpha'\alpha\beta'\beta}\delta_{\alpha'\alpha}\delta_{\beta'\beta}), \tag{5.2}$$

such that the likelihood of each event is normalized over the phase space of all possible decay parameters $(x^+, x^-, \phi^+, \phi^-)$:

$$\int \mathcal{L}(d_\tau, \tilde{d}_\tau | \cos\theta, \mathcal{P}_e, x^+, \phi^+, x^-, \phi^-) \, dx^+ d\phi^+ dx^- d\phi^- = 1. \tag{5.3}$$

The two experimentally available observables in each hemisphere are the scaled energy of the observed decay product x and the azimuthal decay angle of the observed track with respect to the tau production plane ϕ. As there is some amount of measurement uncertainty present in each of these observables, the base likelihood function must be convoluted with a resolution function to take into account the possible 'true' values (x_0, ϕ_0) given the measured values (x, ϕ). In addition, there is some amount of mis-identified tau and non-tau background present in each identified decay topology which must also be accounted for.

Formally, the likelihood for each event observed in the decay topology (ij) is given by

$$\mathcal{L}_{ij} = \int \tilde{\chi}(d_\tau, \tilde{d}_\tau | \cos\theta, \mathcal{P}_e) \, \mathcal{D}_i(x_0^+, \phi_0^+) \, \mathcal{D}_j(x_0^-, \phi_0^-) \times$$

$$\mathcal{R}_{ij}(x^+, x^-, \phi^+, \phi^-, x_0^+, x_0^-, \phi_0^+, \phi_0^-) \, dx_0^+ dx_0^- d\phi_0^+ d\phi_0^- + Background \tag{5.4}$$

where $\mathcal{R}$ is a resolution function describing the probability that an event produced with the 'true' values $(x_0^+, x_0^-, \phi_0^+, \phi_0^-)$ is observed with the measured values $(x^+, x^-, \phi^+, \phi^-)$.[1]

---

[1] In principle the production angle $\cos\theta$ should also be a part of this resolution function, although in practice as long as the anomalous coupling terms are near zero the resolution on $\cos\theta$ can be safely neglected.

Clearly there are a number of problems with implementing the resolution function in this formal fashion as it would require performing a four dimensional integral over an eight dimensional resolution function. Even if the integration could be numerically performed, calculating the resolution function, which will be different for every observed decay topology, is nearly impossible even with the benefit of a Monte Carlo simulation. Rather, a number of simplifying assumptions must be applied to reduce this formal integration to a more tractable number of parameters.

The actual likelihood for an observed event is calculated in this analysis as the product of each hemisphere likelihood, given by

$$
\mathcal{L}_i = \int \tilde{\chi}^{\alpha'\alpha\beta'\beta}(d_\tau, \tilde{d}_\tau \,|\cos\theta, \mathcal{P}_e)\, \mathcal{D}_i^{\alpha'\alpha}(x_0^+, \phi_0^+)\, \delta_{\beta'\beta} \times
$$
$$
\mathcal{R}_i(x^+, x_0^+)\, \mathcal{R}_i(\phi^+, \phi_0^+)\, \mathcal{E}_i(x_0^+)\, dx_0^+ d\phi_0^+ \quad (5.5)
$$

for the τ^+ hemispheres, and similarly for the τ^- hemispheres. The resolution function has been factored into two normalized resolution functions for x and ϕ separately, as well as an overall efficiency function $(\mathcal{E})$ which describes the probability that a given 'true' event will actually pass the tau selection criteria. The motivation for and consequences of this particular likelihood function will be discussed throughout the remainder of this chapter. The correction for background contamination will be discussed in Section 5.6.

5.2   Scaled Energy Resolution

The first simplification applied in Equation 5.5 is the assumption that the resolution on the scaled energy x is a purely instrumental effect arising from the ability of the SLD tracking system to measure the observed track momentum. Each track in an event will then have an individual resolution function $\mathcal{R}_i(x, x_0)$ which depends only upon the particular species (i) of the track measured, and is independent of all other

event parameters. In principle, this tracking resolution can vary as function of the track production angle $\cos\theta$, although within the fiducial volume which has been defined for this analysis the observed tracking resolution is quite uniform.

This resolution function is then a two dimensional function describing the probability that a track of scaled energy x_0 will be reconstructed with scaled energy x. This resolution function is normalized according to

$$\int \mathcal{R}(x, x_0) \, dx = 1, \tag{5.6}$$

so that there is unit probability of detecting each true scaled energy value x_0. The energy-dependent selection efficiency is handled by a separate efficiency function $\mathcal{E}$.

The resolution function for each identified tau decay mode can be estimated directly from the Monte Carlo data where both the true generated x_0 and observed x are known. It is well known that the momentum resolution of a drift chamber depends strongly upon the momentum of the track involved, and a particularly convenient parameterization can be written in terms of the inverse momentum as

$$\sigma_{1/p}^2 = a^2 + b^2/p^2. \tag{5.7}$$

As the scaled energy x is nothing more than the track momentum (up to a small mass correction) divided by half of the collision energy, the resolution on $1/x$ should also follow this simple parameterization.

To calculate the energy resolution, a two dimensional distribution of the Monte Carlo data is made as a function of the true generated energy ($u = x_0$) and the relative residual given by

$$v = (x^{-1} - x_0^{-1})/(x_0^{-1}) = (x_0/x - 1). \tag{5.8}$$

This distribution is then normalized to unity in every bin of x_0, and fit to the
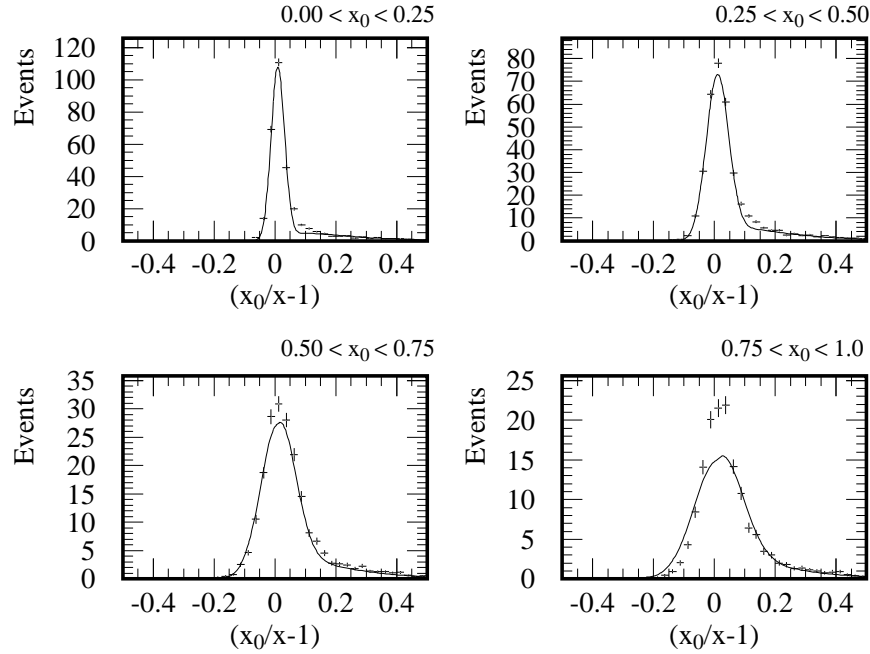
Figure 5-1: The resolution on the electron scaled energy x_0 is shown in four different ranges of the scaled energy. A single six parameter fit is performed to the two dimensional resolution function, which is shown as the solid curve. The Monte Carlo data which has been used in the fit is shown in each scaled energy range as the crosses. Except for in the highest scaled energy range, the fit gives a very good description of the Monte Carlo data. The measured momentum resolution for real tracks is somewhat worse than the Monte Carlo prediction.

function

$$f(u, v) = 1/\sqrt{2\pi\sigma^2} \exp\left[-\frac{(v - c_3)^2}{2\sigma^2}\right], \tag{5.9}$$

where

$$\sigma^2 = c_1^2 u^2 + c_2^2, \tag{5.10}$$

and c_i are the parameters which are being fit for. This three parameter fit does a very good job describing the distribution predicted by the Monte Carlo for the muon, pion, and rho hemispheres.

Table 5.1: Scaled Energy Resolution Parameters

	e	μ	π	ρ
c_1	.085	.083	.080	.087
c_2	.018	.017	.017	.017
c_3	.010	.005	.004	.004
c_4	2.3	-	-	-
c_5	6.3	-	-	-
χ^2/dof	0.98	1.18	0.99	1.16

The energy resolution for electron final states is somewhat more complicated, as the light electrons tend to radiate photons as they traverse the detector, leading to a logarithmic tail in the resolution function. This radiative tail is parameterized in an *ad-hoc* fashion by adding the function

$$c_4 \left[e^{-c_5 v} - e^{-(10+c_5)v} \right],$$
(5.11)

to the function in Equation 5.9 to describe the electron resolution. The results of the resolution parameter fits are shown in Table 5.1.

One valid question is how well the Monte Carlo simulation describes the true tracking resolution seen in the data. An estimate of the resolution parameters in Equation 5.7 has been made by considering the resolution observed in the data for Bhabha and dimuon events. The measured resolution parameters can be converted to values of $c_1 = 0.12$ and $c_2 = 0.010$, which is around 40% worse in the data for the momentum dependent term c_1, while the momentum independent term c_2 is much better. A systematic uncertainty related to this difference is included in the final result.

5.3   Azimuthal Decay Angle Resolution

A significant simplification which is made in Equation 5.5 is to calculate the likelihood for each hemisphere independently. The likelihood function is then obtained from the differential cross section by integrating out all possible decay angles in the opposing hemisphere, and only those hemispheres which have been identified as one of the four spin sensitive decay modes will then contribute to the overall result. There are many advantages to handling the data in this fashion with only a few obvious disadvantages.

The first disadvantage is a loss of statistical precision which comes from ignoring the correlation terms in the transverse polarization cross sections. In contrast to the Standard Model longitudinal polarization correlation which is nearly 100%, the transverse polarization correlations which are described by the χ^{+--+} and χ^{-++-} matrix elements in Table A.3 are proportional to $|d|^2$ and hence quite small.

The second disadvantage to treating each hemisphere independently is that for the events where both tau decays are identified and used in the analysis, the information being provided will be treated by the likelihood fit as being statistically independent, which is not strictly true. The amount of statistical correlation between the hemispheres, as already argued in the previous paragraph, is quite small and will have an insignificant effect on the outcome.

This is certainly not true if an attempt is made to measure the longitudinal polarization of the produced tau leptons, as here the statistical correlations are nearly 100%. Since almost all of the useful information on the anomalous dipole moments comes from the uncorrelated transverse polarization terms, where the dependence is first order in d, and not the correlated terms, where the dependence is second order in d, any resulting statistical correlation is very small and can be safely ignored.

Meanwhile, there are tremendous advantages to be gained by treating the two hemispheres independently. The single most important advantage comes from be-
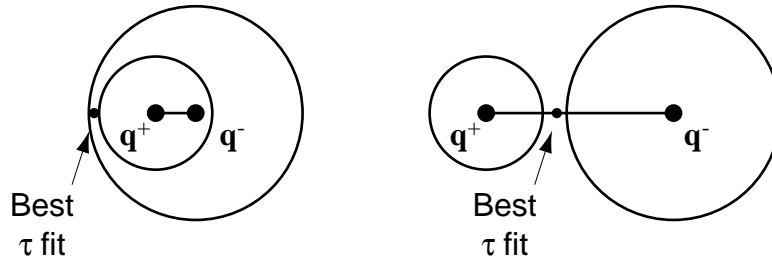
Figure 5-2: Two examples which lead to decay angle correlations are shown. In both cases the most likely probability cones from the kinematic tau fit algorithm do not intersect. The most likely tau momentum vector is then found to be in the plane which contains the two observed tracks, leading to an unphysical correlation in the quantity $|\phi^+ - \phi^-|$.

ing able to avoid the large unphysical correlations between the two reconstructed azimuthal decay angles (ϕ^+, ϕ^-) which result from the kinematic fit used to reconstruct the underlying tau production vector. Since the tau pairs are assumed to be produced back-to-back, any error made in one hemisphere is going to be directly correlated with the error made in the other hemisphere. In addition, if one or both hemispheres have additional missing momentum, as is the case with the fully leptonic decays, the two cones of most likely tau momentum used in the kinematic fit will not necessarily intersect. The kinematic fit will then find the most likely tau momentum vector to lie in the plane which contains both observed decay momenta, and the quantity $|\phi^+ - \phi^-|$ will then tend to pile up at the values of 0 and π. Note that as long as the decay angle in the opposing hemisphere is integrated out, and the correlated physics information contained in the two hemispheres is small, these non-physical correlations in the measured values of ϕ are irrelevant.

By treating each hemisphere independently, the remaining resolution function simply describes the probability of observing a given decay angle ϕ independently from the angle measured in the opposing hemisphere. As might be expected, the resolution on ϕ depends entirely on how well the underlying tau momentum vector is reconstructed, and there are a number of factors which contribute to this accuracy.

The first factor is the topology of the event. Clearly a $\tau^+\tau^- \to \pi^+\pi^- X$ event

will be more accurately reconstructed than a fully leptonic $\tau^+\tau^- \rightarrow e^+e^-X$ event due to the additional missing momentum present in the leptonic decay. To keep the number of independent parameterizations reasonable, the topology of the opposing hemisphere is broken down into two categories: those hemispheres with extra missing momentum $(e, \mu, \rho, 1\mathrm{pr}, 2\mathrm{pr})$, and those hemispheres which are most likely 2 body decays $(\pi, 3\mathrm{pr}, \mathrm{a}1)$. The ϕ resolution is then parameterized separately for each of the four identified decay types for the two possible opposite hemisphere categories.

The second factor is the observed momenta of the two hemispheres which were used in the kinematic tau fit. Clearly if the observed hemisphere has a very low momentum track, while the opposing hemisphere has a very stiff track, there is a very large lever arm available from the opposing hemisphere to determine the tau direction and the error on ϕ will be small. Conversely, if the observed hemisphere has a very high momentum track, the opening angle between the tau and the observed track must be very small and the error on ϕ will be large.

Since the resolution of the kinematic tau fit is dominated by the real physics effect of the missing neutrino momentum, and is only secondarily effected by the tracking resolution, the parameterization of the ϕ resolution is explicitly written as a function of the measured scaled energy (x^+, x^-), and not the true scaled energy which would need to be integrated over in the likelihood function. Even so, this still leaves a three dimensional resolution function $\mathcal{R}(\phi - \phi_0, x, x_{\mathrm{other}})$, where x is the scaled energy of the identified hemisphere and x_{other} is the scaled energy of the track in the opposing hemisphere. Rather than try to deal with a three dimensional function, which is difficult to parameterize and even more difficult to visualize, the single parameter $(x - x_{\mathrm{other}})$ is used to reduce this to a more tractable two dimensional function. This one particular parameter was found to qualitatively have a larger effect on the ϕ resolution than any other linear combination of x and x_{other}.

This resolution function is then estimated from the Monte Carlo data in a similar manner as the scaled energy resolution. A two dimensional distribution is formed

from the ϕ residual $v = \phi - \phi_0$ as a function of the scaled energy difference between the two hemispheres $u = x - x_{\text{other}}$. Without any physically motivated parameterization to use as a guide, this distribution is fit to two Gaussian terms plus a constant term,

$$f(u, v) = (1 - n_2 - n_3)/\sqrt{2\pi\sigma_1^2} \exp\left[-\frac{v^2}{2\sigma_1^2}\right] +$$
$$n_2/\sqrt{2\pi\sigma_2^2} \exp\left[-\frac{v^2}{2\sigma_2^2}\right] + n_3/(2\pi), \quad (5.12)$$

where the widths and fractions of the various terms are simple polynomial functions of u:

$$\sigma_1 = c_1 + c_2 u \tag{5.13}$$

$$n_2 = c_3 + c_4 u \tag{5.14}$$

$$\sigma_2 = c_5 + c_6 u \tag{5.15}$$

$$n_3 = c_7(u + 1) + c_8(u + 1)^2. \tag{5.16}$$

Even though this parameterization is strictly phenomenological, using a simple linear dependence for the gaussian widths in Equation 5.12, this eight parameter fit does a good job describing the predicted Monte Carlo resolution functions for the eight possible hemisphere topologies.

As can be seen in Figure 5-3, the ϕ resolution is quite good for negative values of $x - x_{\text{other}}$, and degrades quickly as this value increases. The eight parameterizations used in this analysis are shown in Table 5.2.

5.4   Detection Efficiency

As shown in Equation 5.6, the resolution functions described in this chapter are normalized to unit probability so that every produced hemisphere has unit proba-
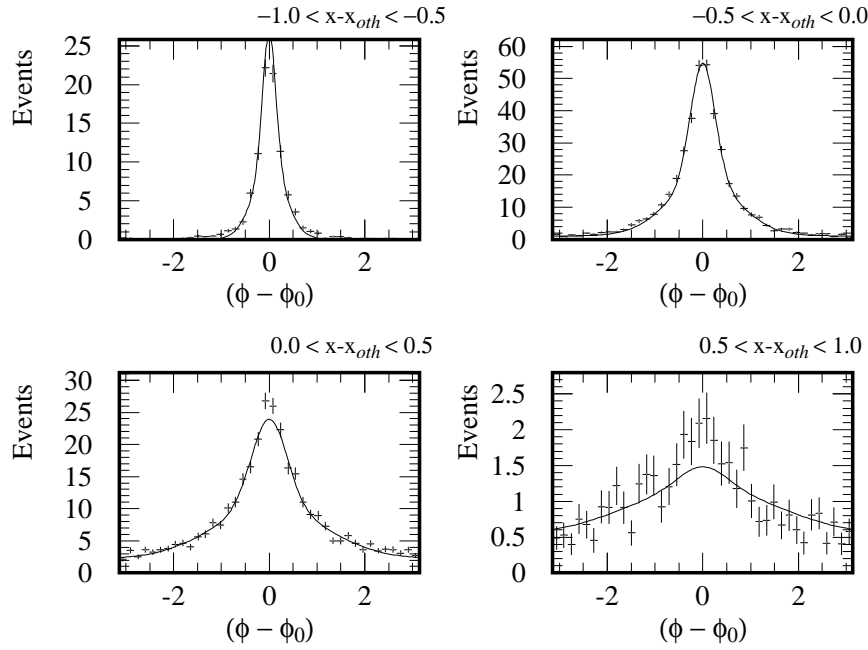
Figure 5-3: The azimuthal decay angle resolution is shown for identified rho events with additional missing momentum in the opposing hemisphere. The eight parameter fit, shown as the solid curve, describes the Monte Carlo data well in all four ranges of the value $x - x_{\text{other}}$. As expected, the resolution gets much worse as this value becomes large, although the expected number of events in this range is small.

bility when integrated over all possible detected values. It is clear, however, that the probability of a hemisphere being selected and properly identified is not uniform as a function of the true, produced event parameters. In principle, the efficiency of selecting a given hemisphere is a function of both the scaled energy and the azimuthal decay angle at production. In practice, the efficiency dependence on ϕ_0 is uniform and the efficiency is strictly written as a function of the scaled energy x_0.[2]

The efficiency function $\mathcal{E}_i(x_0)$ is parameterized separately for each identified tau decay mode i, where the efficiency includes both the probability of selecting the given event as well as the probability of properly identifying decay mode of the given hemisphere. The performance of the particle identification algorithm described in

---

[2] Possible ϕ_0 efficiency effects will be discussed in Chapter 6 as a systematic uncertainty.

Table 5.2: Azimuthal Decay Angle Resolution Parameters

	e-no	e-$miss$	μ-no	μ-$miss$	π-no	π-$miss$	ρ-no	ρ-$miss$
c_1	.31	.32	.23	.34	.13	.32	.23	.33
c_2	.20	.21	.02	.18	-.10	.21	.15	.14
c_3	.39	.59	.56	.61	.33	.55	.46	.51
c_4	-.10	.18	-.02	.09	-.20	-.06	-.05	.28
c_5	.97	1.15	.89	1.14	.73	.93	.79	1.13
c_6	1.19	1.47	1.10	1.59	1.03	1.51	.66	1.39
c_7	.06	.02	.14	.03	.27	-.07	.14	.14
c_8	.19	.11	.07	.10	.14	.16	.09	-.01
χ^2/dof	1.1	1.3	1.0	1.2	0.8	1.1	1.0	1.1

The azimuthal decay angle resolution function is parameterized separately for the four identified decay modes and the missing momentum characteristics of the opposing hemisphere.

Chapter 4 is quite uniform across the barrel part of the SLD detector, but degrades somewhat for production angles beyond $|\cos\theta| > 0.6$. This is primarily due to the loss of useful information from the WIC to perform muon identification, although the LAC also has some problems in this region due to the overlap between the barrel and endcap modules. To properly account for this difference in the particle identification performance, the efficiency function is parameterized separately for tracks found in the barrel region ($|\cos\theta| < 0.6$) and the endcap region ($0.6 < |\cos\theta| < 0.74$).[3]

Further discussion of the efficiency function $\mathcal{E}_i(x_0)$ will be covered in Section 5.6 after the techniques for handling the background contamination have been presented.

5.5   Effective Decay Matrices

The convolution of the theoretical likelihood function over the resolution probability functions described by Equation 5.5 is only dependent upon the observed decay

---

[3] This is more properly termed the *overlap* region, as it is really where the barrel and endcap LAC modules share the shower information, although the term *endcap* will be used.

properties of the identified hemisphere. This convolution can be re-written in terms of the effective decay matrix $\tilde{\mathcal{D}}(x, \phi)$ as

$$\tilde{\mathcal{D}}_i^{\alpha' \alpha}(x, \phi) = \int \mathcal{D}_i^{\alpha' \alpha}(x_0, \phi_0) \; \mathcal{R}_i(x, x_0) \; \mathcal{R}_i(\phi, \phi_0) \; \mathcal{E}_i(x_0) \; dx_0 d\phi_0, \qquad (5.17)$$

where the effective decay matrix for the τ^+ and τ^- hemispheres differ only by the theoretical decay matrix $\mathcal{D}_i(x_0, \phi_0)$ used.

This theoretical decay matrix $\mathcal{D}_i(x_0, \phi_0)$ is developed in Appendix A for the four identified spin-sensitive decays used in this analysis. The great advantage of factoring the likelihood function in this manner is that these resolution integrals only need to be performed once as the effective decay matrices for each observed hemisphere are completely independent of the anomalous couplings which are being iterated over in the likelihood fit. In addition, since only the off-diagonal elements of the decay spin density matrix are functions of both ϕ_0 and x_0, the two dimensional integral written in Equation 5.17 only needs to be performed once for each identified hemisphere. The diagonal matrix elements need to be integrated over x_0 only.

5.6   Backgrounds

Since the tau selection and hemisphere identification algorithms are not perfect, there is some background present in the selected event sample. This background can be classified into three distinct sources which are handled differently in calculating the likelihood for any given identified hemisphere:

- Mis-identified spin-sensitive tau decay modes;

- Other mis-identified tau decay modes;

- Background from non-tau sources.

Each identified hemisphere has some possible background contamination from each of these sources. It is important to treat the mis-identified spin-sensitive tau decay modes separately, as the spin information which they contain will affect the likelihood function differently than the remaining, spin-insensitive background sources.

All sources of background can be accommodated into the likelihood formalism by expanding the effective decay matrix of Equation 5.17 so that it describes a weighted sum of the expected components in each identified decay channel. For each hemisphere identified in channel i, the complete effective decay matrix is then given by

$$\tilde{\mathcal{D}}_i(x, \phi) = \sum_j w_j \tilde{\mathcal{D}}_{ij}(x, \phi), \tag{5.18}$$

where the index j runs over the four identified tau hemisphere types, the background from the other tau decay modes, as well as the non-tau background sources.

Spin-Sensitive Tau Background

For the mis-identified spin-sensitive tau decay modes, the decay matrix is now written in terms of both the identified decay type i and the produced decay type j as

$$\tilde{\mathcal{D}}_{ij}(x, \phi) = \int \mathcal{D}_j(x_0, \phi_0) \, \mathcal{R}_j(x, x_0) \, \mathcal{R}_j(\phi, \phi_0) \, \mathcal{E}_{ij}(x_0) \, dx_0 d\phi_0, \tag{5.19}$$

which is identical to Equation 5.17 except that now the efficiency function is written in terms of both i and j. This efficiency function $\mathcal{E}_{ij}(x_0)$, which is defined as the probability that a hemisphere of type j is reconstructed and identified as a hemisphere of type i, already provides some weighting to account for the mis-id rate, while the additional weighting factor w_j simply provides the branching fraction for tau events which decay into channel j.
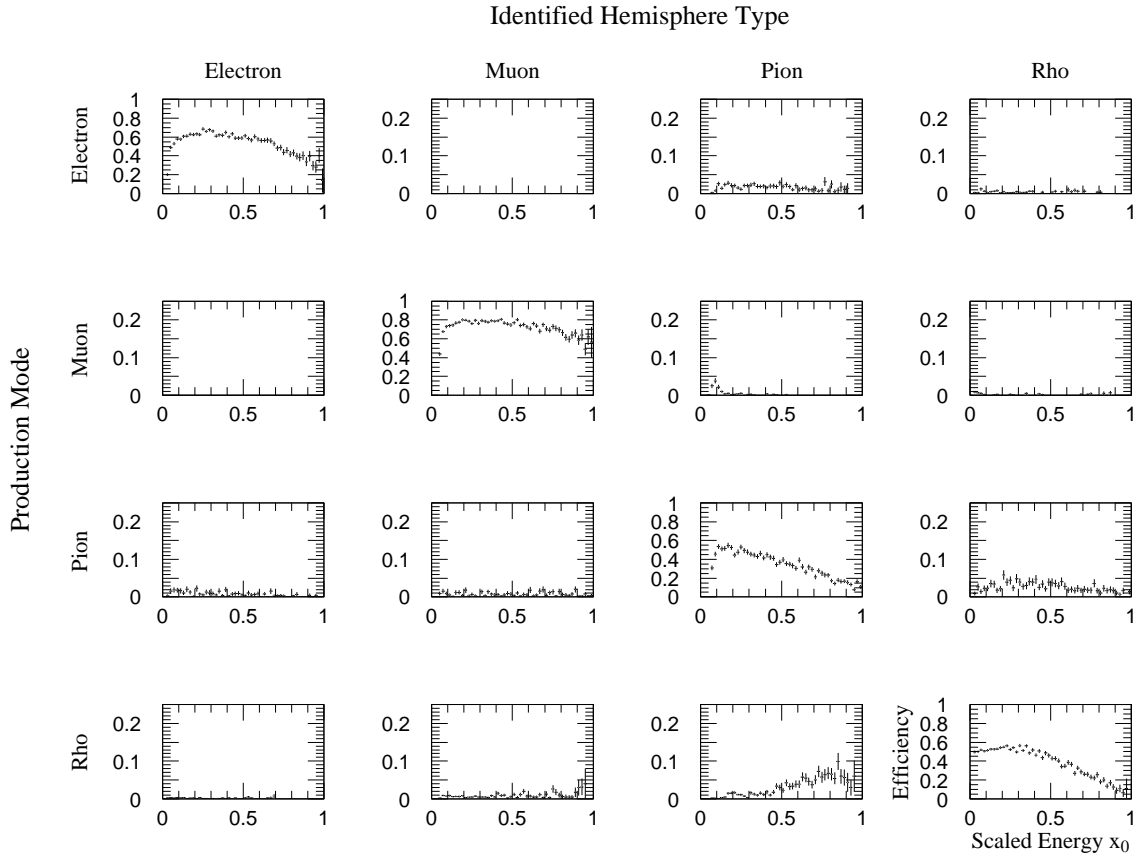
Figure 5-4: The efficiency function $\mathcal{E}_{ij}(x_0)$ is shown as a function of the true scaled energy x_0 for events produced in the barrel region. The efficiency shown here is normalized to the total number of tau decays of each type produced into the fiducial region $|\cos\theta| < 0.6$.

The efficiency function is now a four by four matrix of energy dependent identification efficiencies where the diagonal elements $(i = j)$ describe the correct identification rate, while the off-diagonal elements $(i \neq j)$ describe the mis-identification rate. As mentioned in Section 5.4, these efficiency functions are parameterized separately for the barrel and endcap detector regions. Figure 5-4 shows the efficiency as a function of true scaled energy for the barrel region. The diagonal elements are fit to fourth order polynomial functions, while the off-diagonal elements are either fit to simple linear functions or fourth order polynomials depending upon the complexity of the observed energy dependence.
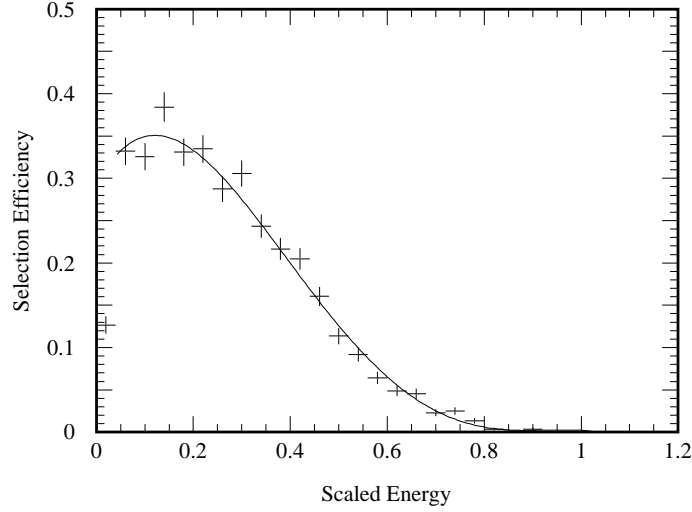
Figure 5-5: The efficiency function for mis-identifying a multi-hadron tau decay mode as a rho decay $\mathcal{E}_\rho^{other}(x)$ is shown as a function of scaled energy for hemispheres in the barrel region. This efficiency function is normalized to the total number of these background decays produced into the barrel region.

Other Tau Background

For the remaining mis-identified tau decays, the momentum of the observed, mis-identified single charged track is assumed to be independent of the underlying tau spin.[4] The effective decay matrix can then be written as

$$\tilde{\mathcal{D}}_{ij}^{\alpha'\alpha}(x,\phi) = \mathcal{E}_i^{other}(x)\delta_{\alpha'\alpha}, \tag{5.20}$$

where the weighting factor w_j in Equation 5.18 is again the branching fraction for tau events to this particular decay mode. In this case, w_{other} is the remaining branching fraction after the (e, μ, π, ρ) modes have been removed.

Since it is assumed that there is no spin information present in these other mis-identified tau decay modes, there is no need to integrate over the spin density matrix, and the effect of this background is merely to dilute the overall spin dependence of

---

[4] The residual spin dependence in these decay modes can be estimated by considering the longitudinal spin dependence as predicted by KORALZ. There is some small spin dependence seen in this background from the single prong a1 decays, although the analyzing power is very small.

the hemisphere by adding in a spin-independent component characterized by the unit decay matrix. The largest background of this sort is from multi-hadron final states to the identified rho channel. The energy dependent efficiency function for this background mode is shown in Figure 5-5, and again a multi-order polynomial is used to parameterize the observed energy dependence.

Non-Tau Background

The background contribution from non-tau sources, which clearly has no spin dependence, is also treated as a constant dilution of the effective spin density matrix. The energy dependence predicted by the Monte Carlo data samples of non-tau background is quite flat in x, and no attempt has been made to model the energy dependence of this background. As the non-tau background is correlated with the overall identified event topology, this background dilution is applied on the basis of the classifications made in both event hemispheres. The background from muon pairs, for instance, is only seen when both hemispheres are identified in the $\tau \rightarrow \mu \bar{\nu}_\mu \nu_\tau$ decay mode.

For this background source, the effective decay matrix is then nothing more than the unit matrix,

$$\tilde{\mathcal{D}}_{ij}^{\alpha'\alpha}(x, \phi) = \delta_{\alpha'\alpha}, \tag{5.21}$$

while the weighting factor $w_{non-tau}$ gives the expected number of identified non-tau background events in that particular decay mode for every generated tau event.

5.7   Likelihood Function Summary

Every hemisphere which is identified in one of the four spin sensitive decay modes is used in this analysis to provide a likelihood for observing that particular event as a

function of the anomalous coupling strengths. The effects of instrumental resolution on the observed hemisphere parameters (x, ϕ) and contamination from all known background sources are incorporated into the effective decay matrix $\tilde{\mathcal{D}}(x, \phi)$ which is computed for each identified hemisphere before the likelihood fit is performed. This effective decay matrix is the weighted sum of the individual decay matrices for each physics process expected to be present in a given identified channel as predicted by the Monte Carlo data.

Each identified τ^+ and τ^- hemisphere then contributes a likelihood given by

$$\mathcal{L}_i^+ = \tilde{\chi}^{\alpha'\alpha\beta'\beta}(d_\tau, \tilde{d}_\tau | \cos\theta, \mathcal{P}_e) \, \tilde{\mathcal{D}}_i^{\alpha'\alpha}(x^+, \phi^+) \, \delta_{\beta'\beta} \tag{5.22}$$

$$\mathcal{L}_i^- = \tilde{\chi}^{\alpha'\alpha\beta'\beta}(d_\tau, \tilde{d}_\tau | \cos\theta, \mathcal{P}_e) \, \tilde{\mathcal{D}}_i^{\beta'\beta}(x^-, \phi^-) \, \delta_{\alpha'\alpha} \tag{5.23}$$

such that the total likelihood function given by

$$\mathcal{F}(d_\tau, \tilde{d}_\tau) \equiv -2 \sum_i \log \mathcal{L}_i \tag{5.24}$$

can be minimized to find the most likely value of the anomalous dipole coupling parameters. The actual fit results and a discussion of the interpretation of the errors on the fit values will be covered in Chapter 6.

Results and Conclusions

Every selected and identified tau decay hemisphere is used in this analysis to provide a likelihood based on the observed charged track momentum as a function of the additional anomalous dipole couplings. This chapter will present the results of this likelihood fit, as well as discuss a number of the systematic uncertainties associated with this sort of analysis. Finally, the results of this analysis are presented along with a number of other measurements of these dipole couplings performed by other collaborations around the world.

6.1 Likelihood Fit Results

Each identified τ^+ or τ^- hemisphere contributes to the total likelihood function a factor given by

$$\mathcal{L}_i^+ = \tilde{\chi}^{\alpha'\alpha\beta'\beta}(d_\tau, \tilde{d}_\tau | \cos\theta, \mathcal{P}_e) \, \tilde{\mathcal{D}}_i^{\alpha'\alpha}(x^+, \phi^+) \, \delta_{\beta'\beta} \qquad (6.1)$$

$$\mathcal{L}_i^- = \tilde{\chi}^{\alpha'\alpha\beta'\beta}(d_\tau, \tilde{d}_\tau | \cos\theta, \mathcal{P}_e) \, \tilde{\mathcal{D}}_i^{\beta'\beta}(x^-, \phi^-) \, \delta_{\alpha'\alpha}, \qquad (6.2)$$

where $\tilde{\chi}(d_\tau, \tilde{d}_\tau | \cos\theta, \mathcal{P}_e)$ is the normalized production spin density matrix which contains all of the physics related to the $Z \to \tau\tau$ vertex, and $\tilde{\mathcal{D}}(x, \phi)$ is the effective tau decay matrix developed in Chapter 5.

The total likelihood function $\mathcal{F}$ is then defined as

$$\mathcal{F}(d_\tau, \tilde{d}_\tau) \equiv -2 \sum_i \log \mathcal{L}_i \qquad (6.3)$$

such that the values of $(d_\tau, \tilde{d}_\tau)$ which minimize $\mathcal{F}$ are the most likely values for the dipole coupling strengths given the observed data. A factor of 2 is included in the definition of $\mathcal{F}$ so that this function behaves statistically in the same manner as a χ^2 distribution.

The function $\mathcal{F}$ is minimized with the `MINUIT` function minimization utility from CERN, which is widely used in physics for log-likelihood and χ^2 fitting.[56] Along with routines to minimize arbitrary multi-dimensional functions, `MINUIT` also provides the processor `MINOS` to calculate parameter errors taking into account both correlations and non-linearities in the minimized function. The theory on which the `MINOS` error estimation is based can be found in [57].

For a single-parameter fit, the 68% CL ($\pm 1\sigma$) interval is determined as the range of the fit parameter over which the minimized function $\mathcal{F}$ changes by less than one unit ($\Delta\mathcal{F} < 1$). For a multi-parameter fit, as performed in this analysis, `MINOS` reports the error on a single parameter as the range over which ($\Delta\mathcal{F} < 1$), while keeping the other parameters minimized. In a two parameter fit, for example, the errors reported by `MINOS` define a rectangular region which entirely contain the one sigma contour found when both parameters are allowed to vary independently. Because the `MINOS` processor actually traces the change in $\mathcal{F}$ as the fit parameters are varied from their best fit values, the error intervals are not necessarily symmetric about the minima.

The results of the `MINUIT` minimization of the function $\mathcal{F}$ for the observed data
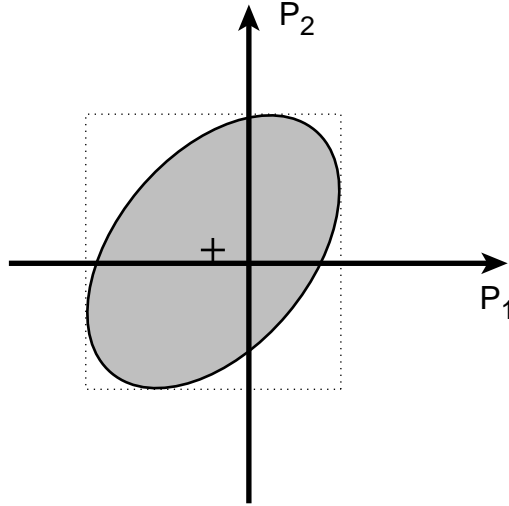
Figure 6-1: The single parameter one sigma errors calculated by `MINOS` bound the contour in the two parameter plane defined by $\Delta\mathcal{F} = 1$. The probability that both parameters simultaneously lie within this one sigma contour is found from a χ^2 table for two degrees of freedom to be 39.3%.

Table 6.1: Anomalous Coupling Fit Results

Parameter	*Fit Value*	ϵ_{lo}	ϵ_{hi}
$\Re(d_\tau)$	0.3	-3.7	+3.7
$\Im(d_\tau)$	-1.9	-2.5	+2.4
$\Re(\tilde{d}_\tau)$	1.0	-4.0	+4.2
$\Im(\tilde{d}_\tau)$	-2.2	-2.5	+2.4

The best fit values for the combined `MINUIT` minimization of the likelihood function $\mathcal{F}(d_\tau, \tilde{d}_\tau)$ is shown along with the limits describing the `MINOS` single parameter 68% confidence interval. All values are in units of 10^{-17} e cm.

Table 6.2: Anomalous Coupling Fit Correlation Matrix

	$\Re(k_v)$	$\Im(k_v)$	$\Re(k_a)$	$\Im(k_a)$	$Global$
$\Re(k_v)$	1.0	-0.04	0.15	0.07	0.171
$\Im(k_v)$		1.0	-0.02	0.19	0.197
$\Re(k_a)$			1.0	0.02	0.149
$\Im(k_a)$				1.0	0.204

The correlation matrix for the `MINUIT` fit is shown. The actual fit parameters used are the dimensionless coupling parameters $k_v = \frac{\sqrt{s}}{g_z} d_\tau$ and $k_a = i \frac{\sqrt{s}}{g_z} \tilde{d}_\tau$.

are shown in Table 6.1, where the errors quoted are the `MINOS` single parameter one sigma limits. Both the real and imaginary parts of both dipole moments are statistically consistent with zero.

6.2   Error Estimation

Given the assumption that the likelihood function $\mathcal{F}$ accurately reflects all aspects of the physical processes being fit, the error estimates for the fit parameters returned by `MINUIT` are valid estimators of the uncertainty on those parameters. With the rather small data sample which is being used in this analysis, the statistical variance on these `MINUIT` determined errors is substantial, and a check that the quoted errors in Table 6.1 are not statistically improbable is desired.

This test is performed by fitting the `KORALZ` generated Monte Carlo data sample, which has roughly twenty times the statistics as the actual observed data, with the same likelihood procedure applied to the data. The Monte Carlo data is evenly divided into twenty MC data sets each of which is fit independently to provide an estimate of the variance in the `MINOS` reported errors. In addition, this test performs a check that the variance on the actual best fit values are accurately described by

Table 6.3: Monte Carlo Based Error Estimation

Parameter	Fit Variance σ_d	Mean Error $\bar{\epsilon}$	Uncertainty $\sigma_{\bar{\epsilon}}$
$\Re(d_\tau)$	3.33	3.90	0.10
$\Im(d_\tau)$	2.46	2.51	0.05
$\Re(\tilde{d}_\tau)$	2.92	4.10	0.10
$\Im(\tilde{d}_\tau)$	2.46	2.31	0.05

By fitting twenty Monte Carlo data samples with equal statistical size as the observed data, the accuracy of the `MINUIT` error estimate can be tested. The actual variance on the observed fit results σ_d agree well with the mean predicted fit error $\bar{\epsilon}$ for the imaginary parts of the dipole moments, although the other two terms appear to have a somewhat narrower variance than predicted by the `MINUIT` error estimate. The fit errors seen in the data agree well with the mean fit errors from the MC samples.

the fit errors.[1]

The results of this test are shown in Table 6.3, and are shown graphically for the CP conserving WMDM in Figure 6-2. While it is strictly more accurate to use the MC derived variance to estimate the error on the fit values, the size of the MC data sample is not large enough to accurately determine probability contours and correlations between the fit parameters. As the mean errors found by fitting the Monte Carlo data agree well with the fit errors returned by `MINUIT` for the data sample, the errors derived from the data will be assumed to be correct. It is interesting to note, however, that in these Monte Carlo fits the variance on the real parts of both d_τ and $\tilde{d}_\tau$ appear to be 30% narrower than the errors returned directly by `MINUIT`.

Since the best fit values of the anomalous dipole couplings agree with zero, the uncertainty in the fit values are used to place 95% confidence limits on the allowed parameter range. For a Gaussian distribution, 95% of the integrated probability lies within ± 1.96 σ of the mean value. If the likelihood function $\mathcal{F}(d_\tau, \tilde{d}_\tau)$ is well

---

[1] While `KORALZ` can not generate the transversely polarized taus which signal the presence of the anomalous dipole couplings, this MC data sample can still be used to test that the fit returns a value of zero when no anomalous terms are present.
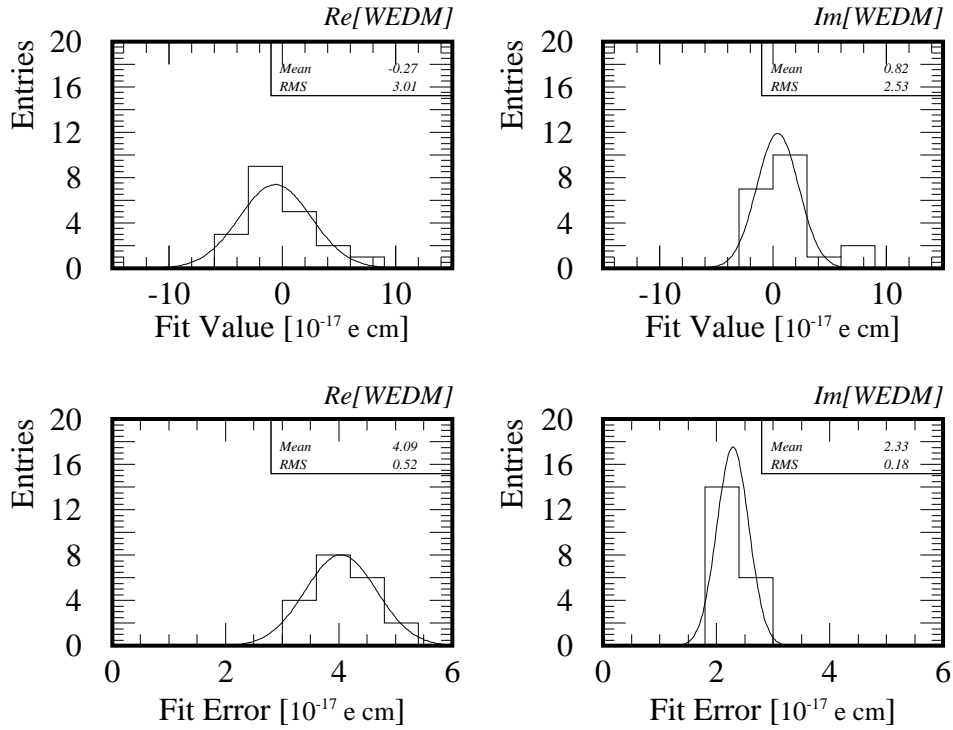
Figure 6-2: The Monte Carlo based error estimates are shown for the WEDM. The RMS variance of the mean fit value is shown along with the mean fit error quoted by `MINUIT`. There is good agreement for the imaginary part, although the variance observed for the real part is nearly 30% narrower than the quoted fit error.

behaved and linear in the fit parameters, the 95% CL range can be found by simply multiplying the errors listed in Table 6.1 by 1.96. Alternately, `MINOS` can be used to map out the 95% CL bound directly for each parameter. The comparison of these two techniques is summarized in Table 6.4 for the actual observed data, and exact agreement is found to three significant digits.

6.3   Systematic Uncertainties

The evaluation of the systematic uncertainties present in any analysis always poses something of a dilemma. Most sources of systematic error cause problems precisely because they are unknown at the time that the analysis is being performed. A truly

Table 6.4: 95% Confidence Limits

Parameter	1.96 σ	MINOS *interval*
$\Re(d_\tau)$	7.23×10^{-17} e cm	7.23×10^{-17} e cm
$\Im(d_\tau)$	4.77×10^{-17} e cm	4.77×10^{-17} e cm
$\Re(\tilde{d}_\tau)$	7.95×10^{-17} e cm	7.95×10^{-17} e cm
$\Im(\tilde{d}_\tau)$	4.72×10^{-17} e cm	4.72×10^{-17} e cm

The 95% CL range calculated directly by MINOS agrees well with the 1.96 σ bound for the observed data.

accurate estimate of the size of the various systematic effects is probably impossible in any analysis, but in the case of a statistically dominated result, arguments limiting these systematic errors to a manageable size are probably easier to come by.

Unknown or improperly handled effects can cause systematic errors in this analysis in two general ways:

- A measurement bias shifting the best fit value for the dipole moments;

- A scale error in the sensitivity to the magnitude of the dipole moments.

Assuming that the true value for the dipole moments are zero, a measurement bias will shift the likelihood fit result away from zero, while a scale error will cause the fit uncertainty to be incorrectly estimated.

In general, systematic errors can arise either from unknown phenomena or from known effects which are improperly handled in the analysis. This leads to two broad categories which must be evaluated separately:

- Effects properly modeled in the Monte Carlo simulation;

- Effects improperly modeled or unknown to the Monte Carlo simulation.

With only a few thousand identified tau hemispheres to work with, the precision of this analysis is severely limited by the available statistics, and a comprehensive

investigation of all possible sources of systematic uncertainty has not been undertaken. Rather, a number of possible effects which might be significant have been studied to verify that these sources of systematic uncertainty are small.

Tracking Resolution

The parameterization of the scaled energy resolution described in Section 5.2 is based on the Monte Carlo simulation of the combined VTX and CDC tracking resolution. A variety of SLD analyses have found that the observed tracking resolution in the data appears to be worse than that simulated by the Monte Carlo, and various attempts have been made to directly measure this effect using dimuon or Bhabha events where the true track momentum is well constrained.

To bound the size of the effect, the likelihood fit is performed using both the Monte Carlo derived parameterization and the parameterization derived from the measured tracking resolution. The difference in the likelihood fit result for both the observed data and the 20 MC data sets provides a limit on the systematic uncertainty from this source.

Azimuthal Decay Angle Efficiency

In the formulation of the effective decay matrices, the efficiency for selecting and identifying a particular tau decay is assumed to be independent of the azimuthal decay angle ϕ. Since the acceptance of the SLD detector is uniform and symmetric across the barrel region, there is no reason to expect that the decay angle between the observed charged track and the unobserved tau will influence the efficiency for selecting any given event.

This is not necessarily true near the end of the defined fiducial volume, however. As shown in Figure 6-3, for a τ^- hemisphere produced near the forward fiducial limit of $\cos\theta = 0.74$ the azimuthal decay angle of $\phi = 0$ points into the fiducial
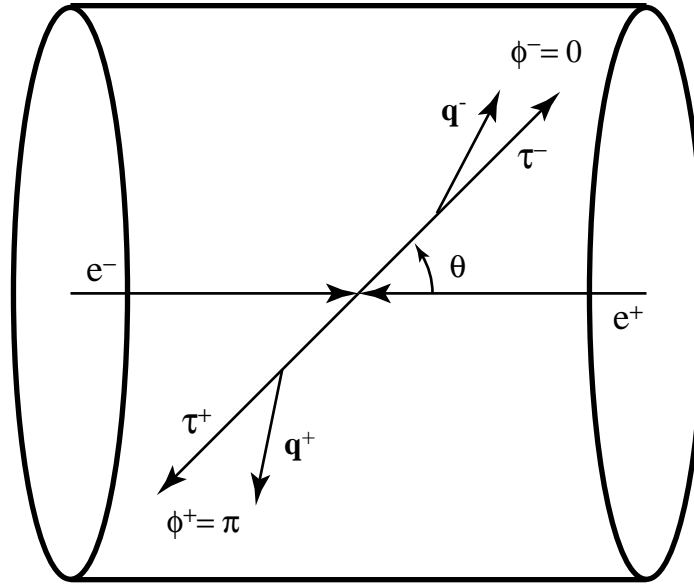
Figure 6-3: Azimuthal Decay Angle Efficiency Geometry

region while $\phi = \pi$ points out of the fiducial region. At the other end of the barrel for the τ^+ hemisphere the opposite situation is true, with the azimuthal decay angle $\phi = 0$ pointing out of the fiducial volume. Near this boundary, then, there could be a ϕ dependence to the track identification efficiency as tracks falling outside of the fiducial region will fail the identification criteria.

The additional event selection requirement that the tau momentum vector must be reconstructed into the fiducial region is designed to mitigate any possible 'edge' effect. Further, this effect should be well modeled by the Monte Carlo simulation, and no ϕ dependence is seen in the selection efficiency for events produced near this fiducial boundary. Finally, the cut on the reconstructed tau momentum can be tightened to $|\cos\theta| \leq 0.7$ or below with no apparent change in the fit results beyond a slight loss of statistics.

Detector Biases

The efficiency and resolution functions parameterized in Chapter 5 are all assumed to be independent of the charge of the track being considered. While this has been verified with the Monte Carlo data, any sort of charge bias would most likely come from a source not properly modeled by the detector simulation, anyway. Since the sensitivity of this analysis relies upon considering the difference between the τ^+ and τ^- hemispheres, this sort of charge bias would directly effect the outcome of this analysis.

One particular detector bias which has been studied is the possibility of a sagitta bias in the CDC momentum measurement.[58] One plausible source of this sort of effect is a relative azimuthal rotation between the CDC endplates. If there is an uncorrected 'twist' in the CDC wire geometry, the error made on the momentum measurement will have the functional form $p_{\mathrm{meas}} = p_0(1 + qs\cos\theta)$, where q is the charge of the track and here $\cos\theta$ is the production angle of the actual track being considered, and not the τ^- production angle. A forward-backward charge asymmetry of this form will directly fake the signal for the anomalous dipole moment by distorting the observed momentum spectra differently for the τ^+ and τ^- hemispheres.

By considering the track momenta of selected dimuon events, which should be equal and opposite, this sagitta bias can be directly measured with the data. The best fit to the observed bias is given by $s = (-0.4 \pm 1.7) \times 10^{-4}$ GeV^{-1} which is found to be consistent with zero. The extreme value of this possible charge bias has been applied as a correction to the momentum of the tracks in the data to evaluate the effect of any sort of unconstrained remaining charge bias effect in this analysis. Note that the *source* of the charge dependent momentum bias has not been assumed, but rather the allowed size of the effect from any source has been measured directly from the data.

An additional charge independent sagitta bias with a functional form $p_{\mathrm{meas}} =$

$p_0(1 + s \cos \theta)$ is also constrained by the dimuon data with a best fit value of $s = (1.9 \pm 1.7) \times 10^{-4}$ GeV^{-1}.

Event Selection and Backgrounds

The composition of the effective decay matrices depends upon an accurate Monte Carlo simulation of the particle identification efficiencies and background contamination. The tau selection described in Chapter 4 is estimated to be quite pure with only a 2% contamination from non-tau sources. Since these non-tau backgrounds simply dilute the apparent spin sensitivity of the identified tau decay modes, doubling the amount of non-tau background in the identified sample will only make a two percent difference to the sensitivity scale of this analysis.

More important is the composition of the identified tau hemispheres in terms of the spin sensitive tau decay modes. The observed number of selected events in each identified event topology agrees well with the Monte Carlo prediction for all decay types except the electrons, where there are around 9% fewer electron hemispheres seen in the data. A possible mis-understanding of the selection efficiencies can be simulated by modifying the tau branching fractions, which are used as overall scale factors in the generation of the effective decay matrices. Reducing the electron branching fraction by up to 10% has very little effect on the outcome of the analysis, as the electron channel is very pure and the relative composition of the identified electron hemispheres is virtually unchanged. The effect of modifying the hadronic pion and rho branching fraction by up to 5% is also applied as a systematic uncertainty.[2]

---

[2] These branching fractions have only been directly measured to a few percent. A variation of 5% is a conservative guess as to the accuracy of the predicted selection efficiency.
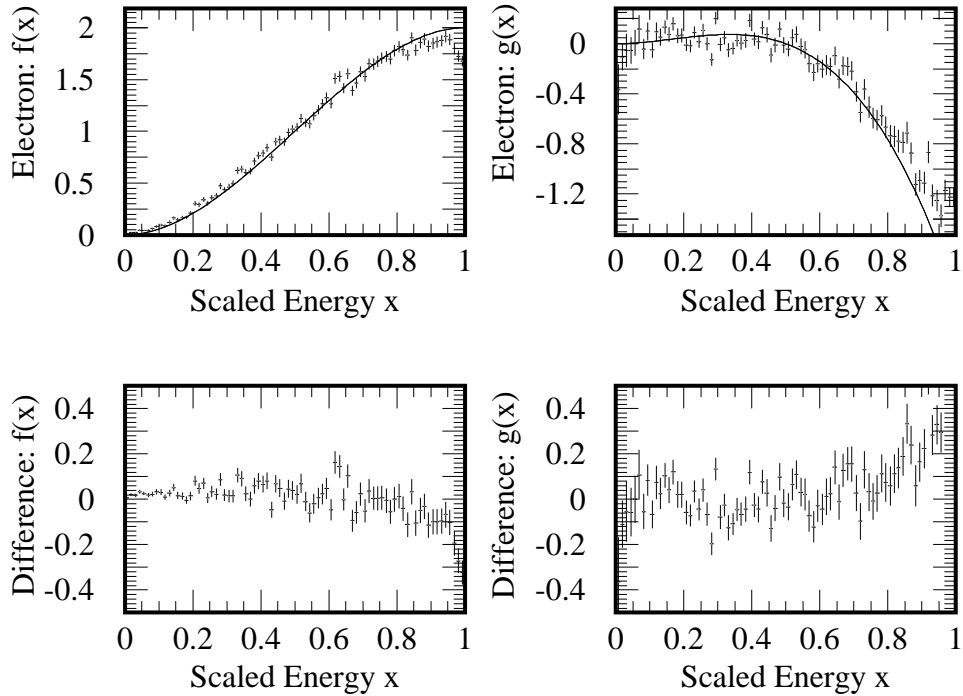
Figure 6-4: The tau center of mass decay functions $f(x)$ and $g(x)$ for the electron decay mode are shown. The points show the KORALZ predicted functions, which include initial state radiation and other higher order corrections, while the solid curve shows the tree level prediction used in the effective decay matrix formalism.

Radiative Corrections

The theoretical tau decay spectra used in calculating the effective decay matrices are described in Appendix A. These decay functions are valid only at tree-level, and do not include the effects of initial or final state radiation, higher order terms in the cross section, or the $\gamma - Z$ interference term which will all modify the observed momentum spectrum for a given tau decay mode. All of these effects *are* accurately modeled, at least to better than a percent, in the KORALZ Monte Carlo generator. The difference between the KORALZ tau decay spectra and the theoretical functions can be up to 10% in the case of the electron decay channel, and probably should be applied as a correction to the tree-level theoretical function. Rather, this difference has been assumed to be an additional source of systematic uncertainty.

Table 6.5: Fit Bias Systematic Uncertainty Summary

Systematic Uncertainty	$\Re(d_\tau)$ Bias	$\Im(d_\tau)$ Bias	$\Re(\tilde{d}_\tau)$ Bias	$\Im(\tilde{d}_\tau)$ Bias
Fiducial Region	0.55	0.09	0.37	0.40
Event Selection	0.14	0.03	0.19	0.05
Momentum Bias	0.05	0.09	0.10	0.06
Tracking Resolution	0.11	0.01	0.33	0.10
Radiative Corrections	1.12	0.47	0.08	0.39
Total	1.26	0.49	0.55	0.57

The various sources of systematic uncertainty which contribute to a bias in the fit result are tabulated along with an estimate of the bias determined by the studies described in the text. The total systematic uncertainty is the quadrature sum of the individual components, and all values are given in units of 10^{-17} e cm.

6.4   Cross Checks

A number of cross checks have been performed on this analysis, of which the most important are the likelihood fits to the Monte Carlo data samples. Even though the same Monte Carlo which is used to parameterize the resolution and efficiency functions is being used in both cases, the KORALZ generated Monte Carlo contains a nearly complete description of the underlying real physical processes, while a number of approximations and simplifications have been made in formulating the likelihood function $\mathcal{F}$. With each hemisphere being treated independently, the Monte Carlo data is then a good testing ground for the assumptions made in this analysis. The fits to the Monte Carlo data sets return zero to within statistics, and the variance of these fit results are reasonable when compared to the quoted fit errors.

The fact that the variance on the real parts of the dipole couplings appear to be narrower by 30% than the quoted fit errors is some cause for concern. If the variance had been wider, an additional systematic would certainly have been applied to cover this discrepancy. While it may well be the case that the error quoted in this analysis on the real parts of the dipole couplings are considerably larger than

Table 6.6: Scale Error Systematic Uncertainty Summary

Systematic Uncertainty	$\Re(d_\tau)$ *Scale*	$\Im(d_\tau)$ *Scale*	$\Re(\tilde{d}_\tau)$ *Scale*	$\Im(\tilde{d}_\tau)$ *Scale*
Electron Polarization	0.6%	0.6%	0.6%	0.6%
Fiducial Region	2.9%		2.3%	
Tracking Resolution	1.4%	1.3%	2.1%	1.3%
Radiative Corrections	1.2%	4.1%	1.7%	3.4%
Monte Carlo Cross Check	10%	5%	10%	5%
Total	10.6%	6.9%	10.6%	6.4%

The various sources of systematic uncertainty which vary the scale of the fit errors are tabulated along with an estimate of the scale uncertainty determined by the studies described in the text.

the true uncertainly as implied by the MC, without a more detailed understanding of the source of this discrepancy the most conservative limit has been chosen.

Another important test is to verify that the sensitivity scale of this analysis is properly understood. The ideal way to test this scale is to generate a set of Monte Carlo data with the additional anomalous coupling terms turned on, and verify that the fit result of this analysis agrees with the input coupling strengths used. In recent years, the Monte Carlo generator `SCOT` which includes these anomalous coupling terms has become available,[59] although a test with this generator has not been performed.

A second way of testing the sensitivity scale of this analysis is to use the `KORALZ` generated Monte Carlo data directly by re-weighting the generated events according to the full differential cross section given by

$$\frac{d\sigma_{L/R}}{d\Omega\, d\mathbf{q}_a^+ d\mathbf{q}_b^-} \propto \chi_{L/R}^{\alpha'\alpha\beta'\beta}(d_\tau, \tilde{d}_\tau \,|\, \cos\theta, \mathcal{P}_e)\; \mathcal{D}^{\alpha'\alpha}(\mathbf{q}_a^+)\; \mathcal{D}^{\beta'\beta}(\mathbf{q}_b^-). \qquad (6.4)$$

To calculate the event weights, the generated MC momentum vectors are used before the detector simulation is performed. These event weights are normalized to produce a mean weight of one when the anomalous couplings are turned off, and these weights

are introduced into the likelihood function by modifying Equation 6.3 to read

$$\mathcal{F}(d_\tau, \tilde{d}_\tau) \equiv -2 \sum_i w_i \ \log \mathcal{L}_i. \tag{6.5}$$

Anomalous coupling strengths up to 5×10^{-17} e cm are tested, and the resulting fit results agree with the input values to $\sim 10\%$ for the real parts and $\sim 5\%$ for the imaginary parts. Whether this discrepancy can be attributed to the likelihood fit or the re-weighting procedure is not immediately clear, and further investigation here is probably warranted. For the sake of this analysis, the observed discrepancy is being assumed as a systematic error.

6.5   Final Results

The final results are determined by taking the MINUIT fit results from Table 6.1, performing a quadrature sum with the estimated systematic bias uncertainty from Table 6.5, and multiplying the final one sigma error limits by the scale uncertainty listed in Table 6.6. The resulting fit values, including the systematic uncertainties, are then given by

$$\Re(d_\tau) = (0.2 \pm 4.3) \times 10^{-17} \ e \text{ cm}$$
$$\Im(d_\tau) = (-2.0 \pm 2.7) \times 10^{-17} \ e \text{ cm}$$
$$\Re(\tilde{d}_\tau) = (1.0 \pm 4.5) \times 10^{-17} \ e \text{ cm}$$
$$\Im(\tilde{d}_\tau) = (-2.2 \pm 2.6) \times 10^{-17} \ e \text{ cm},$$

where the errors indicate the 68% CL.

As was previously discussed in Section 6.1, the confidence intervals found by MINOS on a single parameter in a multi-parameter fit represent the change in the likelihood function due to that parameter while keeping the other parameters min-

imized. For a 95% CL interval, this is the region where $\Delta\mathcal{F} < (1.96)^2$, which has been shown to be equivalent to multiplying these 1σ errors by 1.96.

To construct an upper limit on the absolute value of the four dipole coupling terms from the fit values listed here, each fit value is considered to describe a gaussian probability density function with a given width and mean value. The symmetric region about zero which contains 95% of this probability density function is then quoted as the 95% CL upper limit for each dipole moment, and these limits are found to be

$$|\Re(d_\tau)| < 8.5 \times 10^{-17} \ e \ \text{cm} \qquad (95\% \ CL)$$

$$|\Im(d_\tau)| < 6.3 \times 10^{-17} \ e \ \text{cm} \qquad (95\% \ CL)$$

$$|\Re(\tilde{d}_\tau)| < 9.1 \times 10^{-17} \ e \ \text{cm} \qquad (95\% \ CL)$$

$$|\Im(\tilde{d}_\tau)| < 6.6 \times 10^{-17} \ e \ \text{cm} \qquad (95\% \ CL),$$

which contains a complete estimation of both the statistical and systematic uncertainties.

6.6   Comparisons

The CP violating WEDM has received a lot of attention in recent years from the LEP collaborations. By considering the expectation value of CP odd event observables similar to

$$\mathcal{O}_1 = \hat{\mathbf{z}} \cdot (\mathbf{q}^+ + \mathbf{q}^-) \tag{6.6}$$

$$\mathcal{O}_2 = \hat{\mathbf{z}} \cdot (\mathbf{q}^+ \times \mathbf{q}^-), \tag{6.7}$$

good sensitivity to both the real and imaginary part of the WEDM $(\tilde{d}_\tau)$ can be achieved.[6, 60] Results have been published previously from the Aleph and Opal

Table 6.7: *CP* Odd Observable Limits on the WEDM

Collaboration	Real Limit	Imag. Limit
Aleph	< 0.54	
Opal	< 0.50	< 1.3
Delphi	< 0.71	< 2.3
Combined	< 0.32	< 1.0

The 95% CL limits for the real and imaginary parts of the WEDM $(\tilde{d}_\tau)$ are shown in units of 10^{-17} e cm.

collaborations,[61] and now Delphi is also reporting results using these CP odd observables.

With the nearly 160pb^{-1} of data collected per experiment at the Z pole during the course of the LEP I program, the precision of these WEDM measurements is quite good. Recent updates presented at the Tau 96 conference are listed in Table 6.7.[62]

To date there have been only one other measurement attempted of the CP conserving WMDM (d_τ) performed by the L3 collaboration. In the L3 analysis, an asymmetry in the observed azimuthal decay angle is formed separately for τ^+ and τ^- decays produced into the forward and backward hemispheres. By considering the differences in the observed asymmetries, values for $|d_\tau|$ and $|\tilde{d}_\tau|$ are extracted. The same essential information is being used in the L3 analysis as has been presented here, although with a somewhat lower sensitivity. Limits from this L3 analysis were reported at the Tau 96 conference to be[63]

$$|d_\tau| < 8.1 \times 10^{-17} \ e \ \text{cm} \qquad (95\% \ CL)$$

$$|\tilde{d}_\tau| < 8.7 \times 10^{-17} \ e \ \text{cm} \qquad (95\% \ CL).$$

Measurements of the electric and magnetic dipole moments at the $\gamma \to \tau\tau$ vertex have also been made by the L3 and Aleph collaborations. In these analyses, the

energy spectrum of the extra photon from radiative tau pair decays $Z \rightarrow \tau\tau\gamma$ is fit to constrain any enhancement which would be expected in the presence of these anomalous couplings. While this is not strictly the same thing as the WMDM measured in this analysis, considerations of gauge invariance imply that the ratio d_τ^γ / d_τ^Z should be of order unity. Limits obtained from the L3 collaboration are found to be[64]

$$|d_\tau^\gamma| < 27 \times 10^{-17} \ e \ \text{cm} \qquad (90\% \ CL)$$

$$|\tilde{d}_\tau^\gamma| < 27 \times 10^{-17} \ e \ \text{cm} \qquad (90\% \ CL).$$

The two limits are the same, as the analysis actually constrains the total contribution from both dipole moments.

Given that the CP violating WEDM has already been measured by the LEP collaborations to a much higher precision than achievable in this analysis, it is an interesting to see what sort of limits the SLD data can set on the CP conserving WMDM assuming that the CP violating coupling is zero. As the four parameters in the combined likelihood fit are largely uncorrelated, very little improvement in the sensitivity is to be expected. Constraining $\tilde{d}_\tau = 0$ results in a fit to the WMDM alone of

$$\Re(d_\tau) = (-0.3 \pm 3.8) \times 10^{-17} \ e \ \text{cm}$$

$$\Im(d_\tau) = (-2.0 \pm 2.4) \times 10^{-17} \ e \ \text{cm},$$

which are virtually identical to the results listed in Table 6.1. The probability contour for the two free parameters in this fit are shown in Figure 6-5.
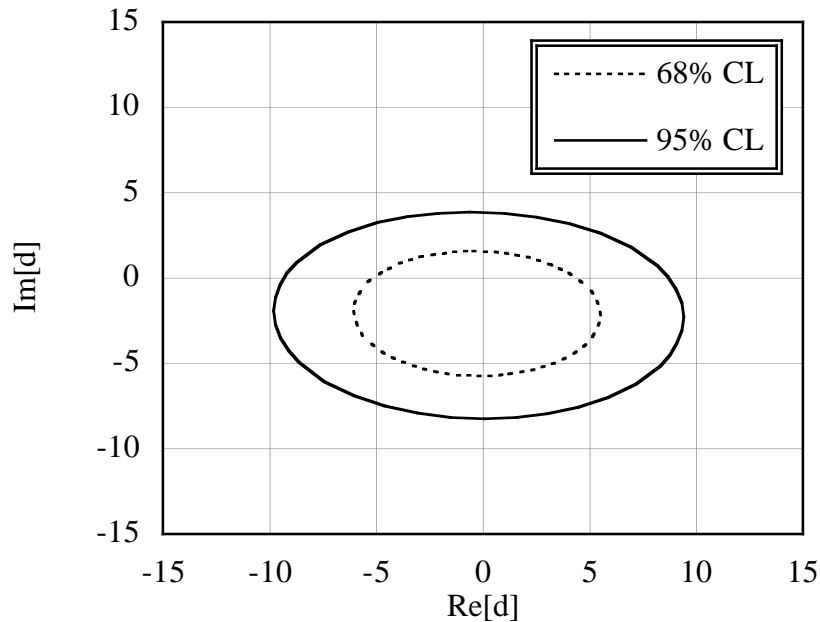
Figure 6-5: The 68% and 95% confidence intervals are shown for a fit to the real and imaginary parts of the CP conserving WMDM (d_τ) with the WEDM ($\tilde{d}_\tau$) fixed to zero. The results are shown in units of 10^{-17} e cm.

6.7   Final Remarks

While the statistical precision of this analysis is not really competitive with the limits placed on the CP violating WEDM by the LEP collaborations, it does provide one of the only measurements of the CP conserving WMDM of the tau lepton currently available. In addition, this analysis represents a unique method for extracting these anomalous couplings which has broad applications in other final state topologies, most notably the pair production of top quarks at a future high energy e^+e^- collider.

The likelihood fit method which has been developed to measure these anomalous couplings is, in principle, the most efficient method for extracting this information from any given data set. Improvements to this analysis which are currently being explored may come closer to this ultimate statistical sensitivity.

The most significant improvement which could be made to this analysis is to forego the determination of the underlying tau momentum vector, but rather inte-

grate over all possible tau momenta in any given event and construct the likelihood function directly from the observed track four-vectors. This approach would also avoid the awkward problem of parameterizing the azimuthal decay angle resolution, and will additionally extract all available information from the three body leptonic tau decay modes. As the cost of computing power continues to drop, this sort of inclusive likelihood fit will almost certainly become more common.

To date, there is no conclusive experimental result which can not be accommodated by the Standard Model. Unfortunately, the result presented here has done nothing to change this fact. The remarkable success of the Standard Model over the last thirty years has emerged from an ever increasing body of precision experimental data, and the prospects for moving beyond the Standard Model via precision measurements alone are starting to look bleak.

To truly make progress, direct evidence of new physics from a higher mass scale, meaning a higher energy machine, will almost certainly be required. With luck this evidence may come soon from the LEP II program currently running above the Z pole at CERN, although nature always has a few surprises in store for those foolish enough to try and unlock her secrets.

A

Cross Section Calculation

This appendix describes the calculation of the differential cross section for the process

$$e^+ e^- \to \tau^+ \tau^- \to a(\mathbf{q}_a^+) \, \bar{b}(\mathbf{q}_b^-) + X$$

for both the Standard Model couplings and additional anomalous couplings described by the Lagrangian

$$\mathcal{L}_{anom} = \frac{i}{2} \, \bar{\tau}^- [\sigma^{\mu\nu} q_\nu (d_\tau - i\tilde{d}_\tau \gamma^5)] \tau^+ Z_\mu. \tag{A.1}$$

Even though the various components of this calculation can be found in the literature, it is not a trivial task to reconcile the different conventions used in these calculations and in this analysis. For completeness, the calculation of the tau production amplitudes will be presented here along with a check of the tau decay amplitudes using a consistent set of coordinate and phase conventions.

The squared matrix element $|\mathcal{M}|^2$ for the production and decay of τ lepton pairs

at the Z pole can be conveniently written in terms of spin matrices,

$$|\mathcal{M}_{\mathrm{L/R}}|^2 = \chi_{L/R}^{\alpha'\alpha\beta'\beta} \, \mathcal{D}^{\alpha'\alpha}(\mathbf{q}_a^+) \, \mathcal{D}^{\beta'\beta}(\mathbf{q}_b^-) \qquad\qquad (\mathrm{A.2})$$

where $\chi_{L/R}$ is the production spin density matrix for a left or right handed incident electron, and $\mathcal{D}(\mathbf{q}_a^+)$ is the tau decay matrix to a particular final state a with momentum vector $\mathbf{q}_a^+$. The Greek superscripts indicate the explicit spin state of the produced tau leptons. A sum over any repeated index is assumed throughout this appendix.

The production spin density matrix is simply a compact notation for the production amplitudes given by

$$\chi_{L/R}^{\alpha'\alpha\beta'\beta} = \mathcal{M}^\star(e^+ e_{L/R}^- \to \tau_{\alpha'}^+ \tau_{\beta'}^-) \, \mathcal{M}(e^+ e_{L/R}^- \to \tau_\alpha^+ \tau_\beta^-), \qquad (\mathrm{A.3})$$

while the elements of the tau decay matrix are similarly given by

$$\mathcal{D}^{\alpha'\alpha}(\mathbf{q}_a^+) = \mathcal{M}^\star(\tau_{\alpha'}^+ \to a(\mathbf{q}_a^+) + X) \, \mathcal{M}(\tau_\alpha^+ \to a(\mathbf{q}_a^+) + X) \qquad (\mathrm{A.4})$$

where α', α / β', β represent the explicit spin states of the intermediate τ^+ / τ^- amplitudes. Since the tau lepton is not a final state particle, all possible tau spin states must be summed over.

A.1 Production Spin Density Matrix

There are a total of 16 terms in χ for each incident electron helicity, however these are the products of only four independent amplitudes which will be calculated here. Using the shorthand notation

$$\mathcal{A}_{L/R}(\alpha, \beta) = \mathcal{M}(e^+ e_{L/R}^- \to \tau_\alpha^+ \tau_\beta^-) \qquad\qquad (\mathrm{A.5})$$

these amplitudes can be written in the Feynman algebra as a product of the production and decay vertex vectors and the propagator matrix

$$\mathcal{A}_{L/R}(\alpha, \beta) = \Gamma_2^\mu \, \Pi_{\mu\nu} \, \Gamma_1^\nu(L/R). \tag{A.6}$$

In the Standard Model, these elements are given by

$$\Gamma_1^\nu(L/R) = -i\frac{g_z}{2} \, \bar{e}^+[\gamma^\nu(c_v - c_a\gamma^5)]e_{L/R}^- \tag{A.7}$$

$$\Gamma_2^\mu = -i\frac{g_z}{2} \, \bar{\tau}_\beta^-[\gamma^\mu(c_v - c_a\gamma^5)]\tau_\alpha^+ \tag{A.8}$$

$$\Pi_{\mu\nu} = \frac{1}{q^2 - M_Z^2 + iM_Z\Gamma_Z}(g_{\mu\nu} - q_\mu q_\nu/M_Z^2), \tag{A.9}$$

where the electron and tau couplings have been assumed to be universal. The additional anomalous couplings only modify the decay vertex, leading to an additional term of

$$\Gamma_2^\mu = -\frac{1}{2} \, \bar{\tau}_\beta^-[\sigma^{\mu\nu}q_\nu(d_\tau - i\tilde{d}_\tau\gamma^5)]\tau_\alpha^+. \tag{A.10}$$

To calculate these amplitudes, the production and decay vectors will be explicitly calculated for both the Standard Model and anomalous couplings. This calculation can be found in the literature for the polarized production of top pairs, which aside from various color factors is identical to the calculation performed here.[7]

A.1.1   Feynman Algebra

To perform this calculation, the Dirac matrix convention of Bjorken and Drell will be used, where

$$\gamma^0 = \begin{pmatrix} 1 & 0 \\ 0 & 1 \end{pmatrix}, \quad \gamma^i = \begin{pmatrix} 0 & \sigma^i \\ -\sigma^i & 0 \end{pmatrix}, \quad \gamma^5 = \begin{pmatrix} 0 & 1 \\ 1 & 0 \end{pmatrix}, \tag{A.11}$$

leading to the two particle eigenspinor solutions of the Dirac equation given by

$$u_1(p) = \sqrt{E} \begin{pmatrix} \sqrt{1 + 1/\gamma} \\ 0 \\ p_z/|p|\sqrt{1 - 1/\gamma} \\ p_+/|p|\sqrt{1 - 1/\gamma} \end{pmatrix} \tag{A.12}$$

$$u_2(p) = \sqrt{E} \begin{pmatrix} 0 \\ \sqrt{1 + 1/\gamma} \\ p_-/|p|\sqrt{1 - 1/\gamma} \\ -p_z/|p|\sqrt{1 - 1/\gamma} \end{pmatrix}, \tag{A.13}$$

where $p_\pm = p_x \pm ip_y$, E is the energy of the particle, and $\gamma = E/m$ is the standard relativistic factor.[65]

The u_1 solution represents a particle with spin in the $+\hat{z}$ direction, while the anti-particle solution with the same spin orientation can be found by applying the charge conjugation operation,

$$v(p) = i\gamma^2 u^\star(p) \tag{A.14}$$

$$v_1(p) = \sqrt{E} \begin{pmatrix} p_-/|p|\sqrt{1 - 1/\gamma} \\ -p_z/|p|\sqrt{1 - 1/\gamma} \\ 0 \\ \sqrt{1 + 1/\gamma} \end{pmatrix} \tag{A.15}$$

$$v_2(p) = \sqrt{E} \begin{pmatrix} -p_z/|p|\sqrt{1 - 1/\gamma} \\ -p_+/|p|\sqrt{1 - 1/\gamma} \\ -\sqrt{1 + 1/\gamma} \\ 0 \end{pmatrix}, \tag{A.16}$$

where again the v_1 solution represents an anti-particle with spin in the $+\hat{\mathbf{z}}$ direction. These eigenspinors are normalized by the convention found in Griffiths such that $u^\dagger u = 2E$.[66] The adjoint spinors are defined in the usual way, such that $\bar{u} = u^\dagger \gamma^0$ and $\bar{v} = v^\dagger \gamma^0$.

A.1.2   Production Vector

This calculation will be performed in the center of mass frame of the $e^+ e^-$ collision, assuming that the initial state particles are massless fermions.

Using the Dirac eigenspinors listed above, with the electron traveling in the $+z$ direction:

$$e_L^- = \sqrt{E} \begin{pmatrix} 0 \\ +1 \\ 0 \\ -1 \end{pmatrix} \qquad\qquad e_R^- = \sqrt{E} \begin{pmatrix} +1 \\ 0 \\ +1 \\ 0 \end{pmatrix} \qquad\qquad \text{(A.17)}$$

$$\bar{e}_L^+ = \sqrt{E} \begin{pmatrix} 0 & +1 & 0 & -1 \end{pmatrix} \qquad \bar{e}_R^+ = \sqrt{E} \begin{pmatrix} +1 & 0 & +1 & 0 \end{pmatrix}$$

There are only two non-zero production vectors Γ_1 corresponding to left and right

handed Z^0 bosons:[1]

$$\Gamma_1^{\mu} = -i\frac{g_z}{2}\ \bar{e}^+[\gamma^{\mu}(c_v - c_a\gamma^5)]e^- \tag{A.18}$$

$$\Gamma_1^{-+} = 0 \qquad\qquad\qquad \Gamma_1^{+-} = 0$$

$$\Gamma_1^{--} = -ig_z E(c_v + c_a)\begin{pmatrix} 0 \\ -1 \\ +i \\ 0 \end{pmatrix} \qquad \Gamma_1^{++} = -ig_z E(c_v - c_a)\begin{pmatrix} 0 \\ +1 \\ +i \\ 0 \end{pmatrix}. \tag{A.19}$$

The notation $\Gamma_1^{\alpha\beta}$ describes an $e^+(e^-)$ with spin oriented in the direction $\alpha(\beta)$, where $(+)$ always refers to a spin aligned in the $+\hat{\mathbf{z}}$ direction. For the electron traveling in the $+\hat{\mathbf{z}}$ direction this is the same as the helicity convention, where $(+)$ would indicate a right-handed electron. For the positron, however, the notation is opposite to the helicity convention, since the positron is traveling in the $-\hat{\mathbf{z}}$ direction. As will be shown, the reason for this somewhat non-standard notation has to do with the spin decay matrices which are explicitly written in terms of the tau spin orientation rather than the tau helicity.

These production vectors can be combined with the propagator matrix to create a common row vector which will be used to calculate the amplitudes for both the Standard Model and anomalous decay couplings. For notational simplicity, the propagator factor from Equation A.9

$$\frac{1}{q^2 - M_Z^2 + iM_Z\Gamma_Z} \tag{A.20}$$

will be assumed to be present in every amplitude, and will be dropped for the remainder of this calculation. In the center of mass frame, the propagator has a

---

[1] Since there are only two non-zero SM production vectors, the incoming electron spin directly determines the spin of the produced Z boson.

particularly simple form since $q_0 = \sqrt{s}$ and $q_i = 0$:

$$\Pi_{\mu\nu} = [g_{\mu\nu} - q_\mu q_\nu / M_Z^2] \tag{A.21}$$

$$\Pi = \begin{pmatrix} 1 - s/M_Z^2 & 0 & 0 & 0 \\ 0 & -1 & 0 & 0 \\ 0 & 0 & -1 & 0 \\ 0 & 0 & 0 & -1 \end{pmatrix}. \tag{A.22}$$

Contracting this propagator with the production vector results in the two non-zero components

$$\Pi\Gamma_1^{--} = -ig_z E(c_v + c_a) \begin{pmatrix} 0 & +1 & -i & 0 \end{pmatrix} \tag{A.23}$$

$$\Pi\Gamma_1^{++} = -ig_z E(c_v - c_a) \begin{pmatrix} 0 & -1 & -i & 0 \end{pmatrix}. \tag{A.24}$$

This four vector is the weak current describing Z boson production, and at this point it is useful to rotate this four vector to take into account the tau production angle.

Defining the angle theta to lie between the outgoing τ^- and incoming e^-, a rotation of minus theta needs to be applied to the initial coupling current. This rotation is performed by the following matrix:

$$\mathcal{R}(\theta) = \begin{pmatrix} 1 & 0 & 0 & 0 \\ 0 & \cos\theta & 0 & -\sin\theta \\ 0 & 0 & 1 & 0 \\ 0 & \sin\theta & 0 & \cos\theta \end{pmatrix}. \tag{A.25}$$

Putting all of this together, the rotated production vector is given by

$$\tilde{\Gamma}_L = \mathcal{R}(\theta) \ \Pi\Gamma_1^{+-} = -ig_z E(c_v + c_a) \left(\begin{array}{cccc} 0 & +\cos\theta & -i & +\sin\theta \end{array} \right) \tag{A.26}$$

$$\tilde{\Gamma}_R = \mathcal{R}(\theta) \ \Pi\Gamma_1^{-+} = -ig_z E(c_v - c_a) \left(\begin{array}{cccc} 0 & -\cos\theta & -i & -\sin\theta \end{array} \right), \tag{A.27}$$

where these are now written explicitly in terms of the incoming electron helicity.

A.1.3   Decay Vector

For the decay vector, the coordinate system is defined such that the fermion is traveling in the $+z$ direction, just as in the case of the production vector. We will take the tau mass into account, resulting in the following outgoing eigenspinors:

$$\tau_L^+ = \sqrt{E} \begin{pmatrix} +\sqrt{1 - 1/\gamma} \\ 0 \\ -\sqrt{1 + 1/\gamma} \\ 0 \end{pmatrix} \qquad \tau_R^+ = \sqrt{E} \begin{pmatrix} 0 \\ +\sqrt{1 - 1/\gamma} \\ 0 \\ +\sqrt{1 + 1/\gamma} \end{pmatrix} \tag{A.28}$$

$$\begin{aligned} \bar{\tau}_L^- &= \sqrt{E} \left(\begin{array}{cccc} 0 & +\sqrt{1 + 1/\gamma} & 0 & +\sqrt{1 - 1/\gamma} \end{array} \right) \\ \bar{\tau}_R^- &= \sqrt{E} \left(\begin{array}{cccc} +\sqrt{1 + 1/\gamma} & 0 & -\sqrt{1 - 1/\gamma} & 0 \end{array} \right). \end{aligned} \tag{A.29}$$

The decay vector (Γ_2) has both a standard model term and an anomalous cou-

pling term. The standard model term is given by

$$\Gamma_2^\mu = -i\frac{g_z}{2}\,\bar{\tau}^-[\gamma^\mu(c_v - c_a\gamma^5)]\tau^+ \tag{A.30}$$

$$\Gamma_2^{++} = -ig_z E(c_v - c_a') \begin{pmatrix} 0 \\ +1 \\ -i \\ 0 \end{pmatrix} \qquad \Gamma_2^{--} = -ig_z E(c_v + c_a') \begin{pmatrix} 0 \\ -1 \\ -i \\ 0 \end{pmatrix}$$

$$\Gamma_2^{+-} = -ig_z E/\gamma \begin{pmatrix} -c_a \\ 0 \\ 0 \\ -c_v \end{pmatrix} \qquad \Gamma_2^{-+} = -ig_z E/\gamma \begin{pmatrix} +c_a \\ 0 \\ 0 \\ -c_v \end{pmatrix}, \tag{A.31}$$

where $c_a' = \beta c_a$, while the anomalous coupling term is given by

$$\Gamma_2^\mu = -\frac{1}{2}\,\bar{\tau}^-[\sigma^{\mu\nu}q_\nu(d_\tau - i\tilde{d}_\tau\gamma^5)]\tau^+ \tag{A.32}$$

$$\Gamma_2^{++} = -ig_z E(k_v/\gamma) \begin{pmatrix} 0 \\ -1 \\ +i \\ 0 \end{pmatrix} \qquad \Gamma_2^{--} = -ig_z E(k_v/\gamma) \begin{pmatrix} 0 \\ +1 \\ +i \\ 0 \end{pmatrix}$$

$$\Gamma_2^{+-} = -ig_z E(k_v - k_a') \begin{pmatrix} 0 \\ 0 \\ 0 \\ +1 \end{pmatrix} \qquad \Gamma_2^{-+} = -ig_z E(k_v + k_a') \begin{pmatrix} 0 \\ 0 \\ 0 \\ +1 \end{pmatrix} \tag{A.33}$$

where $k_v = \frac{\sqrt{s}}{g_z}d_\tau$, $k_a = i\frac{\sqrt{s}}{g_z}\tilde{d}_\tau$, and $k_a' = \beta k_a$. Again, the indices of $\Gamma_2^{\alpha\beta}$ represent the spin orientation along the outgoing fermion direction $\hat{\mathbf{z}}$, rather than the helicity of the outgoing particle. That is to say, the spin notation for the τ^+ is given by

$\hat{\sigma}_{(\tau+)} \cdot \hat{\mathbf{z}}$, where $\hat{\mathbf{z}}$ is defined by the τ^- direction. The more common helicity notation can be recovered by reversing the τ^+ index α.

A.1.4   Production Amplitudes

All of the pieces are now in hand to calculate the amplitudes. Considering the left and right handed production amplitudes separately, the product of the production and decay vectors are listed in Table A.1 and Table A.2. Remember that all amplitudes must be multiplied by the propagator factor from Equation A.20.

These amplitudes are explicitly calculated using the Z boson propagator, although the amplitudes for the photon propagator can also be found by making the substitutions

$$
\begin{aligned}
c_v &\rightarrow 2g_e/g_z \\
c_a &\rightarrow 0
\end{aligned}
\tag{A.34}
$$

along with modifying the propagator factor by the substitution

$$
\frac{1}{q^2 - M_Z^2 + iM_Z\Gamma_Z} \rightarrow \frac{1}{q^2}.
\tag{A.35}
$$

The complete amplitude, then, is the sum of the Z boson and photon terms. For completeness, the sixteen terms of χ for both left-handed and right-handed incident electrons are listed in Table A.3 in the relativistic limit of vanishing tau lepton mass and ignoring the photon propagator amplitudes.

A.2   Decay Matrix

The partial width calculation for various one prong tau decays was performed before the tau lepton was actually discovered.[12] Working in the tau rest frame, the partial width for a particular tau decay can be written in terms of a spin independent decay

Table A.1: Standard Model Amplitudes

	Left Handed $-g_z^2 E^2(c_v + c_a)\times$	*Right Handed* $-g_z^2 E^2(c_v - c_a)\times$
$\mathcal{A}(++)$	$-(c_v - c_a')(1 - \cos\theta)$	$-(c_v - c_a')(1 + \cos\theta)$
$\mathcal{A}(--)$	$-(c_v + c_a')(1 + \cos\theta)$	$-(c_v + c_a')(1 - \cos\theta)$
$\mathcal{A}(+-)$	$-(c_v/\gamma)\sin\theta$	$+(c_v/\gamma)\sin\theta$
$\mathcal{A}(-+)$	$-(c_v/\gamma)\sin\theta$	$+(c_v/\gamma)\sin\theta$

Production amplitudes are shown separately for left and right handed incident electrons. In the relativistic limit only the $\mathcal{A}(++)$ and $\mathcal{A}(--)$ amplitudes are non-zero.

Table A.2: Anomalous Coupling Amplitudes

	Left Handed $-g_z^2 E^2(c_v + c_a)\times$	*Right Handed* $-g_z^2 E^2(c_v - c_a)\times$
$\mathcal{A}(++)$	$+(k_v/\gamma)(1 - \cos\theta)$	$+(k_v/\gamma)(1 + \cos\theta)$
$\mathcal{A}(--)$	$+(k_v/\gamma)(1 + \cos\theta)$	$+(k_v/\gamma)(1 - \cos\theta)$
$\mathcal{A}(+-)$	$+(k_v - k_a')\sin\theta$	$-(k_v - k_a')\sin\theta$
$\mathcal{A}(-+)$	$+(k_v + k_a')\sin\theta$	$-(k_v + k_a')\sin\theta$

Production amplitudes are shown separately for left and right handed incident electrons. In the relativistic limit only the $\mathcal{A}(+-)$ and $\mathcal{A}(-+)$ amplitudes are non-zero.

Table A.3: Relativistic Production Spin Density Matrix Elements

Matrix Element	Left Handed $g_z^4 E^4 (c_v + c_a)^2 \times$	Right Handed $g_z^4 E^4 (c_v - c_a)^2 \times$
χ^{++++}	$(c_v - c_a)^2 (1 - \cos\theta)^2$	$(c_v - c_a)^2 (1 + \cos\theta)^2$
χ^{----}	$(c_v + c_a)^2 (1 + \cos\theta)^2$	$(c_v + c_a)^2 (1 - \cos\theta)^2$
χ^{++--}	$|k_v - k_a|^2 \sin^2\theta$	$|k_v - k_a|^2 \sin^2\theta$
χ^{--++}	$|k_v + k_a|^2 \sin^2\theta$	$|k_v + k_a|^2 \sin^2\theta$
χ^{+++-}	$-(k_v - k_a)(c_v - c_a)\sin\theta(1 - \cos\theta)$	$(k_v - k_a)(c_v - c_a)\sin\theta(1 + \cos\theta)$
χ^{++-+}	complex conjugate	c.c.
χ^{---+}	$-(k_v + k_a)(c_v + c_a)\sin\theta(1 + \cos\theta)$	$(k_v + k_a)(c_v + c_a)\sin\theta(1 - \cos\theta)$
χ^{--+-}	c.c.	c.c.
χ^{+-++}	$-(k_v + k_a)(c_v - c_a)\sin\theta(1 - \cos\theta)$	$(k_v + k_a)(c_v - c_a)\sin\theta(1 + \cos\theta)$
χ^{-+++}	c.c.	c.c.
χ^{-+--}	$-(k_v - k_a)(c_v + c_a)\sin\theta(1 + \cos\theta)$	$(k_v - k_a)(c_v + c_a)\sin\theta(1 - \cos\theta)$
χ^{+---}	c.c.	c.c.
χ^{+-+-}	$(c_v^2 - c_a^2)(1 - \cos^2\theta)$	$(c_v^2 - c_a^2)(1 - \cos^2\theta)$
χ^{-+-+}	c.c.	c.c.
χ^{-++-}	$(k_v + k_a)^\star (k_v - k_a)\sin^2\theta$	$(k_v + k_a)^\star (k_v - k_a)\sin^2\theta$
χ^{+--+}	c.c.	c.c.

The spin density matrix elements are given by $\chi^{\alpha'\alpha\beta'\beta} = \mathcal{A}^\star(\alpha', \beta')\mathcal{A}(\alpha, \beta)$. The first four terms contribute to the total cross section, as well as produce the correlated longitudinal tau polarization. The second and third set of four terms generate the transverse polarization of the τ^- and τ^+ respectively, and will be zero in the absence of the anomalous couplings. The last four terms, responsible for transverse spin correlations, have both a SM and anomalous component.

function $f(\mathbf{q}^\star)$ and a spin dependent decay function $g(\mathbf{q}^\star)$ as

$$
\begin{aligned}
\tfrac{d\Gamma}{d\mathbf{q}^\star}(\tau^- \to b(\mathbf{q}^\star) + X) &\propto f_b(\mathbf{q}^\star) + g_b(\mathbf{q}^\star)\,\hat\sigma \cdot \hat{\mathbf{q}}^\star \\
\tfrac{d\Gamma}{d\mathbf{q}^\star}(\tau^+ \to a(\mathbf{q}^\star) + X) &\propto f_a(\mathbf{q}^\star) - g_a(\mathbf{q}^\star)\,\hat\sigma \cdot \hat{\mathbf{q}}^\star
\end{aligned}
\tag{A.36}
$$

where $\hat\sigma$ is the tau spin vector and $\mathbf{q}^\star$ is the momentum of the tau decay product in the tau rest frame. In this analysis it is assumed that the only anomalous couplings enter through the $Z \to \tau^+\tau^-$ vertex, so the tau decays retain their Standard Model coupling parameters, and the symmetry between the τ^+ and τ^- partial widths is required by CP invariance.

A.2.1   Coordinate System

The coordinate system used for the tau decay matrices is defined by the production spin density matrix, where the $+\hat{\mathbf{z}}$ direction is always taken to be pointing along the τ^- momentum vector, while the $+\hat{\mathbf{x}}$ direction lies in the production plane pointing in the direction of increasing production angle θ, and the $+\hat{\mathbf{y}}$ direction is oriented out of the production plane to complete a right handed coordinate system. For the τ^+, this means that a spin of $+\hat\sigma_z$ is pointing opposite to its direction of motion.

A.2.2   Decay Functions

The tau decay matrix $\mathcal{D}(\mathbf{q}^\star_\mp)$ defined in Equation A.4 is then equal to the differential decay width written in the Dirac spin space of the tau as

$$
\begin{aligned}
\mathcal{D}(\mathbf{q}^\star_\mp) &= f(\mathbf{q}^\star) \pm g(\mathbf{q}^\star)\,\hat\sigma \cdot \hat{\mathbf{q}}^\star \\
&= \begin{pmatrix}
f(\mathbf{q}^\star) \pm g(\mathbf{q}^\star)\cos\theta^\star & \pm g(\mathbf{q}^\star)\sin\theta^\star e^{-i\phi^\star} \\
\pm g(\mathbf{q}^\star)\sin\theta^\star e^{+i\phi^\star} & f(\mathbf{q}^\star) \mp g(\mathbf{q}^\star)\cos\theta^\star
\end{pmatrix}.
\end{aligned}
\tag{A.37}
$$
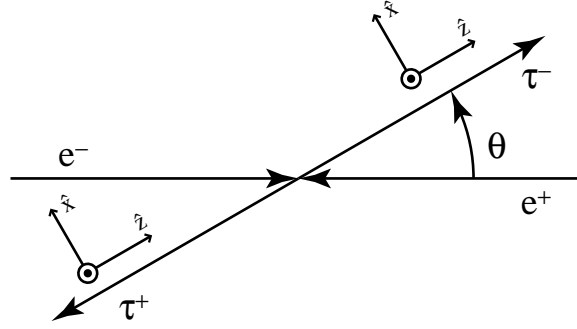
Figure A-1: The tau decay matrix coordinate system is shown.

The matrix $\mathcal{D}(\mathbf{q}^\star)$ is normalized so that

$$\int \mathcal{D}(\mathbf{q}_a^\star) \, d\mathbf{q}_a^\star = \begin{pmatrix} 1 & 0 \\ 0 & 1 \end{pmatrix}, \tag{A.38}$$

resulting in the unit matrix when integrated over all momenta $\mathbf{q}^\star$.

For the two body decay $\tau^- \to \pi^- \nu_\tau$ the decay functions have a particularly simple form,

$$f_\pi(\mathbf{q}^\star) = \frac{1}{4\pi} \, \delta(x^\star - 1) \tag{A.39}$$

$$g_\pi(\mathbf{q}^\star) = \frac{1}{4\pi} \, \delta(x^\star - 1), \tag{A.40}$$

where $x^\star = 2E_\pi/E_\tau$ is the scaled energy of the observed pion, which is required to be one by the kinematics of the two body decay. In this example, the pion is assumed to be massless.

In the case of the three body semi-leptonic decay $\tau^- \to e^- \bar{\nu}_e \nu_\tau$ there is an extra

unobserved neutrino which must be integrated over first, resulting in decay functions of the form

$$
f_e(\mathbf{q}^\star) = +\frac{(x^\star)^2}{2\pi}(3 - 2x^\star)
$$
$$
g_e(\mathbf{q}^\star) = -\frac{(x^\star)^2}{2\pi}(2x^\star - 1),
\tag{A.41}
$$

where again $x^\star = 2E_e/E_\tau$ is the scaled energy of the observed charged particle, and again the final state particle is assumed to be massless. The exact decay functions for the muon and rho decays are somewhat more complicated due to the non-negligible mass terms. These functional forms will be presented in Sections A.2.7 and A.2.8 respectively.

A.2.3   Boost Algebra

The decay matrices described in the previous section are written in terms of experimentally unavailable parameters $(x^\star, \theta^\star, \phi^\star)$ in the tau rest frame. To write these in terms of the lab frame variables of interest (x, ϕ), a Lorentz boost must be applied along the tau flight direction, followed by a change of variables. This boost can be written as

$$
\begin{pmatrix} E \\ \mathbf{p}_\parallel \\ \mathbf{p}_\perp \end{pmatrix} = \begin{pmatrix} \gamma & \beta\gamma & 0 \\ \beta\gamma & \gamma & 0 \\ 0 & 0 & 1 \end{pmatrix} \begin{pmatrix} E^\star \\ \mathbf{p}_\parallel^\star \\ \mathbf{p}_\perp^\star \end{pmatrix}
\tag{A.42}
$$

where $\beta\gamma = \mathbf{p}_\tau/m_\tau$ and $\gamma = E_\tau/m_\tau$ are the Lorentz parameters describing the boost of the tau rest frame into the lab frame, while the decay products are assumed to be massless. Note that β is signed by the individual tau momentum, so that in the coordinate system where $\hat{\mathbf{z}} = \hat{\mathbf{q}}_{\tau^-}$, $\beta^- \approx +1$ and $\beta^+ \approx -1$.

Substituting the relations

$$E^\star = E_0^\star x^\star$$
$$\mathbf{p}_\parallel^\star = E_0^\star x^\star \cos\theta^\star \tag{A.43}$$
$$\mathbf{p}_\perp^\star = E_0^\star x^\star \sin\theta^\star,$$

where $E_0^\star = m_\tau/2$ is the maximum allowed decay energy, into Equation A.42 gives the following relations in the Z center of mass frame,

$$E = x^\star E_0^\star (\gamma + \beta\gamma\cos\theta^\star)$$
$$\mathbf{p}_\parallel = x^\star E_0^\star (\beta\gamma + \gamma\cos\theta^\star) \tag{A.44}$$
$$\mathbf{p}_\perp = x^\star E_0^\star \sin\theta^\star,$$

which can be explicitly written in terms of the lab frame kinematic variables as

$$x = \frac{x^\star}{2}(1 + \beta y^\star)$$
$$y = \frac{\beta + y^\star}{1 + \beta y^\star} \tag{A.45}$$
$$\phi = \phi^\star$$

where $x = E/E_\tau$, $y = \cos\theta$, and the transverse azimuthal angle ϕ is invariant by virtue of being transverse to the boost direction. The opposite boost from the lab frame to the center of mass frame gives the useful inverse relations

$$x^\star = 2\gamma^2 x(1 - \beta y)$$
$$y^\star = \frac{y - \beta}{1 - \beta y} \tag{A.46}$$
$$\phi^\star = \phi.$$

A.2.4   Change of Variables

The differential partial width in the lab frame can be written in terms of the differential partial width in the tau rest frame as

$$\frac{d^2\Gamma}{dxd\phi} = \int \frac{d^3\Gamma}{dx^\star dy^\star d\phi^\star} \left| \frac{\partial(x^\star, y^\star)}{\partial(x, y)} \right| \left| \frac{\partial\phi^\star}{\partial\phi} \right| dy, \tag{A.47}$$

where the Jacobian can be found from Equation A.46 to be

$$\left| \frac{\partial(x^\star, y^\star)}{\partial(x, y)} \right| = \left| \frac{\partial x^\star}{\partial x} \frac{\partial y^\star}{\partial y} - \frac{\partial x^\star}{\partial y} \frac{\partial y^\star}{\partial x} \right|$$
$$= \frac{2}{1 - \beta y}. \tag{A.48}$$

Some care must be taken when considering the limits of integration for y at a fixed energy x. The lab frame angle y is solely dependent upon the center of mass angle $y^\star$, which is bounded in the center of mass frame by the relation in Equation A.45

$$y^\star = \frac{1}{\beta}(2\frac{x}{x^\star} - 1). \tag{A.49}$$

Any given value of x describes a curve in the $x^\star - y^\star$ plane which is bounded at both ends by the kinematic limits of the center of mass frame variables. At $x^\star = 1$, there is a bound on $y^\star = \frac{1}{\beta}(2x - 1)$ which is a lower bound for τ^- decays ($\beta \approx +1$) and an upper bound for τ^+ decays ($\beta \approx -1$). Similarly, there is a lower bound on $x^\star$ when $y^\star = \text{sign}(\beta)$. Using Equation A.45, this gives limits of

$$y_{lo}^- = +\frac{1}{|\beta|}(1 - \frac{1}{2x\gamma^2}) \qquad y_{hi}^- = +1 \tag{A.50}$$

$$y_{hi}^+ = -\frac{1}{|\beta|}(1 - \frac{1}{2x\gamma^2}) \qquad y_{lo}^+ = -1 \tag{A.51}$$

on the integral over the lab frame variable y.

From Equation A.37, there are three separate integrals which need to be per-
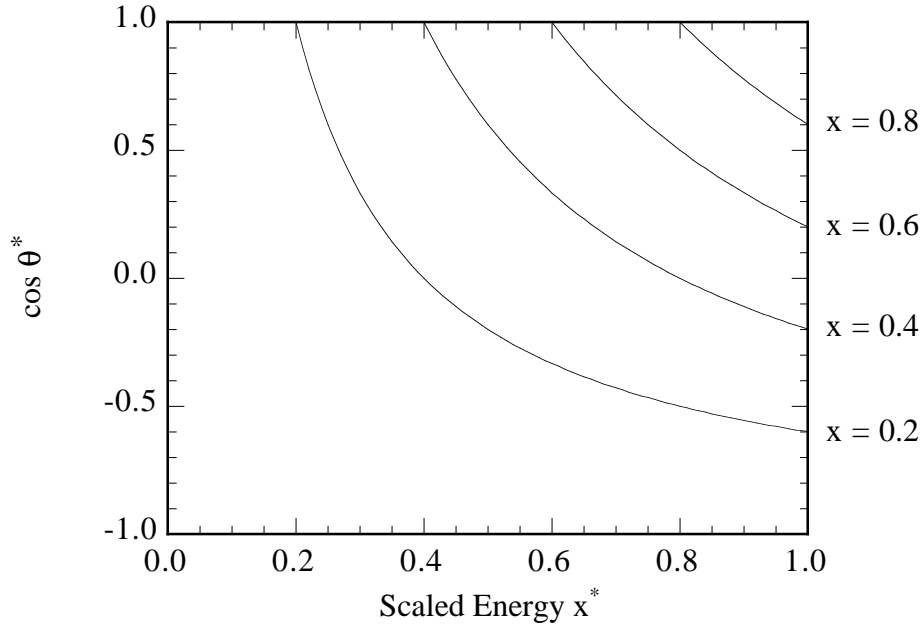
Figure A-2: Limits of integration in the tau center of mass frame for a fixed value of the lab frame variable x

formed,

$$A(x) = \int f(x^\star) \, |J| \, dy$$

$$B(x) = \int g(x^\star) \cos \theta^\star \, |J| \, dy \qquad \text{(A.52)}$$

$$C(x) = \int g(x^\star) \sin \theta^\star \, |J| \, dy$$

from which we can write the tau decay matrix in terms of lab frame variables as

$$\mathcal{D}^{\mp}(x, \phi) = \begin{pmatrix} A(x) \pm B(x) & \pm C(x) e^{-i\phi} \\ \pm C(x) e^{+i\phi} & A(x) \mp B(x) \end{pmatrix}. \qquad \text{(A.53)}$$

A.2.5   Pion Decay

For the hadronic decay $\tau^{\mp} \to \pi^{\mp} \nu_{\tau}$, described by Equation A.40, $x^{\star}$ is restricted to be equal to one by the kinematics of the two body decay. In this case,

$$
\frac{d^2\Gamma}{dx\,d\phi} = \frac{d^2\Gamma}{dy^{\star}d\phi^{\star}} \left| \frac{\partial(y^{\star}, \phi^{\star})}{\partial(x, \phi)} \right|
$$
$$
y^{\star} = \frac{1}{\beta}(2x - 1) \tag{A.54}
$$
$$
\frac{\partial(y^{\star}, \phi^{\star})}{\partial(x, \phi)} = \frac{2}{\beta},
$$

and the three lab frame functions are given by

$$
A^{\mp}(x) = f_{\pi}(x^{\star} = 1)\frac{2}{\beta}
$$
$$
= \frac{1}{2\pi|\beta|} \tag{A.55}
$$
$$
B^{\mp}(x) = g_{\pi}(x^{\star} = 1)\frac{2}{\beta}y^{\star}
$$
$$
= \pm\frac{1}{2\pi\beta^2}(2x - 1) \tag{A.56}
$$
$$
C^{\mp}(x) = g_{\pi}(x^{\star} = 1)\frac{2}{\beta}\sqrt{1 - (y^{\star})^2}
$$
$$
= \frac{1}{2\pi\beta^2}2\sqrt{x(1 - x) + (\beta^2 - 1)/4}. \tag{A.57}
$$

The subsequent decay matrix, in the limit that $\beta \to 1$, is given by

$$
\mathcal{D}^{\mp}(x, \phi) = \frac{1}{2\pi} \begin{pmatrix} 2x & \pm 2\sqrt{x(1 - x)}e^{-i\phi} \\ \pm 2\sqrt{x(1 - x)}e^{+i\phi} & 2(1 - x) \end{pmatrix}, \tag{A.58}
$$

which is both properly normalized under integration over all momenta, and shows that left handed τ^- decays have the same energy spectrum as right handed τ^+ decays.

A.2.6   Electron Decay

For the leptonic decay $\tau^- \to e^- \bar{\nu}_e \nu_\tau$, described by Equation A.41, $x^\star$ is no longer restricted to be equal to one, and the integrals in Equation A.52 must be performed. Starting with the first integral

$$A^\mp(x) = \frac{1}{2\pi} \int (3(x^\star)^2 - 2(x^\star)^3) \frac{2}{1 - \beta y} \, dy, \tag{A.59}$$

it is easier to work with the variable $u = (1 - \beta y)$, where $x^\star = (2\gamma^2 x)u$, giving

$$A^\mp(x) = -\frac{1}{2\pi\beta} \int (6(2\gamma^2 x)^2 u - 4(2\gamma^2 x)^3 u^2) \, du. \tag{A.60}$$

Changing the integration limits from y to u gives $\{\frac{1}{2\pi\gamma^2}, (1 - |\beta|)\}$ where these are the $\{$lo,hi$\}$ limits for a τ^- decay and the $\{$hi,lo$\}$ limits for a τ^+ decay. Flipping the limits of integration will cancel the sign of the factor of $\frac{1}{\beta}$ in equation A.60 giving

$$\begin{aligned}
A^\mp(x) &= -\frac{1}{2\pi|\beta|} \left[3x^2(2\gamma^2)u^2 - \frac{4}{3}x^3(2\gamma^2)^3 u^3 \right]_{1/(2x\gamma^2)}^{1-|\beta|} \\
&= \frac{1}{2\pi|\beta|} \left[\frac{5}{3} - 3x^2(\frac{2}{1+|\beta|})^2 + \frac{4}{3}x^3(\frac{2}{1+|\beta|})^3 \right] \\
&= \frac{1}{2\pi} \left[\frac{5}{3} - 3x^2 + \frac{4}{3}x^3 \right] \quad \text{as } (|\beta| \to 1).
\end{aligned} \tag{A.61}$$

The second integral can be evaluated in a similar way with

$$\begin{aligned}
B^\mp(x) &= -\frac{1}{2\pi} \int (2(x^\star)^3 - (x^\star)^2) \frac{2}{1 - \beta y} y^\star \, dy \\
&= \frac{1}{2\pi\beta^2} \int (4(2\gamma^2 x)^3 u - 2(2\gamma^2 x)^2)(\frac{1}{\gamma^2} - u) \, du.
\end{aligned}$$

In this integral, the $\cos\theta^\star$ has produced an extra factor of $1/\beta$ in front of the integral so that reversing the limits of integration will pick up a factor of -1 not canceled

by the factor of $1/\beta^2$.

$$
\begin{aligned}
B^{\mp}(x) &= \pm\frac{1}{2\pi\beta^2} \int_{1/(2x\gamma^2)}^{1-|\beta|} \left[4(2\gamma^2 x)^3(\frac{1}{\gamma^2}u - u^2) - 2(2\gamma^2 x)^2(\frac{1}{\gamma^2} - u) \right]\, du \\
&= \pm\frac{1}{2\pi\beta^2} \left[\frac{1}{3} - 4x^2(\frac{2}{1+|\beta|}) + (x^2 + 4x^3)(\frac{2}{1+|\beta|})^2 - \frac{4}{3}x^3(\frac{2}{1+|\beta|})^3 \right] \\
&= \pm\frac{1}{2\pi} \left[\frac{1}{3} - 3x^2 + \frac{8}{3}x^3 \right] \text{ as } (|\beta| \to 1)
\end{aligned}
\tag{A.62}
$$

The third integral is given by

$$
C^{\mp}(x) = -\frac{1}{2\pi} \int (2(x^\star)^3 - (x^\star)^2)\frac{2}{1-\beta y}\sqrt{1 - (y^\star)^2}\, dy,
\tag{A.63}
$$

which does not have a straight forward analytic solution. To handle this integration, as well as the more complicated muon and rho decays, a numerical Monte Carlo integration technique is employed. Decay events are generated with uniform probability in the tau rest frame variables $(x^\star, y^\star)$, and each event is assigned a weight equal to the matrix element of interest from Equation A.37. These weights are then accumulated into a histogram as a function of the lab frame variable x. After normalizing by the total number of events generated, the population of each bin is equal to the mean value of the lab frame function over that range of x.

Combining the two analytic integrals gives the decay matrix for a massless leptonic decay in the limit as $\beta \to 1$

$$
\mathcal{D}^{\mp}(x, \phi) = \frac{1}{2\pi} \begin{pmatrix} (2 - 6x^2 + 4x^3) & - \\ - & (\frac{4}{3} - \frac{4}{3}x^3) \end{pmatrix},
\tag{A.64}
$$

where these diagonal elements agree with the well known Michel spectrum for the two longitudinal tau spin states. The numeric solution for the off-diagonal element is shown in Figure A-3, along with the numerically integrated diagonal elements, which agree well with the analytic functions listed above.
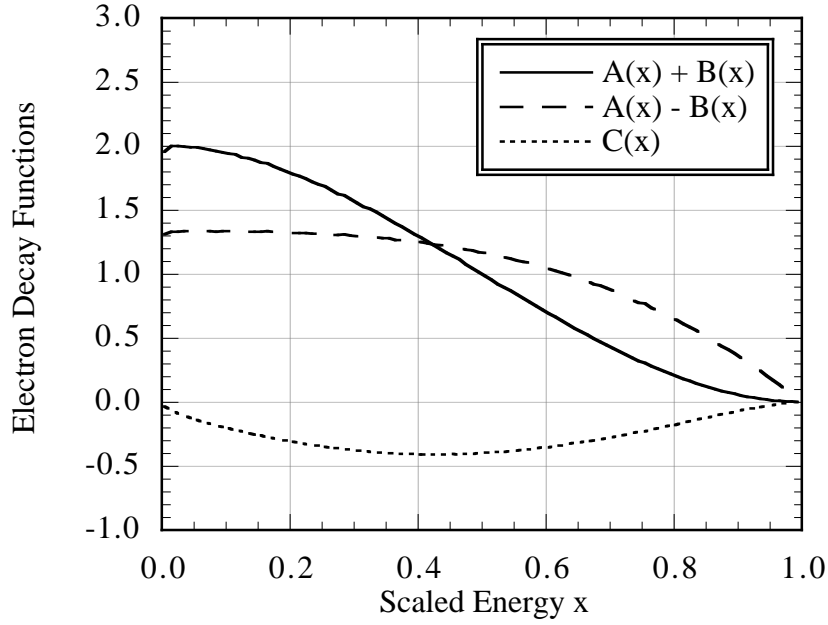
Figure A-3: The electron decay functions $A(x)+B(x)$, $A(x)-B(x)$, and $C(x)$ are shown after a change of variables into the lab frame by the numerical integration technique described in the text.

A.2.7   Muon Decay

For the leptonic decay $\tau^- \to \mu^- \bar{\nu}_\mu \nu_\tau$, the mass of the final state particle can no longer be ignored. From Tsai, the decay functions are given by

$$f_\mu(\mathbf{q}^\star) = \frac{1}{2\pi} \left[(x^\star)^2 - 4\frac{m_\mu^2}{m_\tau^2} \right] \left[3 - 2x^\star + \frac{m_\mu^2}{m_\tau^2} \left(3 - 4\frac{1}{x^\star} \right) \right] \qquad (A.65)$$

$$g_\mu(\mathbf{q}^\star) = \frac{1}{2\pi} \left[(x^\star)^2 - 4\frac{m_\mu^2}{m_\tau^2} \right] \left[1 - 2x^\star + 3\frac{m_\mu^2}{m_\tau^2} \right] \frac{p^\star}{E^\star} \qquad (A.66)$$

which reduces to the electron result as $(m_\mu/m_\tau) \to 0$. The factor $p^\star/E^\star$ can be written in terms of $x^\star$ as

$$\frac{p^\star}{E^\star} = \sqrt{1 - \left(\frac{2}{x^\star} \right)^2 \frac{m_\mu^2}{m_\tau^2}}. \qquad (A.67)$$
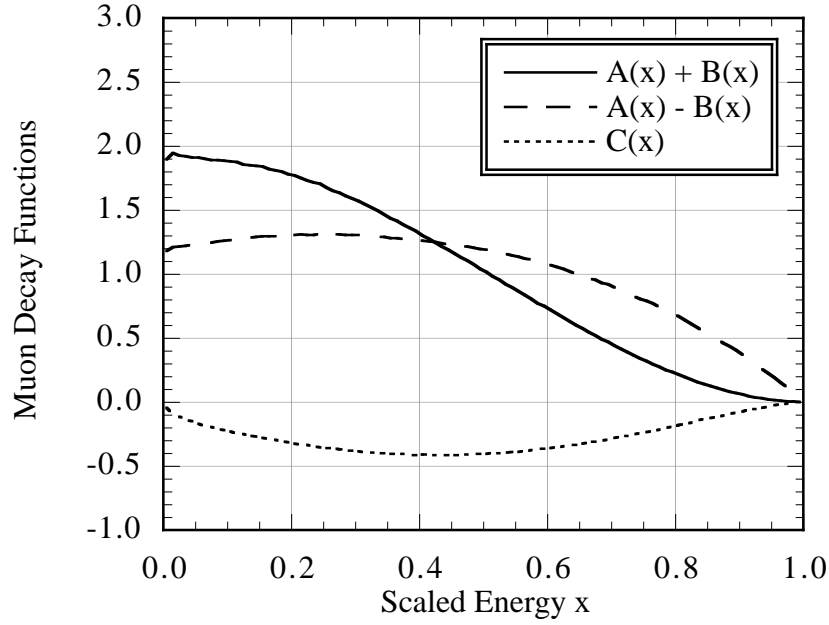
Figure A-4: The muon decay functions $A(x) + B(x)$, $A(x) - B(x)$, and $C(x)$ are shown after a change of variables into the lab frame.

The possible values of $x^\star$ are bounded by

$$x_{lo}^\star = 2\frac{m_\mu}{m_\tau} \qquad x_{hi}^\star = 1 + \frac{m_\mu^2}{m_\tau^2}, \tag{A.68}$$

and the numerically integrated matrix functions are shown in Figure A-4.

A.2.8   Rho Decay

The hadronic decay mode $\tau^- \rightarrow \pi^- \pi^0 \nu_\tau$ is dominated by the rather broad rho resonance. The decay functions listed in Tsai are computed in the narrow width approximation and are given by[2]

$$f_\rho(\mathbf{q}^\star) = \frac{1}{2\pi}\left\{\left[x^\star - \frac{1}{2}\left(1 + \frac{m_\rho^2}{m_\tau^2}\right)\right]^2 + \frac{m_\rho^2}{4m_\tau^2}\left[1 - 4\frac{m_\pi^2}{m_\rho^2}\right]\left[1 - \frac{m_\rho^2}{m_\tau^2}\right]\right\} \tag{A.69}$$

---

[2] The function printed in the original Tsai article was incorrect, and was revised in the erratum.

$$g_\rho(\mathbf{q}^\star) = \frac{1}{2\pi} \left\{ \left[x^\star - \frac{1}{2}\left(1 + \frac{m_\rho^2}{m_\tau^2}\right) \right]^2 + \frac{m_\rho^2}{4m_\tau^2}\left[1 - 4\frac{m_\pi^2}{m_\rho^2}\right]\left[3 - \frac{m_\rho^2}{m_\tau^2}\right] \right. \\ \left. - \frac{1}{2x^\star}\left[\frac{m_\rho^2}{m_\tau^2} - 4\frac{m_\pi^2}{m_\tau^2}\right] \right\} \frac{E^\star}{p^\star}, \tag{A.70}$$

where $x^\star$ is the scaled energy of the π^-, not the ρ^-. Again, the factor $p^\star/E^\star$ can be written in terms of $x^\star$ as

$$\frac{p^\star}{E^\star} = \sqrt{1 - \left(\frac{2}{x^\star}\right)^2 \frac{m_\pi^2}{m_\tau^2}}. \tag{A.71}$$

To incorporate the width of the rho resonance, the Q^2 of the rho decay process is distributed according to a Breit-Wigner by smearing the value of m_ρ used in the equations above. This gives satisfactory, although not exact, agreement with the predicted left and right handed decay distributions predicted by the Tau decay package `TAUOLA`.[3] This difference contributes to the systematic uncertainty assigned to the rho decay modeling.

---

[3] `TAUOLA` is a package for simulating tau lepton decays used in the `KORALZ` Monte Carlo generator. Unfortunately, the current version of `KORALZ` does not allow for transverse polarizations, or hemisphere spin correlations. The decay distributions generated for purely longitudinal tau polarizations are, however, quite accurate. Details can be found in
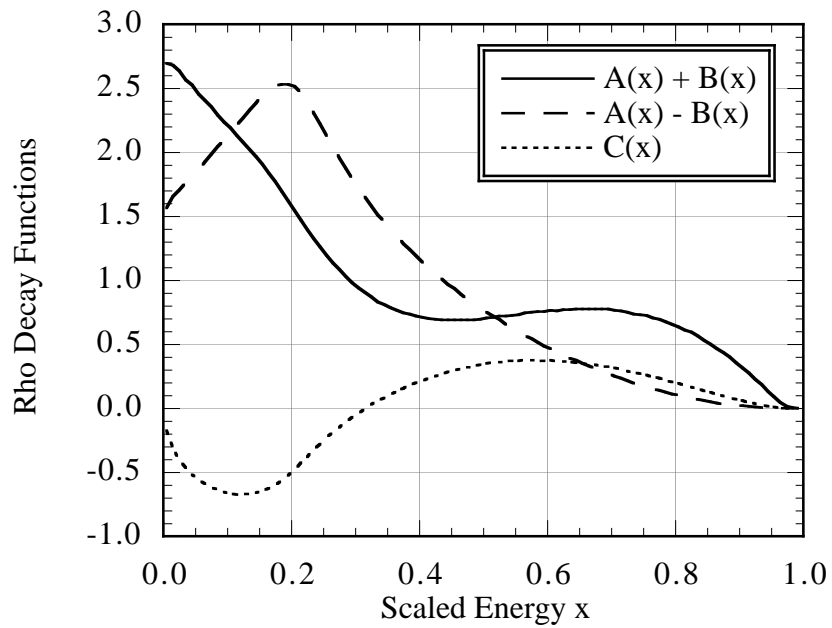
Figure A-5: The rho decay functions are shown in the lab frame. The curves show the
result of the numerical integration technique including the width of the rho
resonance.

Compton Cherenkov Detector Simulation

This appendix describes the Monte Carlo simulation of the Compton Cherenkov Detector (CKV). Based on the EGS4 electromagnetic shower package, this simulation has been greatly expanded in detail and scope for the 1994-95 run in an attempt to improve the accuracy of the detector calibration. A detailed computer model of the detector response is needed to correctly account for a small but non-negligible smearing of the acceptance in each detector channel. This smearing, which contributes roughly a one percent correction to the calculated analyzing powers, is due primarily to a lead pre-radiator placed in front of the detector to improve the signal to noise ratio.

In general, an attempt has been made to simulate every aspect of the detection process from the original electron bunch through to the transmission of the Cherenkov photons in the detector. As with any Monte Carlo simulation a decision has to be made as to when a detail is too fine to warrant inclusion, and in some cases there is simply not enough knowledge to construct an accurate model. In many cases, the actual effect of adding some new detail was not known beforehand, and only in retrospect does it turn out to be unimportant.

Section B.1 describes the basic theory behind the analyzing power calculations

and the framework of the simulation. Sections B.2 and B.3 describe the modeling of
the electrons themselves from the SLD interaction point where they are generated,
through the $e^-\gamma$ scattering process, and into the spectrometer elements of the po-
larimeter system. Section B.4 covers the geometry of the detector as described to
the EGS shower package which simulates the interactions of these electrons in the
detector and surrounding material. Simulation of the actual Cherenkov process and
the transmission of the light to the Photomultiplier tubes is covered in Section B.5,
while some of the actual results are detailed in Section B.6. A final note on the code
itself will be found in Section B.7.

B.1   Compton Scattering Theory

The cross section for Compton scattering, more fully developed in Chapter 3, can
be written in terms of an unpolarized cross section $d\sigma_0$ and an asymmetry function
A as

$$d\sigma(x) = d\sigma_0(x)\left[1 + \mathcal{P}A(x)\right] \tag{B.1}$$

where the kinematic variable $x = K'/K'_{\mathrm{max}}$ is the fractional energy of the scattered
Compton photon in the lab frame, and $\mathcal{P}$ is the longitudinal polarization product.
In the Compton polarimeter system, a spectrometer is used to momentum analyze
the scattered electrons, and the spatial variation of the cross section is measured in
the multi-channel CKV detector. The analyzing power for a particular channel a^i
can be written as

$$a^i = \frac{\int A(x)\mathcal{R}^i(x)\frac{d\sigma_0}{dx}dx}{\int R^i(x)\frac{d\sigma_0}{dx}dx} \tag{B.2}$$

where $\mathcal{R}^i(x)$ is the detector response function function for that channel. Equa-
tion B.2 shows that knowledge of the absolute response of each of the channels is

not necessary since $\mathcal{R}^i$ appears in both the numerator and the denominator.

The integrals in Equation B.2 can be carried out over either position or energy, although in this case the response is more naturally thought of as a function of position. In writing the asymmetry function $A(x)$ in terms of position, it is assumed that the transformation function representing the effect of the spectrometer is known. This same transformation function also enters into the Jacobian needed to convert the $\frac{d\sigma_0}{dx}$ term. Because the incoming electron beam has finite spatial width and angular divergence, as well as non-zero energy divergence, this transformation is in principle not a simple one-to-one mapping of energy to position, but depends upon the exact trajectory of each individual electron. In fact, the center of mass energy of the collision is smeared by the beam energy divergence, and should be convoluted into Equation B.2 as well.

One way to tackle this problem is to use the simulation itself to do the entire calculation, tabulating not only the response, but the exact cross section and asymmetry of each electron generated, thereby allowing an exact calculation of the analyzing powers for each channel. For most cases, the cost in computational time makes this sort of approach prohibitive, especially when the results are to be used in a fitting procedure. A second method is to use the full simulation to produce a response function with all smearing taken in to account, and then integrate these response functions against the analytic expressions for the cross section and asymmetry. The same spectrometer model is used in both techniques, the only approximation being made is that the complicated energy to position relationship can be approximated without bias by an analytic function representing the trajectory of the beam centroid. This turns out to be a good approximation, and further results will be deferred until Section B.6.

B.2   Electron Simulation

Photons from the Compton Laser collide with the outgoing electron beam in the South Final Focus immediately before the first dipole bend magnet of the South Arc. In order to accurately simulate the spatial and angular divergence of the target electrons at the collision point, a first order beam transport matrix is used to estimate the electron beam transport from the SLD Interaction Point to the Compton Interaction Point (CIP). The matrix is derived from a Transport simulation of the SFF beam elements.[67] In general, the transport matrix T operates on a vector of beam parameters

$$\vec{\mathbf{x}} = \begin{pmatrix} x \\ x' \\ y \\ y' \\ E \end{pmatrix}$$

where x' is the angular deflection and x is the spatial displacement from the central or design trajectory. This vector can either represent an individual electron or a beam envelope describing an entire ensemble, however in this simulation $\vec{\mathbf{x}}$ always represents a single electron. In the SFF between the SLD and the CIP, all of the beam control elements are orthogonal to first order leading to a decoupling of the x and y coordinates. The beam transport matrix can then be parameterized as

$$\begin{pmatrix} x \\ x' \end{pmatrix}_{\text{CIP}} = \begin{pmatrix} T_{xx} & T_{xx'} \\ T_{x'x} & T_{x'x'} \end{pmatrix} \begin{pmatrix} x \\ x' \end{pmatrix}_{\text{SLD}} \tag{B.3}$$

$$\begin{pmatrix} y \\ y' \end{pmatrix}_{\text{CIP}} = \begin{pmatrix} T_{yy} & T_{yy'} \\ T_{y'y} & T_{y'y'} \end{pmatrix} \begin{pmatrix} y \\ y' \end{pmatrix}_{\text{SLD}}, \tag{B.4}$$

Table B.1: Beam Transport Matrix Elements

Parameter	Value
T_{xx}	-4.2240
$T_{x'x'}$	-0.2685
$T_{xx'}$	1.7692 μm/μRad
$T_{x'x}$	0.0757 μRad/μm
T_{yy}	-5.7817
$T_{y'y'}$	-0.1148
$T_{yy'}$	0.9752 μm/μRad
$T_{y'y}$	-0.3450 μRad/μm

where these values are listed in Table B.1. The beam parameters at the CIP are entirely dominated by the beam divergence at the SLD IP. The small micron-level spot sizes can be accurately approximated as zero, further reducing the matrix T to only four significant parameters. The electrons are generated with an elliptical gaussian distribution of divergence angles at the SLD IP and 'transported' to the CIP by means of the transport matrix T. This distribution has a projective half width of 300 μRad in x and 200 μRad in y, and is assumed to be uncorrelated between the two axes at the SLD IP.

The resulting one sigma beam parameters at the Compton IP are shown in Table B.2. The incident laser spot is estimated to be at least a few times larger than the electron bunch, and no additional spatial convolution is made to simulate the $e^- \gamma$ collision. To first order the SFF is achromatic between the SLD and the CIP, and thus there is no energy dependence to the spatial distributions at the CIP. The Compton scattering angle in the lab frame is on the order of 10 microradians, which is small compared to the natural divergence of the beam at the CIP. For this reason, no attempt has been made to add any additional energy dependent angular divergence to simulate the scattering process. It will be shown in Section B.6 that the simulated analyzing powers are actually quite insensitive to the details of the electron spot.

Table B.2: Compton IP Electron Beam Parameters

Parameter	Value
σ_x	530 μm
σ_y	195 μm
$\sigma_{x'}$	80 μRad
$\sigma_{y'}$	23 μRad

Beam spot size and divergence angles are shown at the CIP assuming a 300 μRad by 200 μRad spot size at the SLD IP. The position and angle for each coordinate are completely correlated, although there is assumed to be no correlation between the two axes.

In order to give each channel of the CKV adequate statistics, the scattered electron energy is selected to produce a roughly flat distribution of particles across the face of the detector. The unpolarized cross section and asymmetry function are calculated for each electron to be accumulated along with the eventual detector response, so no Monte Carlo simulation of the absolute cross section is necessary.

B.3   Spectrometer

After interacting with the Compton Laser, the scattered electrons are swept out of the main electron beam by a series of magnets shown schematically in Figure B-1. The equations of motion for an electron of known energy through these magnets is calculated analytically in the Turtle ray tracing package,[68] and is used in this simulation to determine the exact trajectory of each electron into the detector. Table B.3 shows the default parameters used to characterize this effective spectrometer for a 50 GeV design energy electron. The actual magnet strengths used in the simulation are scaled down from these values by the actual beam energy which is fixed to be 45.6 GeV.

This spectrometer model is exact up to higher order field components such as fringing fields at the dipole faces, which have been neglected. In general, any small
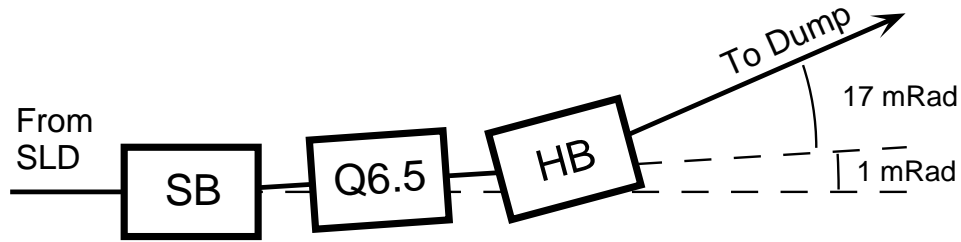
Figure B-1: The block diagram of spectrometer elements is shown with deflection angles for the on-energy beam.

Table B.3: Spectrometer Parameters

Element	Length	Field	Half Aperture
SB	4.00272 m	0.41667 kGauss	
Drift	0.26649 m		
Q6.5	1.27033 m	12.0 kGauss	5.0 cm
Drift	0.99127 m		
HB	2.30418 m	12.5 kGauss	

Magnet strengths listed are for the 50 GeV design momentum. The quadrupole is defocusing in the horizontal plane.

error made in the absolute scale of the dipole field simulated by the model will be corrected for by the complete calibration procedure. The addition of the quadrupole Q6.5 for the 1994-95 SLD run has made the spectrometer model a much more complex analytic function, and has added a few more parameters to the model itself, but in principle it has not changed the overall function of the spectrometer in the simulation.

Up to this point in the simulation, the electrons have been described in the co-ordinates of the Transport equations which are deviations from a design or central energy ray particle. The last step in the electron beam simulation is to make a co-ordinate transformation into the system used to describe the detector geometry to the EGS4 shower simulation package. This transformation is straightforward provided one knows where the on energy electron beam is in relation to the Cherenkov
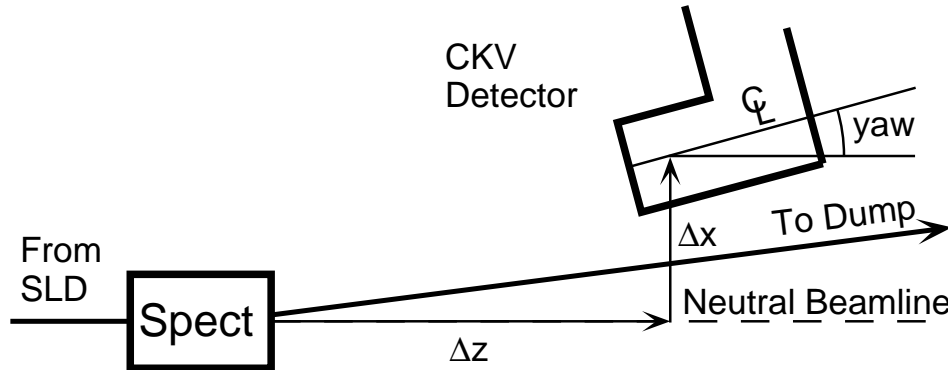
Figure B-2: The orientation of the CKV detector is defined with respect to the neutral beamline. The front face of channel 5 along the detector centerline is used as the reference point.

detector itself. Since this can vary with different beam energies and magnet settings, the location of the Cherenkov detector is defined with respect to the neutral or undeflected beamline, and the spectrometer model itself is used to calculate the location of the nominal energy electron beam.

There are three angles and three distances which completely describe the position of the Cherenkov detector with respect to the neutral beamline. Of these, the vertical displacement and pitch, along with the roll of the detector are all assumed to be zero, and are constrained to be nearly so by survey data taken during detector installation and removal. The remaining three parameters, shown in Figure B-2, are the longitudinal distance along the neutral beamline, the transverse distance away from the neutral beamline, and the yaw of the detector centerline. The front face of channel 5 along the detector centerline is used as the detector orientation reference point. The transverse orientation of the detector is essentially what the calibration process determines, while the other two parameters are fixed in the simulation to their surveyed values. The calibrated analyzing powers are actually quite insensitive to variations in these two final parameters.

With this transformation the incident electron simulation is complete and the EGS shower simulation package is called to do the real computational work of the

Table B.4: CKV Detector Survey Values

Parameter	Survey Value
Pitch	-1.2 mRad
Roll	-0.2 mRad
Yaw	44.5 mRad
Δx	16.140 cm
Δy	0.149 cm
Δz	211.915 cm

Δx is determined by the calibration procedure; this represents a typical value. Survey data was taken March 14, 1994.

simulation.

B.4   Detector Geometry

The EGS4 code package is used to simulate the interactions of the high energy electrons with the CKV detector and surrounding material.[44] The CKV detector is described to the EGS package by a planar geometry consisting of approximately 100 planes and over 200 distinct regions. The detail of this geometry can be seen in Figure B-4. Along with a full description of the detector itself, the model includes the lead preradiator and beampipe flange in front of the detector, as well as the beampipe itself and an assortment of material on the other side of the beampipe where the backscattered Compton photon will interact.

The head of the detector has a fairly complicated geometry reflecting the projective nature of the detector channels. To facilitate detector assembly, the thin walls of each channel are sandwiched between aluminum spacer plates which define the floor and ceiling of the channel volume. Each plate has an identical angular extent, and is staggered longitudinally in the detector by a fixed amount from its neighbor. This entire assembly is kept in place by a pair of press bars providing compression from either side. Since the dimensions of the spacer plates are well known
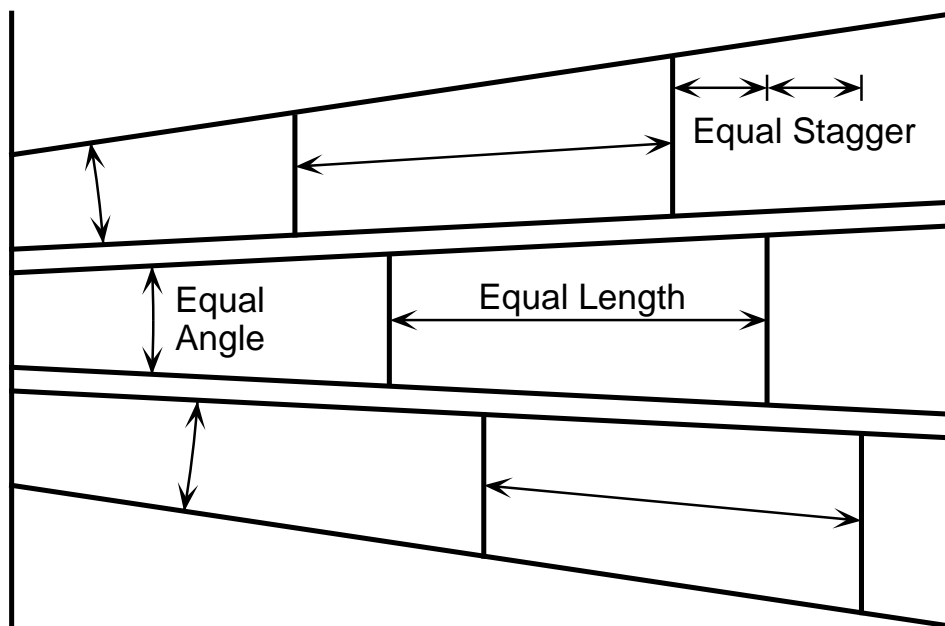
Figure B-3: The channel wall geometry as defined by the spacer bars is schematically
shown. Every spacer bar subtends an equal angle, has equal length along
its centerline, and is offset by an equal amount in the longitudinal direction.
These three parameters along with the channel wall thickness completely
determine the channel wall geometry.

from fabrication drawings, the simulation code uses this information to construct
the detector geometry at run time in much the same way the detector is physically
assembled. As shown in Figure B-3, the planes defining the walls of each channel
are computed by stacking the spacer plates sequentially outward from the central
channel. This technique has greatly simplified the parameterization of the detector
head geometry, while allowing for the study of things like machining tolerances on
the calculated analyzing powers.

The smearing of the response functions is primarily due to the presence of ma-
terial upstream from the detector. Two removable lead sheets which are used as a
pre-radiator provide 6.86 mm $(1.22X_0)$ of material during normal operating condi-
tions. There is also 2.78 mm $(0.03X_0)$ of aluminum from the front of the vacuum
can which contains the CKV detector gas volume. The electrons exit the SLD vac-

uum through a thin stainless steel window which is assumed to have no significant effect, and is not modeled. As a result of problems seen during the 1993 run, an attempt has been made to accurately simulate all material near the beampipe which might scatter electrons into the detector volume. As seen in Figure B-4, this material includes the beampipe itself, the flange holding the SLC exit window, and the aluminum side wall of the CKV vacuum can. In Section B.6, it will be shown that while this extra beampipe material can make a substantial difference to the asymmetry observed in the inner channels, the effect of this material is negligible in Channel 7. Other material included in the simulation include the stainless steel blocks used as 45 degree mirrors, the aluminum press bars and spacer plates which define the floor and ceiling of the channel volume, and a chunk of lead immediately behind the detector which simulates the PTD detector. None of this extra material has an observable effect on the simulated analyzing powers or detector response. No attempt has been made to simulate showering in the actual detector gas itself. A vacuum is assumed in all regions which are not filled with solid material.

B.5   Cherenkov Photon Production

The production and transport of the Cherenkov light in the CKV detector is modeled for the nine regions representing the channels in the detector head, as well as in nine additional regions representing the transverse light guides. In principle, Cherenkov light is produced everywhere inside the detector, but small aluminum covers at the front of each channel keeps this stray light from reaching the Photomultiplier tubes. The simulation of the Cherenkov process was originally developed by Rob Elia for the 1992 run, and has survived mostly unchanged since then. The Cherenkov production threshold for propane at 1 atmosphere is roughly 10 MeV. The exact value used directly effects the width of the simulated response function, and a number of cross checks on the shape of the response function constrain this quantity to be good to
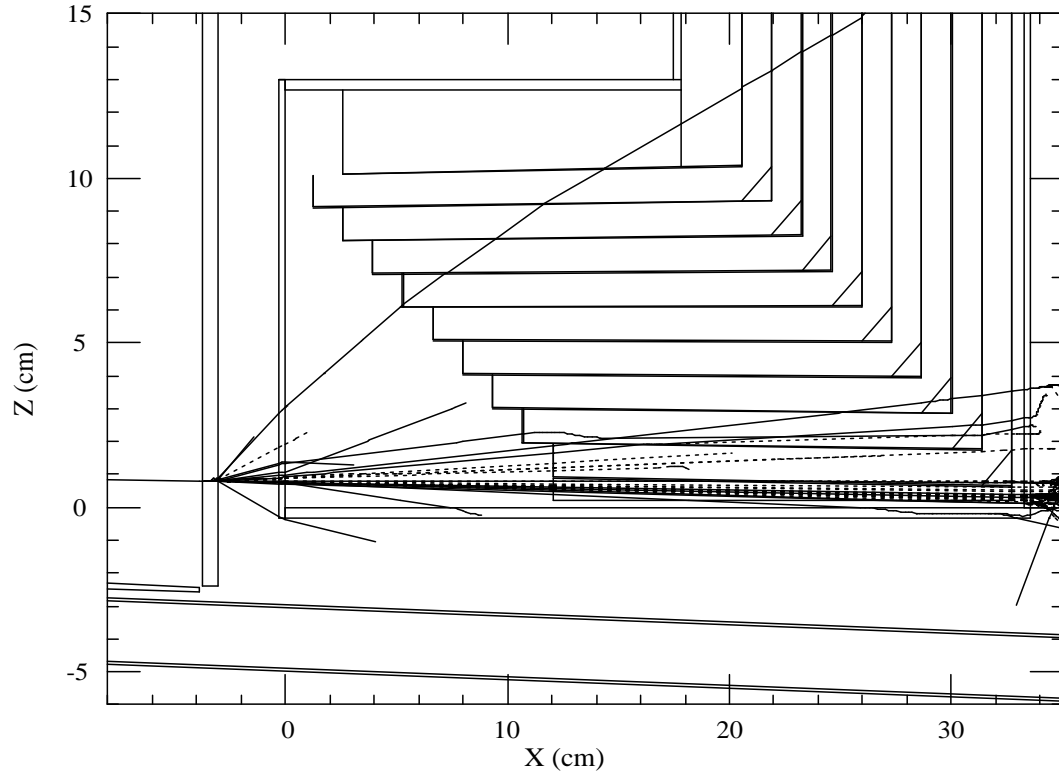
Figure B-4: An EGS4 simulation of a single electron showering in the CKV detector is shown.

roughly ± 2 MeV. Every charged particle transported through one of the sixteen active detector regions radiates Cherenkov photons in this simulation. The number of Cherenkov photons produced per unit length is given by

$$
n(E) = n_0 \sin^2 \theta
$$

$$
= 2215.1/\text{cm} \times \sin^2 \theta_{\max} \frac{E^2 - E_{\min}^2}{E^2 - m_e^2} \tag{B.5}
$$

where

$$\sin^2 \theta_{\max} = m_e^2 / E_{\min}^2 \tag{B.6}$$

and the normalization factor n_0 corresponds to a production energy range from 2 - 8 eV. Given the assumption that $E_{\min} = 10$ MeV, the maximum production angle $\theta_{\max} = 51$ mRad and the Cherenkov production per unit length $n(E) \approx 5.8$/cm as $\beta \to 1$.

The produced photons are generated randomly along the length of the track and with a uniform distribution in azimuth about the charged track. The opening angle θ between the photon and charged track depends on the energy of the charged track as shown in Equation B.5. To save processing time, the transmission of the Cherenkov light is not simulated, but rather a probability function $P(z^\star, \phi^\star, \theta^\star)$ is calculated beforehand and used as a lookup table. The three coordinates $z^\star, \phi^\star,$ and $\theta^\star$ are the longitudinal distance from the start of the channel, the azimuthal direction of the photon, and the polar angle of the photon from the individual channel center line. There is only one function P used for all nine channels.

The function P is generated by simulating the reflections of the Cherenkov photons down the mirrored aluminum light guides, and off the two 45 degree mirrors. Photons are generated over the full useful range of the $z^\star, \phi^\star,$ and $\theta^\star$ parameters, and the reflectivity of the photons off the aluminum surfaces is calculated for each ray as a function of the incident angle and photon energy using the Fresnel equations. The calculated reflectivity is then normalized separately for both the 45 degree blocks and the grazing incidence from the channel walls to agree more closely with direct measurements made with a mercury lamp. Each photon orientation is simulated multiple times with a flat distribution in energy from 2 - 8 eV, and the transmission is combined with the expected quantum efficiency of the photocathode shown in Figure B-5 to provide the net probability of a photoelectron being produced. The
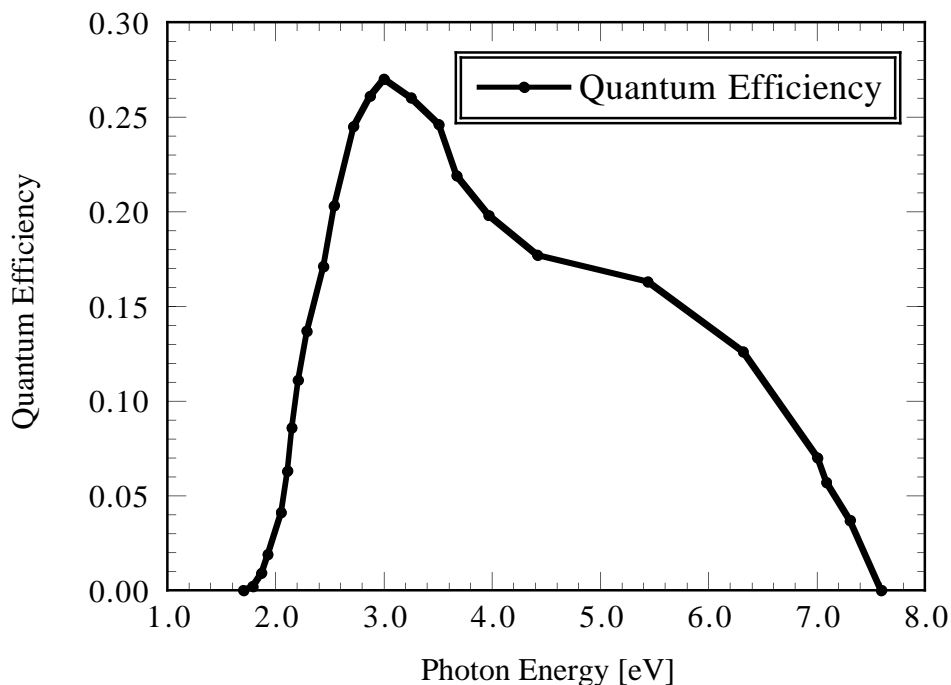
Figure B-5: The Quantum Efficiency as a function of incident photon energy as used in the detector simulation is shown for the Hammamatsu R1398 photomultiplier tube.

actual value returned by the function P is therefore integrated over a flat photon energy spectrum with the energy dependence of the photocathode and the reflectivity taken into account. No attempt has been made to simulate the absorption of photons in the gas, nor has the polarization of the Cherenkov light been taken into account.

It is known that there must be some scintillation of charged particles below the 10 MeV Cherenkov threshold in the detector gas, and scintillation may account for much of the beam related background seen by the CKV detector during normal operations. Some measurements of the scintillation properties of propane have been made by LBL, and the expected rate of photoelectrons produced from scintillation is expected to be insignificant compared to the rate from direct Cherenkov production. A direct simulation, however, has never been attempted. Under the assumption that scintillation from signal electrons will be isotropic throughout the volume of
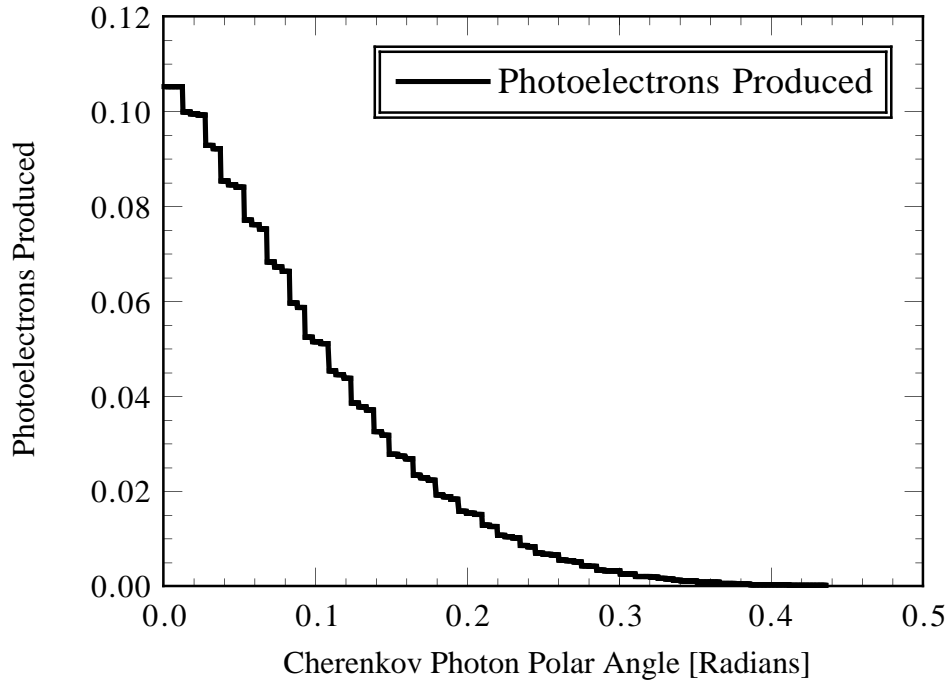
Figure B-6: The transmission probability of a Cherenkov photon at a fixed position $z^\star$ and fixed azimuthal angle $\phi^\star$ is shown as a function of the polar angle $\theta^\star$ with respect to the channel centerline. The step changes in the probability arise from the discrete change in the number of reflections required to reach the PMT. The QE of the photocathode has been folded into this curve.

the detector, the result will be a uniform increase in the response of each channel. This increase will only be significant in the far tails of the response functions, and this sort of contamination has been explicitly constrained by cross checks performed during the calibration procedure.

During the 1995 running period, a lead preradiator for the BSM counter was stuck in the neutral beamline across from the CKV detector. Data was taken in this configuration for approximately 10 days, and a statistically significant dilution of the compton asymmetry was seen as a result in Channel 8. An attempt was made to expand the CKV detector model to simulate this effect by tracking the backscattered photons from the Compton scattering process as well as the electrons. It is expected that any showering from this material would be unable to

make it into the detector head, but rather might find itself into the long transverse transport lines which reflect the Cherenkov light back to the photomultiplier tubes. For this reason, the simulation of the Cherenkov light production was expanded to include these transverse detector regions. A fairly accurate simulation of the material present on the neutral beamline was undertaken from recent drawings made of this region, however no significant amount of signal was seen in the CKV detector from these sources. There are a number of possible reasons to explain this apparent discrepancy between the data and EGS simulation. First, it is possible that the EGS modeling of wide angle and second order scattering is simply not correct. Second, it is possible that the simulation of the neutral beamline material is missing something important. Third, it is possible that the neutral beamline signal is coming mostly from scintillation which is not modeled, rather than direct Cherenkov production. Fourth, it is possible that the effect seen in the data is actually a linearity problem resulting from significantly higher backgrounds during the BSM era, and not an actual change in the asymmetry at all. At the present time, there are no concrete reasons to rule out any of the above possibilities, and the correction applied to the analyzing powers during the BSM period carry a 100% systematic error.

B.6   Results

For every incident electron generated, the total number of photoelectrons produced in each of the nine CKV channels is determined by the EGS shower simulation. These nine responses, along with the unpolarized cross section and the asymmetry function, are histogrammed as a function of the incident electron trajectory where it would have crossed the plane perpendicular to the neutral beamline intersecting the front of Channel 5 if the detector were not present. The bin size used is adjustable, although a bin size of 100 μm was used for most of the Monte Carlo generated. This data is written out bin by bin to an external file so that the information can be
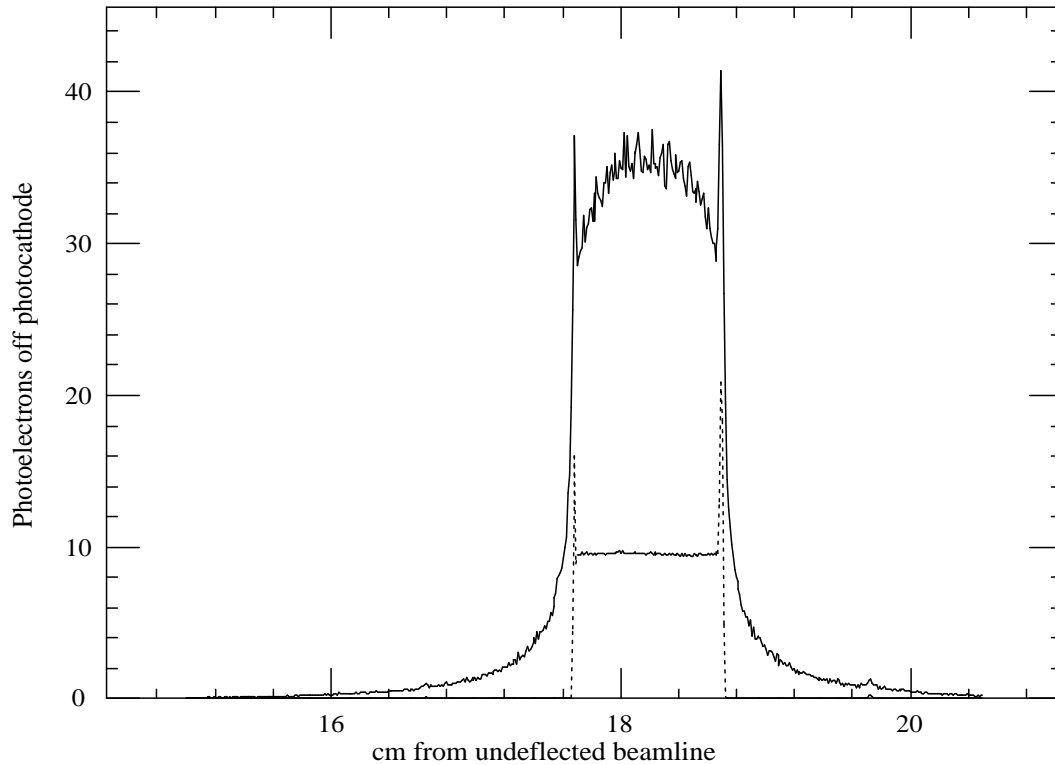
Figure B-7: The EGS generated response function for Channel 7 is shown both with and without the $\sim 3/10$ inch lead pre-radiator. The amplification in the signal size can be clearly seen, as well as the long tails resulting from showering in the pre-radiator.

easily accessed and manipulated at a later date. An example of a response function for Channel 7 is shown in Figure B-7.

During the course of a Monte Carlo run, both the response sums and sums-squared are accumulated allowing an estimate of the statistical error in the calculated analyzing power to be made. The statistical error in one bin is derived from the variance of the mean response in that bin, and is taken to be uncorrelated with all other bins. This is probably only a good approximation in the heart of a detector channel where the number of photoelectrons produced is high, however this

region dominates the determination of the analyzing power. Since this error does not actually enter into the calculation of the analyzing power, but rather is used as a rough guide to the statistical significance of any observed result, it does not have to be exactly correct. As a check a set of ten runs were generated with different initial random number seeds, and it was verified that the distribution of the calculated analyzing powers followed a gaussian distribution with a width equal to that predicted by the computed error. A further discussion of the handling of random numbers will be deferred until Section B.7.

The detector simulation is set up so that a single run can generate one set of response functions, or some sort of scan can be made to calculate a series of response functions while a model parameter is changed. This has proved most useful in simulating the response and analyzing power changes during the course of a table scan, which is the primary tool used in the calibration procedure. Other checks have been made by changing the relative position of the beam in the spectrometer quadrupole field, simulating a mis-alignment of this beam element or relative beam motion in the SFF.

The remainder of this section will be devoted to a number of studies of the EGS simulation itself. These studies compare the analyzing powers generated with different input parameter sets. It should be noted that the EGS Monte Carlo alone does not determine the final analyzing powers used in the polarization measurement, but rather must be combined with the calibration procedure and a time dependent tracking of the analyzing powers between calibration points. Different parameter sets have been compared here with a default configuration based on the average table position found during with the detector calibration procedure. These analyzing powers are 'typical' for the run, and agree with the actual calibrated analyzing powers for Channel 7 to within $\sim 0.2\%$, but do not directly correspond to the calibrated analyzing powers used in the polarization measurement. In general, the effect of any parameter which changes the position of the edge with respect to the

detector will largely be taken out by the calibration procedure. The obvious example is the transverse detector position, but even things like the width of the detector channels and the displacement of the electron beam through the spectrometer will produce a smaller change in the calibrated analyzing powers than the raw change indicated by the simulation. For this reason, all comparisons shown here should be taken as an upper limit on the possible size of any effect seen; the true effect can only be determined by completing the full calibration procedure.

As was mentioned in Section B.1, there could be a difference in the analyzing power calculation between integrating the response function against the analytic cross sections, and using the full blown binned calculation with all beam smearing effects explicitly taken into account. Table B.5 shows the effect of the beam size on the analyzing powers is insignificant, and in practice the results from the two different calculations are observed to vary by no more than $\sim 2 \ 10^{-5}$.

While the lead preradiator has a significant effect on the signal seen in a given CKV channel, the effect on the analyzing power is actually fairly small. Table B.6 shows the change in analyzing powers for the three commonly used lead configurations used for cross checks during the 1994-95 run. A change of $\sim 1\%$ can be seen in the Channel 7 analyzing power when the lead preradiator is completely removed.

Electron showering in the material beside the CKV detector has always been something of a problem. Since the electrons which hit this material have a lower asymmetry than the electrons directly incident on a channel, any signal picked up by the photomultiplier tubes from these sources amounts to a dilution of the observed asymmetry. Table B.7 shows the difference in the analyzing powers seen when the beampipe, exit window flange, and CKV vacuum can side wall are turned off in the simulation. Since the accuracy of the EGS simulation of high angle scattering could possibly be questioned, it is comforting to see that the effect of this extra material is confined to the inner three channels.

Table B.5: Analyzing Power Dependence on Electron Spot Size

Channel Number	Default AP	No Divergence Δ AP
1	-0.04905(12)	-0.00004(17)
2	0.11092(14)	-0.00020(19)
3	0.27261(13)	+0.00018(18)
4	0.41919(11)	-0.00013(16)
5	0.54146(9)	+0.00004(13)
6	0.63937(7)	-0.00004(10)
7	0.70962(5)	+0.00003(8)
8	0.70816(29)	+0.00002(36)
9	0.69253(68)	+0.00068(84)

The change in analyzing powers is shown when the simulation of the beam width and energy divergence is turned off. No significant effect is seen.

Table B.6: Analyzing Power Dependence on Preradiator Thickness

Channel Number	0.27 inch AP	0.18 inch Δ AP	0.09 inch Δ AP	0.00 inch Δ AP
1	-0.04905(12)	-0.00120(18)	-0.00316(19)	-0.00337(17)
2	0.11092(14)	+0.00061(20)	+0.00074(21)	+0.00101(19)
3	0.27261(13)	+0.00150(19)	+0.00269(20)	+0.00328(18)
4	0.41919(11)	+0.00159(17)	+0.00324(17)	+0.00395(15)
5	0.54146(9)	+0.00137(13)	+0.00336(14)	+0.00418(12)
6	0.63937(7)	+0.00177(11)	+0.00343(11)	+0.00470(10)
7	0.70962(5)	+0.00240(8)	+0.00484(8)	+0.00665(7)
8	0.70816(29)	+0.00232(40)	+0.00106(114)	-0.14477(3029)

Analyzing powers are shown for the default 0.27 inch preradiator configuration. The differences in analyzing powers for smaller preradiators are also shown.

Table B.7: Analyzing Power Dependence on Beamline Material

Channel Number	Default AP	No Material Δ AP
1	-0.04905(12)	+0.00695(17)
2	0.11092(14)	+0.00264(19)
3	0.27261(13)	+0.00106(19)
4	0.41919(11)	+0.00010(16)
5	0.54146(9)	+0.00008(13)
6	0.63937(7)	-0.00014(10)
7	0.70962(5)	-0.00002(8)
8	0.70816(29)	+0.00031(36)
9	0.69253(68)	+0.00182(80)

The change in analyzing powers is shown due to turning off the simulation of the beampipe, exit window flange, and CKV vacuum can side wall. A clear effect is visible in the inner three CKV channels.

Table B.8: Analyzing Power Dependence on Detector Material

Channel Number	Al Walls AP	No Walls Δ AP	Pb Walls Δ AP
1	-0.04905(12)	-0.00083(17)	+0.00474(19)
2	0.11092(14)	-0.00078(19)	+0.00308(21)
3	0.27261(13)	-0.00013(19)	+0.00287(20)
4	0.41919(11)	-0.00058(16)	+0.00157(17)
5	0.54146(9)	-0.00015(13)	+0.00163(14)
6	0.63937(7)	-0.00021(10)	+0.00150(11)
7	0.70962(5)	+0.00011(8)	+0.00100(8)
8	0.70816(29)	+0.00362(35)	+0.00399(43)
9	0.69253(68)	+0.00085(129)	-0.00297(155)

The difference in analyzing powers is shown when the channel wall material is changed from the nominal aluminum. Differences for both no material and lead are significant, but even a gross misunderstanding of the wall material has a small effect on the analyzing power.

B.7   Code Notes

The Compton Cherenkov detector simulation is written in a combination of Mortran and vanilla Fortran compiled and run mostly on an Alpha 3000 at MIT. With the recent acquisition of SLACAX, it is not more efficient to run this code at SLAC, and the entire package has been copied from MIT to the directory

$$\texttt{DISK\$SLD\_AXP\_FAC} : [\texttt{EGS}]$$

on the SLACVX cluster.

The simulation code consists of a number of components. The complete EGS4 distribution is stored in the `[EGS.EGS4]`   directory with minor modifications from the distribution release to fix some floating point precision problems present on the Alpha platform. The user code is found in the `[EGS.COMPTON]`   directory and consists of separate routines to simulate the spectrometer (`TRANSPORT.FOR`) and the Cherenkov light production (`LOOKUPEFF.FOR`), as well as the main simulation code itself (`COMPTON95D.MOR`). The parameters used in the detector simulation are defined for each job in an input file. This file is read in by the simulation at the beginning of a run, and allows the same executable code to be used for a wide variety of cross checks and tests. An added benefit is that the exact parameter set used to generate a particular response function is readily available, and results can be reliably reproduced after weeks or even months.

Every Monte Carlo run of the detector simulation is generated with a unique random number seed. The EGS package consumes random numbers at a fairly voracious rate, and some problems were encountered finding a random number generator with a long enough period to prevent repetition. To generate the standard set of analyzing powers to the precision shown above required a simulation of 1 million incident electrons. This job, which took 10.5 hours of CPU time on SLACAX, generated over 19 billion random numbers. Very few commonly available random

number generators can produce this sort of series without repeating at least once. The actual routine used is `RANMAR` from the `CERNLIB` package. This routine, written by G. Marsaglia and A. Zaman, was chosen for its long (10^{43}) period and ease of use in setting and extracting the seed values. The period of this generator was verified to be greater than 10^{12} by a direct test.

Appendix C

The SLD Collaboration

K. Abe,[19] K. Abe,[29] I. Abt,[13] T. Akagi,[27] N.J. Allen,[4] W.W. Ash,[27]†
D. Aston,[27] K.G. Baird,[24] C. Baltay,[33] H.R. Band,[32] M.B. Barakat,[33]
G. Baranko,[9] O. Bardon,[15] T. Barklow,[27] G.L. Bashindzhagyan,[18]
A.O. Bazarko,[10] R. Ben-David,[33] A.C. Benvenuti,[2] G.M. Bilei,[22] D. Bisello,[21]
G. Blaylock,[6] J.R. Bogart,[27] T. Bolton,[10] G.R. Bower,[27] J.E. Brau,[20]
M. Breidenbach,[27] W.M. Bugg,[28] D. Burke,[27] T.H. Burnett,[31] P.N. Burrows,[15]
W. Busza,[15] A. Calcaterra,[12] D.O. Caldwell,[5] D. Calloway,[27] B. Camanzi,[11]
M. Carpinelli,[23] R. Cassell,[27] R. Castaldi,[23](a) A. Castro,[21] M. Cavalli-Sforza,[6]
A. Chou,[27] E. Church,[31] H.O. Cohn,[28] J.A. Coller,[3] V. Cook,[31] R. Cotton,[4]
R.F. Cowan,[15] D.G. Coyne,[6] G. Crawford,[27] A. D'Oliveira,[7] C.J.S. Damerell,[25]
M. Daoudi,[27] R. De Sangro,[12] P. De Simone,[12] R. Dell'Orso,[23] P.J. Dervan,[4]
M. Dima,[8] D.N. Dong,[15] P.Y.C. Du,[28] R. Dubois,[27] B.I. Eisenstein,[13] R. Elia,[27]
E. Etzion,[4] D. Falciai,[22] C. Fan,[9] M.J. Fero,[15] R. Frey,[20] K. Furuno,[20]
T. Gillman,[25] G. Gladding,[13] S. Gonzalez,[15] G.D. Hallewell,[27] E.L. Hart,[28]
A. Hasan,[4] Y. Hasegawa,[29] K. Hasuko,[29] S. Hedges,[3] S.S. Hertzbach,[16]
M.D. Hildreth,[27] J. Huber,[20] M.E. Huffer,[27] E.W. Hughes,[27] H. Hwang,[20]
Y. Iwasaki,[29] D.J. Jackson,[25] P. Jacques,[24] J. Jaros,[27] A.S. Johnson,[3]
J.R. Johnson,[32] R.A. Johnson,[7] T. Junk,[27] R. Kajikawa,[19] M. Kalelkar,[24]
H. J. Kang,[26] I. Karliner,[13] H. Kawahara,[27] H.W. Kendall,[15] Y. Kim,[26]
M.E. King,[27] R. King,[27] R.R. Kofler,[16] N.M. Krishna,[9] R.S. Kroeger,[17]
J.F. Labs,[27] M. Langston,[20] A. Lath,[15] J.A. Lauber,[9] D.W.G.S. Leith,[27]
V. Lia,[15] M.X. Liu,[33] X. Liu,[6] M. Loreti,[21] A. Lu,[5] H.L. Lynch,[27] J. Ma,[31]

G. Mancinelli,[22] S. Manly,[33] G. Mantovani,[22] T.W. Markiewicz,[27] T. Maruyama,[27]
R. Massetti,[22] H. Masuda,[27] E. Mazzucato,[11] A.K. McKemey,[4] B.T. Meadows,[7]
R. Messner,[27] P.M. Mockett,[31] K.C. Moffeit,[27] B. Mours,[27] D. Muller,[27]
T. Nagamine,[27] S. Narita,[29] U. Nauenberg,[9] H. Neal,[27] M. Nussbaum,[7]
Y. Ohnishi,[19] L.S. Osborne,[15] R.S. Panvini,[30] H. Park,[20] T.J. Pavel,[27]
I. Peruzzi,[12][b] M. Piccolo,[12] L. Piemontese,[11] E. Pieroni,[23] K.T. Pitts,[20]
R.J. Plano,[24] R. Prepost,[32] C.Y. Prescott,[27] G.D. Punkar,[27] J. Quigley,[15]
B.N. Ratcliff,[27] T.W. Reeves,[30] J. Reidy,[17] P.L. Reinertsen,[6] P.E. Rensing,[27]
L.S. Rochester,[27] P.C. Rowson,[10] J.J. Russell,[27] O.H. Saxton,[27] T. Schalk,[6]
R.H. Schindler,[27] B.A. Schumm,[14] S. Sen,[33] V.V. Serbo,[32] M.H. Shaevitz,[10]
J.T. Shank,[3] G. Shapiro,[14] D.J. Sherden,[27] K.D. Shmakov,[28] C. Simopoulos,[27]
N.B. Sinev,[20] S.R. Smith,[27] J.A. Snyder,[33] P. Stamer,[24] H. Steiner,[14] R. Steiner,[1]
M.G. Strauss,[16] D. Su,[27] F. Suekane,[29] A. Sugiyama,[19] S. Suzuki,[19] M. Swartz,[27]
A. Szumilo,[31] T. Takahashi,[27] F.E. Taylor,[15] E. Torrence,[15] A.I. Trandafir,[16]
J.D. Turk,[33] T. Usher,[27] J. Va'vra,[27] C. Vannini,[23] E. Vella,[27] J.P. Venuti,[30]
R. Verdier,[15] P.G. Verdini,[23] S.R. Wagner,[27] A.P. Waite,[27] S.J. Watts,[4]
A.W. Weidemann,[28] E.R. Weiss,[31] J.S. Whitaker,[3] S.L. White,[28] F.J. Wickens,[25]
D.A. Williams,[6] D.C. Williams,[15] S.H. Williams,[27] S. Willocq,[33] R.J. Wilson,[8]
W.J. Wisniewski,[27] M. Woods,[27] G.B. Word,[24] J. Wyss,[21] R.K. Yamamoto,[15]
J.M. Yamartino,[15] X. Yang,[20] S.J. Yellin,[5] C.C. Young,[27] H. Yuta,[29]
G. Zapalac,[32] R.W. Zdarko,[27] C. Zeitlin,[20] and J. Zhou,[20]

[1] *Adelphi University, Garden City, New York 11530*
[2] *INFN Sezione di Bologna, I-40126 Bologna, Italy*
[3] *Boston University, Boston, Massachusetts 02215*
[4] *Brunel University, Uxbridge, Middlesex UB8 3PH, United Kingdom*
[5] *University of California at Santa Barbara, Santa Barbara, California 93106*
[6] *University of California at Santa Cruz, Santa Cruz, California 95064*
[7] *University of Cincinnati, Cincinnati, Ohio 45221*
[8] *Colorado State University, Fort Collins, Colorado 80523*
[9] *University of Colorado, Boulder, Colorado 80309*
[10] *Columbia University, New York, New York 10027*
[11] *INFN Sezione di Ferrara and Università di Ferrara, I-44100 Ferrara, Italy*
[12] *INFN Lab. Nazionali di Frascati, I-00044 Frascati, Italy*
[13] *University of Illinois, Urbana, Illinois 61801*
[14] *Lawrence Berkeley Laboratory, University of California, Berkeley, California 94720*
[15] *Massachusetts Institute of Technology, Cambridge, Massachusetts 02139*

[16] *University of Massachusetts, Amherst, Massachusetts 01003*

[17] *University of Mississippi, University, Mississippi 38677*

[18] *Moscow State University, Institute of Nuclear Physics, 119899 Moscow, Russia*

[19] *Nagoya University, Chikusa-ku, Nagoya 464 Japan*

[20] *University of Oregon, Eugene, Oregon 97403*

[21] *INFN Sezione di Padova and Università di Padova, I-35100 Padova, Italy*

[22] *INFN Sezione di Perugia and Università di Perugia, I-06100 Perugia, Italy*

[23] *INFN Sezione di Pisa and Università di Pisa, I-56100 Pisa, Italy*

[24] *Rutgers University, Piscataway, New Jersey 08855*

[25] *Rutherford Appleton Laboratory, Chilton, Didcot, Oxon OX11 0QX United Kingdom*

[26] *Sogang University, Seoul, Korea*

[27] *Stanford Linear Accelerator Center, Stanford University, Stanford, California 94309*

[28] *University of Tennessee, Knoxville, Tennessee 37996*

[29] *Tohoku University, Sendai 980 Japan*

[30] *Vanderbilt University, Nashville, Tennessee 37235*

[31] *University of Washington, Seattle, Washington 98195*

[32] *University of Wisconsin, Madison, Wisconsin 53706*

[33] *Yale University, New Haven, Connecticut 06511*

[†] *Deceased*

[a] *Also at the Università di Genova*

[b] *Also at the Università di Perugia*

Bibliography

[1] S.L.Glashow, *Nucl. Phys.* **22** (1961) 579;
   A.Salam, J.C.Ward, *Phys. Lett.* **13** (1964) 168;
   S.Weinberg, *Phys. Rev. Lett.* **19** (1967) 1264.

[2] H.M.Foley, P.Kusch, *Phys. Rev.* **73** (1948) 412;
   R.L.Garwin, L.M.Lederman, M.Weinrich, *Phys. Rev.* **105** (1957) 1415.

[3] PDG Collaboration, R.M.Barnett *et al.*, *Phys. Rev.* D **54** (1996) 1.

[4] "Status of the new Muon (g-2) Experiment", *Proceedings of the Twenty Eighth International Conference on High Energy Physics*, Warsaw, Poland, 1996.

[5] J.Bernabeu, G.A.Gonzalez-Sprinberg, M.Tung, J.Vidal, *Nucl. Phys.* B **436** (1995) 474.

[6] W.Bernreuther, U.Low, J.P.Ma, O.Nachtmann, *Z. Phys.* C **43** (1989) 117.

[7] G.L.Kane, G.A.Ladinsky, C.P.Yuan, *Phys. Rev.* D **45** (1992) 1709.

[8] W.Bernreuther, O.Nachtmann, P.Overmann, *Phys. Rev.* D **48** (1993) 78.

[9] LEP Electroweak Working Group, D.Abbaneo *et al.*, "A Combination of Preliminary Electroweak Measurements and Constraints on the Standard Model", CERN–PPE/96–183 (1996).

[10] T.G.Rizzo, *Phys. Rev.* D **51** (1995) 3811.

[11] T.G.Rizzo, SLAC–PUB–7453, (1997), *Submitted to* Phys. Rev. *D.*

[12] Y.S.Tsai, *Phys. Rev.* D **4** (1971) 2821;
Erratum - *ibid.*, *Phys. Rev.* D **13** (1976) 771.

[13] "The SLD Design Report", SLAC–Report–229, (1980).

[14] R.Alley *et al.*, *Nucl. Instrum. Methods* **A365** (1995) 1.

[15] M.G.Minty, R.Akre, P.Krejcik, R.H.Siemann, *Particle Accel. Conf:* IEEE 1995:3046.

[16] R.Pitthan *et al.*, *Particle Accel. Conf:* IEEE 1991:2098.

[17] T.L.Barklow *et al.*, *Part. Accel.* **30** (1990) 121.

[18] T.Maruyama *et al.*, *Phys. Rev. Lett.* **66** (1991) 2351.

[19] T.Maruyama, R.Prepost, *Annual Review of Nucl. Part. Sci.* **45** (1995) 41.

[20] C.Adolphson *et al.*, SLAC–PUB–6118, (1993).

[21] T.Limberg, P.Emma, R.Rossmanith, SLAC–PUB–6210, (1993).

[22] G.Blaylock, SLC Physics Note 22, (1993).

[23] "The SLD Design Report", SLAC–Report–273, (1984).

[24] D.Sherden, *Nucl. Instrum. Methods* **A265** (1988) 342.

[25] C.J.S.Damerall *et al.*, *Nucl. Instrum. Methods* **A288** (1990) 236.

[26] M.D.Hildreth *et al.*, *Nucl. Instrum. Methods* **A367** (1995) 111.

[27] D.Williams, PhD Thesis, Massachusetts Institute of Technology (1994).

[28] K.Abe *et al.*, *Nucl. Instrum. Methods* **A343** (1994) 74.

[29] T.J.Pavel, PhD Thesis, Stanford University (1996).

[30] D.Axen *et al.*, *Nucl. Instrum. Methods* **A328** (1993) 472.

[31] A.C.Benvenuti *et al.*, *Nucl. Instrum. Methods* **A290** (1990) 353.

[32] S.L.White, PhD Thesis, Tennessee University (1995).

[33] S.Jadach, B.F.L.Ward, Z.Was, *Comput. Phys. Commun.* **79** (1994) 503.

[34] S.Jadach, Z.Was, R.Decker, J.H.Kuhn, *Comput. Phys. Commun.* **76** (1993) 361.

[35] R. Brun, R. Hagelberg, M. Hansroul, J.C. Lassalle, CERN-DD/72/2 (1978).

[36] M.Fero *et al.*, SLD Physics Note 50, (1996).

[37] D.Calloway *et al.*, SLD Note 246, (1996).

[38] R.Elia, PhD Thesis, Stanford University (1994);
R.King, PhD Thesis, Stanford University (1994).

[39] A.Lath, PhD Thesis, Massachusetts Institute of Technology (1994).

[40] H.Frauenfelder, A.Rossi, Vol. 5, Part B, *Methods of Experimental Physics*, edited by I.C.L.Yuan and C.S.Wu, Academic Press, New York, 1963.

[41] C.Y.Prescott, SLAC–TN–73–1, (1973);
M.L.Swartz, SLAC–PUB–4656, (1988).

[42] H.Veltman, *Phys. Rev.* **D40** (1989) 2810;
Erratum: *ibid.* **D42** (1990) 1856.

[43] P.L.Reinertsen, SLD Physics Note 45, (1996).

[44] W.R.Nelson, H.Hirayama, D.W.O.Rogers, *The EGS4 Code System*, SLAC–Report–265, (1985).

[45] G.Menegatti, M.Fero, SLD Note 247, (1996).

[46] P.Raimondi, private communication.

[47] P.Emma, *Depolarization in the SLC Final Transformer*, unpublished note.

[48] P.Chen, K.Yokoya, *Proceedings of the Eighth International Symposium on High-Energy Spin Physics,* Minneapolis, MN, 1988, pg. 938.

[49] M.J.Fero and F.J.Decker, SLD Note 249, (October 1996).

[50] B.Schumm *et al.*, SLD Note 240, (March 1994).

[51] SLD Collaboration, K.Abe *et al.,Phys. Rev. Lett.* **73** (1994) 25.

[52] J.Quigley, PhD Thesis, Massachusetts Institute of Technology (1997).

[53] J.Yamartino, PhD Thesis, Massachusetts Institute of Technology (1994).

[54] SLD Collaboration, K.Abe *et al.*, *Phys. Rev. Lett.* **78** (1997) 23.

[55] N.Allen, PhD Thesis, Brunell University (1997).

[56] F.James, M.Roos, *Comput. Phys. Commun.* **10** (1975) 343.

[57] W.T.Eadie, D.Drijard, F.James, M.Roos, B.Sadoulet, *Statistical Methods in Experimental Physics*, North-Holland, 1971.

[58] SLD Collaboration, K.Abe *et al.*, *Phys. Rev. Lett.* **78** (1997) 17.

[59] U.Stiegler, *Comput. Phys. Commun.* **81** (1994) 221.

[60] J.F.Donoghue G.Valencia, *Phys. Rev. Lett.* **58** (1987) 451;
W.Bernreuther, O.Nachtmann, *Phys. Lett.* B **268** (1991) 424;
B.Ananthanarayan, S.D.Rindani, *Phys. Rev.* D **51** (1995) 5996.

[61] Opal Collaboration, P.D.Acton *et al.*, *Phys. Lett.* B **281** (1992) 405;

Opal Collaboration, R.Akers *et al.*, *Z. Phys.* C **66** (1995) 31;

Opal Collaboration, K.Ackerstaff *et al.*, CERN-PPE/96-184, *Submitted to* Z. Phys. *C*;

Aleph Collaboration, D.Buskulic *et al.*, *Phys. Lett.* B **297** (1992) 459;

ibid., *Phys. Lett.* B **371** (1995) 371.

[62] N.Wermes, *Proceedings of the Fourth International Workshop on Tau Lepton Physics*, Estes Park, CO, Sep 1996.

[63] E.Sanchez, *Proceedings of the Fourth International Workshop on Tau Lepton Physics*, Estes Park, CO, Sep 1996.

[64] L.Taylor, *Proceedings of the Fourth International Workshop on Tau Lepton Physics*, Estes Park, CO, Sep 1996.

[65] J.D.Bjorken, S.D.Drell, *Relativistic Quantum Mechanics*, McGraw-Hill (1964).

[66] D.Griffiths, *Introduction to Elementary Particles*, Wiley (1987).

[67] K.L.Brown, F.Rothacker, D.C.Carey, F.C.Iselin, *Transport: A Computer Program for Designing Charged Particle Beam Transport Systems*, SLAC-91 Rev. 2 (1977).

[68] D.C.Carey, K.L.Brown, F.C.Iselin, *Decay Turtle: A Computer Program for Simulating Charged Particle Beam Transport Systems, Including Decay Calculations*, SLAC-246 (1982).